Emplacement Conditions of Some Lac de Gras Kimberlites and Their Effect on the Resorption of Diamonds

by

Yana Fedortchouk
Diploma, Moscow State University, 1993

A Dissertation Submitted in Partial Fulfillment of the
Requirements for the Degree of

DOCTOR OF PHILOSOPHY

in the School of Earth and Ocean Sciences

Emplacement Conditions of Some Lac de Gras Kimberlites and Their Effect on the Resorption of Diamonds

by

Yana Fedortchouk

Diploma, Moscow State University, 1993

Supervisory Committee

Dr. Dante Canil, (School of Earth and Ocean Sciences)

Supervisor

Dr. Kathryn M. Gillis, (School of Earth and Ocean Sci.)

Departmental Member

Dr. Kevin Telmer, (School of Earth and Ocean Sciences)

Departmental Member

Dr. Thomas M. Fyles, (Department of Chemistry)

Outside Member

Dr. Robert W. Luth, (Dep. of Earth and Atm. Sci., U. of Alberta)

Additional Member

Supervisory Committee

Supervisor	Dr. Dante Canil, (School of Earth and Ocean Sciences)
Departmental Member	Dr. Kathryn M. Gillis, (School of Earth and Ocean Sciences)
Departmental Member	Dr. Kevin Telmer, (School of Earth and Ocean Sciences)
Outside Member	Dr. Thomas M. Fyles, (Department of Chemistry)
Additional Member	Dr. Robert W. Luth, (Dep. of Earth and Atm. Sci., U. of Alberta)

ABSTRACT

Crystallization temperatures (T) and oxygen fugacities (fO_2) of kimberlite magma estimated from oxides included in olivine phenocrysts from eight kimberlite pipes in the central Slave Province, Canada, are compared to the degree and character of resorption observed in diamonds recovered from these kimberlites. The mechanism of diamond oxidation in kimberlite melts and the rate-controlling parameters for this reaction are explored in oxidation experiments. The T and maximum fO_2 recorded by olivine – chromite pairs at an assumed pressure of 1 GPa are 970° – 1070°C and 2.2 – 3.1 log units below the nickel – nickel oxide (NNO) buffer. This mineral assemblage crystallized from a magma with 11 to 28 mol% of liquid, 10 mol% of earlier-precipitated olivine phenocrysts and 62 to 79 mol% of mantle xenocryst olivine. The T – fO_2 values vary between kimberlites from Northwest and Southeast clusters within 150°C and one log unit, respectively, and form a trend of decreasing fO_2 and increasing crystallization T in the southeast direction. This trend corresponds to substantial differences in the diamond populations. A detail description of morphological forms and surface resorption features for five diamond parcels (> 7000 stones) show an increase in diamond resorption with increase in kimberlite crystallization T and more extensive surface etching in more oxidized kimberlites. The surface etch features on diamonds are determined by the

conditions in the kimberlite melt, whereas some of the volume resorption occurs in the mantle and its relationship with the melt conditions is obscure. The diamond grade is higher in kimberlites with lower fO_2 confirming the effect of the melt conditions on diamond preservation. Diamond oxidation experiments at 1350°C to 1500°C and 1 GPa produced only surface graphitisation, and no diamond resorption in volatile-undersaturated melts. In contrast, volatile oversaturated conditions produce resorption features seen in diamonds recovered from kimberlites, suggesting that the process of diamond resorption is its reaction with the fluid and not with the melt. Both CO_2 and H_2O oxidize diamonds at a similar rate, but produce very different surface features. Therefore, the surface features of natural diamonds may provide information on the H_2O/CO_2 ratio in the kimberlitic fluid. The morphologies of diamonds from this study imply high H_2O/CO_2. The scarcity of surface graphitisation and presence of highly resorbed diamonds in kimberlites suggest presence of free fluid phase in kimberlite magmas for the most of their history. The diamond oxidation is not affected by the physical properties of diamonds.

TABLE OF CONTENTS

LIST OF TABLES

LIST OF FIGURES

ACKNOWLEDGMENTS

This study would not be possible without guidance of Dante Canil. I was very fortunate to work under his supervision. His extensive knowledge and deep interest in the evolution of the Earth created a very encouraging environment for his students. I want to express him my deepest gratitude for his invaluable advises, patience and support, for being always available for help, for interesting discussions. Due to his help I greatly expanded my knowledge during these years and it was a great pleasure to work with him and to get to know him.

I sincerely thank Jon A. Carlson, Darren R. Dyck and BHP Billiton Diamonds Inc. for access to drill-core and diamonds, for support and suggestions during sampling and permission to publish the results. I am especially grateful to Jon A. Carlson for giving me an opportunity to work at BHP Billiton Diamonds Inc. on diamond projects and to collect the data on diamond resorption, for organizing training in diamond descriptions and providing with the necessary diamond parcels. I also want to extend my thanks to everyone at BHP office in Kelowna for creating a wonderful atmosphere I enjoyed while working there.

I would like to thank all the people who helped me obtaining samples for this study. Catherine McCammon and Maya Kopylova shared with me chromite grains where they measured Fe^{3+} by Mössbauer spectroscopy. Tom Nowicki at Mineral Services Canada Inc. and Maya Kopylova provided some of the kimberlite samples.

I am grateful to Elena Semenets for participation in the study of resorption of different diamonds, and her interest to the phenomena of diamond resorption. Her help in obtaining the data on nitrogen content and aggregation for the diamonds I used in the experiments made this part of the work possible. Branko Deljanin and European Gemological Laboratories at Vancouver are thanked for the access to the FTIR spectrometer and Patrick Hayman for the help with deconvolution of the spectra.

Particular gratitude is expressed to Maya Kopylova for sharing her knowledge about kimberlites; discussing different parts of my project, help with obtaining samples and literature. I am very grateful to John Gurney for sharing his experience in diamond descriptions, for his patience and time answering my numerous questions. Conversations with him greatly expanded my knowledge about diamonds. My work benefited a lot from

discussions with Valentin Afanasiev on diamond morphology. I would like to thank Anton Chakhmouradian for providing me with some Russian literature on diamonds and Stephen Parman for giving me some tips on experimental procedures. I am grateful to M. Arima, C. Ballhaus, N. Green, O. Navon, J.K. Russell and A. Woodland for their critical reviews and helpful comments on my manuscripts.

During the time I spent at UVic working on my thesis I really enjoyed company of my student colleagues Jason MacKenzie, Kim Scully, Tony Bellis, Zhihuan Wan and many others, whom I want to thank for creating a stimulating environment, for the interesting discussions we had and for the help we provided each other with experimental procedures and equipment.

I would like to thank everyone who helped me with microprobe and SEM work: Mati Raudsepp (at UBC), Lang Shi (University of Alberta), Bruce Kaye (Defence Research and Development Canada) and Brent Gowen (University of Victoria). I am very grateful to Mati Raudsepp for valuable suggestions during microprobe work. Defence Research and Development Canada is thanked for giving me free access to their equipment. I want to thank Richard Robinson and Doug Stajduhar in the Chemistry machine shop (University of Victoria) for their help and creativeness in preparing parts for experimental equipment.

I greatly appreciate hospitality of Maya Kopylova and Alexander Lykov, at whose home I was staying in Vancouver during microprobe work at UBC, and Tamara and Vadim Astakhov, with whom I stayed in Kelowna during work at BHP on diamond parcels.

This work would not be possible without support from my family. I want to express my sincere gratitude to my husband, Pavel, for his constant encouragement and great interest in my work, for doing his best in taking care of the children and household in my busiest times. I want to thank my children, Arseny, Galina and Iakov, for their understanding and my mother, Alexandra, whose help with the youngest grandson made it possible for me to finish this work.

The Natural Sciences and Engineering Research Council of Canada, University of Victoria and BHP Billiton Diamonds Inc. are acknowledged for financial support of this research.

I dedicate this work to my grandparents

GALINA TEREKHOVA and VICTOR FEDORCHUK

who awakened my interest in geology

and whose personal and professional lives

have served as a great example to me

CHAPTER 1.

INTRODUCTION

This dissertation is a study of fresh kimberlites recently found in N.W.T. of Canada and the diamonds recovered from these rocks. For the first time, crystallization conditions of these complex magmas, their role on the quality and grade, and surface features of kimberlite-hosted diamonds, and the nature of the diamond interaction with kimberlite melt are addressed in a comprehensive petrological study of natural kimberlites and an experimental study of the processes that ensue in such magmas.

Kimberlites are volatile-rich alkaline ultrabasic rocks first described at Kimberley, South Africa, in the end of 19^{th} century as the first primary source of diamonds. Kimberlites are now found on all continents (Fig.1.1), concentrated in cratonic tectonic settings but are also found in surrounding mobile belts (Scott Smith, 1996). Being relatively exotic low-volume volcanic rocks, kimberlites, nevertheless, attract a lot of attention as the main primary source of diamonds and as deep-seated magmas that provide a window into the deeper parts of Earth's mantle. During ascent, kimberlites sample mantle material as xenoliths and xenocrysts and bring them to the surface. Moreover kimberlite-hosted diamonds contain mineral inclusions that record mineral assemblages of the upper and, in few cases, lower mantle. In spite of intensive studies in last few decades, the origin and evolution of these magmas are still poorly understood, due to the paucity of well-preserved, fresh natural examples.

The primary composition of kimberlite melts is still not well constrained. Kimberlites are hybrid rocks. They contain primary minerals crystallized from the

kimberlite melt (euhedral olivine, spinel, monticellite, phlogopite, perovskite, apatite, carbonate and serpentine) and mega- and macrocryst assemblage of unknown origin (anhedral olivine, Mg-ilmenite, pyrope, diopside, phlogopite, enstatite and chromite) (Mitchell, 1996) that may have originated from the disintegrated mantle xenoliths, may represent early minerals on the kimberlite liquidus, or crystallized from protokimberlite melts. Kimberlites also contain numerous mantle and crustal xenoliths and typically show significant alteration. The similar composition of the xenocrystal and phenocrystal olivine (Mitchell, 1986), the most abundant mineral in kimberlites, and unknown origin of mega/macrocrysts preclude determination of the chemical composition of primary kimberlite melt. Based on mineralogy, kimberlites are divided into basaltic (Group I) and micaceous (Group II or Orangites, Mitchell, 1995) (Mitchell, 1986). Group I is further subdivided into IA and IB on the basis of Nd and Sr isotopic composition (Smith et al., 1985). The best approximation for the Group I kimberlites is the composition of aphanitic kimberlite of Wesselton mine, South Africa, (Shee, 1986) and Jericho pipe, Slave craton, Canada (Price et al., 2000). Both of these examples have almost no macrocrysts and high MgO content suggesting, but not proving, their uncontaminated and unfractionated nature.

Liquids produced experimentally by partial melting of carbonated peridotite provide another estimate on the composition of kimberlite melts (Canil and Scarfe, 1990; Dalton and Presnall, 1998; Gudfinnsson and Presnall, 2005). They depend on the choice of the composition of the mantle source and the conditions during melting. Although, the two approaches providing working hypotheses for the composition of primary kimberlite melts, they have nevertheless to rely on several assumptions and show compositional variation especially in terms of the volatile content.

Ambiguity in the primary melt composition results in disagreement regarding the nature of the mantle source for kimberlites, uncertainty in their crystallization conditions (T, P, fO_2) and evolution. Melting experiments on peridotite + CO_2 system (e.g. Canil and Scarfe, 1990; Dalton and Presnall, 1998; Gudfinnsson and Presnall, 2005) and kimberlite geochemistry (Roex et al., 2003) indicate that these magmas could be produced by very small degree of partial melting of carbonated garnet lherzolite mantle at pressures around 5 – 6 GPa (Group IB) and around 10 GPa (Group IA). Results of melting experiments on the natural and synthetic kimberlites place their source at much greater depths than 10 GPa (e.g. Edgar and Charbonneau, 1993) in the orthopyroxene-free garnetite (garnet + clinopyroxene ± olivine), or even in the transition zone (Ringwood et al., 1992). Mitchell (2004) proposed formation of kimberlite magmas by extensive (10 – 50 vol%) partial melting of metasomatized mantle, within mineralogically complex carbonate-bearing veins.

The choice of the model for the kimberlite source determines the estimates for the liquidus temperatures and mineral assemblages during kimberlite crystallization, both also complicated by the unknown volatile content and composition (H_2O/CO_2 ratio) of the magma. Calculation of T and fO_2 of kimberlite magmas from mineral geothermometers and oxygen barometers is usually not possible due to the high degree of alteration of primary kimberlite minerals. Finding approaches to constrain the composition of kimberlite melt, and its crystallization T, fO_2 and volatile content is important in order to shed more light on the origin and evolution of kimberlites and processes in subcontinental mantle. Crystallization conditions of kimberlites may also significantly affect their diamond population.

For thousands of years people valued diamonds for their beauty, hardness and resistance to impact. Diamonds were found only in secondary sources, placers, mainly alluvial deposits, until the first diamondiferous kimberlite was discovered near Kimberley, South Africa, in 1869. It was soon recognized that kimberlites only provide transportation for diamonds to the Earth's surface, whereas the diamonds were formed deep in the Earth's mantle (Meyer, 1985). The diamond ages of 3.2 – 3.3 Ga estimated from Sm – Nd and Rb – Sr isotope systems in peridotitic mineral inclusions in diamonds (Richardson et al., 1984) and 2.9 – 3.0 Ga from Re – Os system in sulfide inclusions (Richardson et al., 2001) are much older than the emplacement ages of the hosted kimberlites. But ages as young as 360 Ma were also suggested that required diamond crystallization just before the kimberlite eruption (Shimizu and Sobolev, 1995).

Diamonds are believed to be formed at the base of cratons, the oldest and deepest parts of continental lithosphere, where at high pressures the temperatures are low enough to be below the diamond – graphite transition (e.g. Haggerty, 1986). The two common environments for diamond growth are eclogitic (E-type) and peridotitic (P-type) (e.g. Meyer, 1985), but the possibility exists for crystallization of some microdiamonds from volatile-rich silicate melts of kimberlitic composition in the upper mantle (Arima et al., 1993). Recent discoveries of diamonds with lower mantle mineral assemblages preserved as inclusions (e.g. McCammon, 2001) make these diamonds the deepest originating material found on the Earth's surface.

Mineral inclusions trapped by diamonds during their growth provide important information on the composition and evolution of the lithospheric mantle and therefore are intensively studied. Nitrogen impurities and their aggregation forms in the diamond lattice provide information on the temperature during diamond growth and residence in

the mantle (Evans and Harris, 1989). Variations in carbon isotopes suggest growth of some of the diamonds from recycled subducted carbon, whereas others were formed from primordial material (Gurney, 1986; Meyer, 1985). Thus, diamonds provide us with a unique record of the Earth's history hidden in the major and trace-element chemistry and radiogenic isotope systems of the mineral and fluid inclusions they contain, the content and aggregation form of the impurities and other defects of the diamond lattice and carbon isotopes.

Diamonds show a great variety of morphological forms and colours (Fig. 1.2). It was recognized early that some of these forms are primary and are the result of crystal growth, whereas others are secondary, the result of diamond resorption (Fersmann and Goldschmidt, 1911). Octahedra and cubes are the two primary diamond morphologies. At the conditions outside of diamond stability, the resorption of diamond develops more complex forms with a larger number of faces and produces dodecahedron (12-face) and tetrahexahedron (24-face) crystals. The surface of such a diamond also exhibits a great variety of etch features and imperfections. Cathodoluminescence studies of the internal structure of diamonds revealed several growth zones in a single diamond grain, divided by periods of resorption that infer a mantle origin for some of the resorption events (Taylor et al., 1995). Nevertheless, since the high-temperature kimberlite melt is expected to be a very reactive environment for the entrained diamonds, the majority of diamond resorption is believed to happen after entrainment in the ascending kimberlite through diamond dissolution in the melt (Arima, 1998; Robinson et al., 1989). The duration of diamond exposure in the melt and the conditions of the melt would then have a great effect on the kinetics of this reaction. The influence of temperature and oxygen fugacity on the rate of diamond oxidation was confirmed by experimental studies (Cull and Meyer,

1986; Evans and Phaal, 1961; Kozai and Arima, 2005; Sonin et al., 2000). They all show faster diamond oxidation at higher T and fO_2, but the relationships between T, fO_2 and diamond oxidation rate vary significantly between the different studies. Moreover, almost all diamond oxidation experiments at controlled fO_2, except Kozai and Arima (2005), were done in a mixture of gases at 100 KPa. Constraining the crystallization path of natural kimberlites and the development of methods that allow calculating their temperatures and oxygen fugacity are, therefore, important for predicting of the degree of diamond preservation and diamond quality in a particular kimberlite pipe. The study of the morphology and surface features of kimberlite-hosted diamonds, on another hand, can help to learn more about the evolution of kimberlite magmas.

The recent discovery of new kimberlite provinces in the Canadian North started in early 1990s with the discovery of diamondiferous kimberlites in Lac de Gras area, N.W.T. (Pell, 1997) and has expanded to many localities in N.W.T., Ontario, Alberta, Quebec and Nunavut, providing new kimberlite and diamond material for investigation. Some of these kimberlites are extremely fresh with well-preserved primary mineralogy compared to South African and Siberian kimberlites. For this reason, the Canadian pipes give new unprecedented opportunities for understanding of composition and crystallization conditions of kimberlite magmas. Moving the diamond mining activity into Canada and the resultant growth of interest in kimberlite and diamond studies made the material easily accessible for investigation.

The main focus of the dissertation is an investigation of how the conditions of kimberlite melts affect the process of diamond resorption during the emplacement. This includes: 1) constraining crystallization conditions of kimberlite melts; 2) investigating

how these conditions affect the diamond population of the kimberlites; 3) finding the mechanism of diamond oxidation in kimberlite magmas.

The first goal of the present study was to find an approach to calculate T and fO_2 for kimberlite melts, that was previously complicated by the poor preservation of the primary minerals in these usually highly altered rocks. T and fO_2 during kimberlite crystallization are important parameters for diamond preservation since the previous experimental studies (Cull and Meyer, 1986; Evans and Phaal, 1961; Kozai and Arima, 2005; Sonin et al., 2000) showed their significant influence on the kinetics of diamond oxidation. Furthermore, constraining crystallization T and fO_2 helps to understand better the evolution of kimberlite melts.

An existing Ol – Sp geothermometer and oxygen barometer (Ballhaus et al., 1991) was applied to chromite inclusions in olivine phenocrysts in the studied kimberlites to obtain T and fO_2 values that were then adjusted to account for the extremely low silica activity of kimberlite melts. The obtained T and fO_2 values were used to estimate the composition of primary kimberlite melts, to asses how much mantle material these magmas accumulated and to compare the oxidation conditions of kimberlites to those of the other mantle derived magmas to learn about the conditions in the mantle source of kimberlites. In addition, the calculated T and fO_2 of kimberlite melts constrain the emplacement path of these magmas in T-P-fO_2 space and limit the path relative to the stability fields of different forms of carbon (diamond, graphite, CO_2) in the mantle, making it possible to evaluate diamond preservation during kimberlite ascent.

The next task was to apply the approach developed for T and fO_2 calculations to the larger number of kimberlites where an immense amount of data on the diamond populations (degree of preservation, surface resorption features) was collected. The main

goal of this part of the thesis was to test if the conditions of kimberlite melt correlate with the degree of diamond resorption in a particular kimberlite and/ or with the development of any of the resorption features observed on the diamonds. This research addresses whether the effect of T and fO_2 on the diamond population of a kimberlite is significant enough to be recorded in the characteristics of the diamonds. The obtained T - fO_2 data also provides an opportunity to investigate variation in the oxidation state between different kimberlite bodies, and kimberlites from different clusters in order to learn more about the changes in their mantle source in time and space, and about changes in kimberlite oxidation state during crystallization. A comprehensive database on the presence and distribution of various resorption features collected from more than 7000 Lac de Gras diamonds allows the extrapolation of relative timing of different resorption events, to correlate different resorption features to the certain parameters of the kimberlite system, and to make conclusions about the amount of the resorption caused by kimberlite magmas versus those that occured in the mantle source. As a more practical application, this study assesses what diamond features are determined by the certain parameters of the kimberlite melts. It also suggests an expansion of the commonly used evaluation of kimberlite pipes which is based mainly on the amount and composition of the mantle material in the magma, to include consideration of the conditions in the kimberlite melt as well.

The empirical correlation between diamond resorption features, T and fO_2 of kimberlite melt indicates that these parameters are among the most important rate-controlling parameters in the process of diamond oxidation. In order to confirm this empirically derived conclusion we need to know the mechanism of diamond oxidation in kimberlite magmas, which is not yet completely understood. Knowing the processes that

operate during diamond oxidation is important in order to evaluate what are the rate-controlling parameters for this reaction in nature.

All the previous experimental studies were either done in a mixture of gases at 100 KPa and T lower than in kimberlite magmas (Cull and Meyer, 1986, Evans and Phaal, 1961, Sonin et al., 2000) or in a complex composition of natural kimberlites or alkaline basalts (e.g. Arima, 1998, Chepurov et al., 1985, Harris and Vance, 1974, Kozai and Arima, 2005, Sonin et al., 1997). The first approach investigated kinetics of diamond burning as a function of T and fO_2, but in the environment and conditions that are far from the ones of natural kimberlite magma. In the second approach, the complexity of the system that included a multi-component melt with dissolved volatiles of undetermined composition and a fluid phase of unknown composition, prevented understanding of which of the components or phases reacted with the diamonds to oxidize them. The only work that investigated the mechanism of diamond oxidation (Rudenko et al., 1979) by doing experiments in different simple systems explored low T and P conditions that are far from those expected in natural kimberlites and, therefore, have different kinetics of some of the processes.

The diamond oxidation experiments in the present work were performed in a simple CaO-MgO-SiO_2-H_2O system and in pure H_2O and CO_2 fluids that allowed exploration of the role of the melt and the different fluids in diamond oxidation, and determination of the mechanism of diamond resorption in kimberlite magmas. The importance of different parameters of kimberlite magmas and diamond properties for the rate of diamond oxidation was then assessed. The results of this work explaines many conflicting observations and interpretations on diamond resorption in previous experiments and provides a basis for further investigations. They also showed, for the

first time, the importance of the composition of kimberlitic fluid for the morphology and surface resorption features on diamonds, which impacts the quality of diamonds. Comparison of diamond resorption forms produced in controlled experiments with the features observed on the natural diamonds allowed the evaluation of conditions characterizing the natural kimberlite systems and provides a new tool of kimberlite investigation from the morphology of the kimberlite-hosted diamonds.

This work significantly expanded our understanding of crystallization conditions, oxidation state and volatile behavior of kimberlite magmas. It explained the process of diamond resorption and determined its rate-controlling parameters. The large effect of the composition of kimberlitic fluid and the conditions of kimberlite melt on the morphology and surface features of diamonds may have a practical output for the assessment of diamond population of a kimberlite.

Contribution of the authors

I wrote all the chapters of this dissertation solely. My supervisor Dr. Dante Canil edited all the chapters. The two published chapters: Chapter 2 (*Fedortchouk Y, Canil D.* Intensive variables in kimberlite magmas, Lac de Gras, Canada and implications for diamond survival. *Journal of Petrology* (2004) *45: 1725-1745*) and Chapter 3 (*Fedortchouk, Y., Canil, D., and Carlson, J.A.* Dissolution forms in Lac de Gras diamonds and their relationship to the temperature and redox state of kimberlite magma. *Contributions to Mineralogy and Petrology,* (2005) *150, 54-69*) were revised prior to the publication. The co-author on the second paper (Chapter 3) Jon A. Carlson (BHPBilliton Diamonds Inc., Kelowna) contributed to the project by initiating the diamond description work, providing me with training and the numerous (and generally inaccessible) diamond

samples necessary to accomplish this study. The co-author on the third project (Chapter 4) Elena Semenets (Gemological Research Inc., Vancouver) contributed by calculating the nitrogen content and aggregation state of the diamonds I used in the experiments. All of the results and interpretations are my own work.

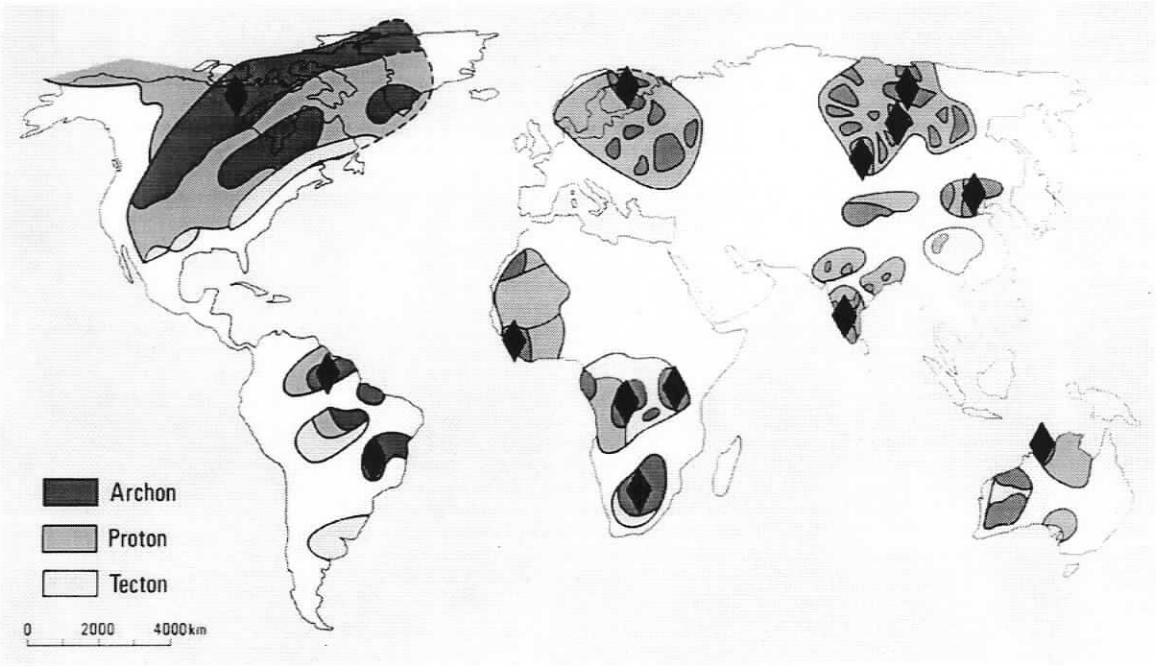

Figure 1.1 World map of cratons and major diamond deposits (red diamonds). The age provinces: Archons > 2.5 Ga, Protons – 2.5 to 1.6 Ga, and Tectons –1.6 to 0.8 Ga. (from Haggerty, 1999).

A.

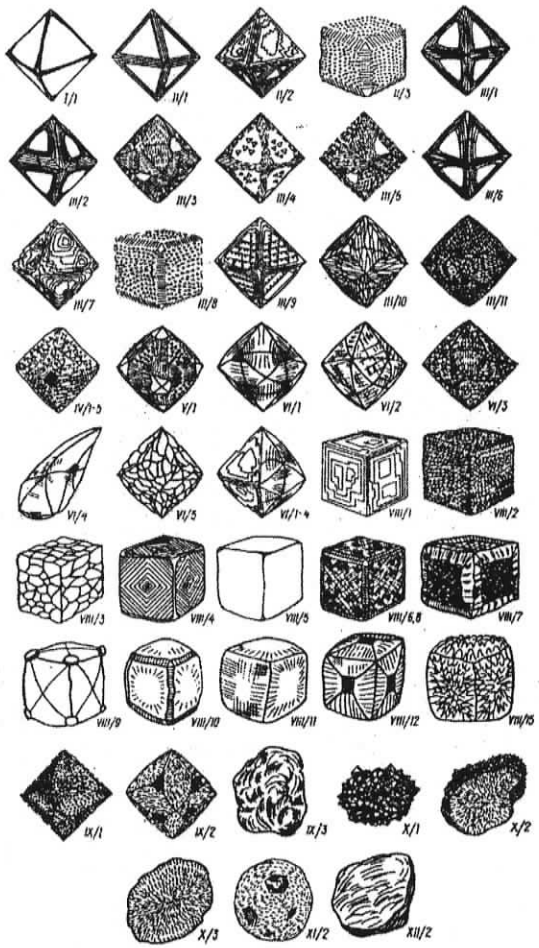

B.

Figure 1.2 Diversity of morphological forms observed in natural diamonds produced by both growth and resorption processes. A) from Bartoshinskiy (1983). B) diamonds recovered from Panda kimberlite in Lac de Gras kimberlite field, N.W.T., Canada.

CHAPTER 2.

INTENSIVE VARIABLES IN KIMBERLITE MAGMAS, LAC DE GRAS, CANADA AND IMPLICATIONS FOR DIAMOND SURVIVAL

Yana Fedortchouk

Dante Canil

School of Earth and Ocean Sciences, University of Victoria, Victoria, B.C., Canada

2.1. ABSTRACT

Crystallization temperatures (T) and oxygen fugacities (fO_2) of kimberlite magma are estimated from oxides included in olivine phenocrysts from the Leslie, Aaron, Grizzly and Torrie kimberlite pipes in the central Slave Province, Canada. Crystallization temperatures recorded by olivine-chromite pairs at an assumed pressure of 1.0 GPa are 1030 – 1170°C ± 50°C with a mean of ~1080°C. At these temperatures the fO_2 of coexisting olivine and chromite are 2 to 3 log units less oxidized than the nickel-nickel oxide (NNO) buffer at a silica activity limited by the presence of monticellite. Mass balance of olivine, bulk rock, and liquid compositions in equilibrium with olivine phenocryst rims, suggest these kimberlites represent crystallization from a magma with 11 to 28 mol% of liquid, 10 mol% of earlier precipitated olivine phenocrysts and 62 to 79 mol% of mantle xenocryst olivine. The calculated T – fO_2 values indicate that diamonds

entrained in the Lac de Gras kimberlites were most likely transported to the surface within the stability field of graphite but close to the graphite - CO_2 boundary.

Key words: chromite; crystallization temperature; kimberlite; olivine; oxygen fugacity

2.2. INTRODUCTION

Kimberlites are exotic and complex rocks that for a number of reasons are attractive for study. Firstly, the composition and intensive variables (e.g. T, fO_2) of these mantle-derived magmas shed light on the processes and conditions in their deep mantle source. Secondly, because kimberlites are the main primary source of diamonds, knowing these intensive variables constrains the likely presence and quality of diamonds in a pipe.

Despite decades of study on kimberlites there is still no comprehensive model for their origin and evolution (Mitchell, 1995). One of the major unknowns is the primary composition of kimberlite melt formed in the mantle. Kimberlite magma sampled at the surface is a hybrid of minerals formed by crystallization and xenoliths derived from the mantle and crust. There are no unambiguous criteria to isolate material crystallized from the melt phase, from that contributed by xenolithic material.

The best approximations of natural primary magmas are aphanitic kimberlite such as at Wesselton, South Africa (Shee, 1986) or Jericho, Canada (Price et al., 2000). Even in these special cases, it remains unclear whether volatile (H_2O, CO_2) contents or their ratios have been preserved during emplacement. Experimental studies of natural and synthetic compositions can provide an estimate of liquidus temperatures for kimberlites (Canil and Scarfe, 1990; Dalton and Presnall, 1998; Edgar et al., 1988; Edgar and Charbonneau, 1993; Girnis et al., 1995; Ringwood et al., 1992), but these estimates can also be suspect because of the diversity in compositions chosen as starting material in the experiments,

and the effect of unconstrained primary CO_2/H_2O on resulting determinations of liquidus temperatures and mineralogy.

Application of mineral geothermometers and oxygen barometers for the estimation of T and fO_2 in kimberlite magma is usually not possible due to the high degree of alteration that many pipes experience during their emplacement. One possible measure of redox conditions in kimberlite is the chemical composition of ilmenite. Pipes that contain ilmenites with low Fe^{3+}/Fe^{2+} and high Mg are considered to have crystallized at low but undefined fO_2 conditions (Fipke et al., 1995). This method has two shortcomings: it has only been empirically developed for South African kimberlites and may not apply to pipes from other provinces such as in North America (Orr and Luth, 2000). Also, the paucity or absence of ilmenite in some kimberlite pipes limits its application (Fipke et al., 1995).

We examined some extremely fresh kimberlites from the Lac de Gras kimberlite field, in the Northwest Territories, Canada (Pell, 1997). Olivine phenocrysts in these kimberlites contain inclusions of magnesiochromite allowing application of Mg-Fe exchange thermometry and oxygen barometry to examine T – fO_2 evolution during emplacement of hypabyssal, diatreme and crater phases of pipe development. We then highlight the influence of all of these variables on the preservation of diamond in kimberlite melt and the prediction of economic potential of a kimberlite pipe.

2.3. GEOLOGY, PETROGRAPHY AND SAMPLES

2.3.1. Geology

The Lac de Gras kimberlite field is located in the east-central part of the Archean Slave Province, Canada (Fig. 2.1). The Lac de Gras kimberlites have Eocene and Late

Cretaceous emplacement ages (Davis and Kjarsgaard, 1997; Creaser et al., 2003) and intrude metamorphosed Archean sedimentary, volcanic, and plutonic rocks (Pell, 1997; Ward et al., 1995). Most of Slave Province kimberlite pipes do not outcrop at the surface and are usually small, ranging from 2 to 12 hectares in surface area (Pell, 1997). The majority of these pipes are filled by crater facies (pyroclastic and epiclastic) kimberlite intruded by hypabyssal facies magma (Kirkley et al., 1998; Pell, 1997). Diatreme facies kimberlite is rare in comparison with South African examples. This study examines fresh kimberlite sampled in drill core from four kimberlite pipes: Grizzly, Torrie, Leslie and Aaron, with an emphasis on the latter two (Fig. 2.1). The composition, age and other data for the four kimberlites are summarized in Table 2. 1.

The Leslie pipe is seven hectares in area (Fig. 2.2a). It was emplaced in porphyritic biotite granite and filled with very fresh hypabyssal facies kimberlite to the present land surface. Only a remnant of tuffisitic kimberlite breccia is intersected at a depth of 400 meters (Berg and Carlson, 1998). The nearby pipes of the same age are filled with crater facies kimberlite to a depth of at least 300 m (Berg and Carlson, 1998, and references therein). Thus, the absence of crater facies at Leslie cannot be the result of erosion but rather reflects either an explosively formed open vent that was subsequently filled by magmatic kimberlite, or an earlier tuffisitic kimberlite breccia phase displaced by a hypabyssal intrusion (Berg and Carlson, 1998). Bulk rock geochemical studies of Leslie samples by Berg and Carlson (1998) indicate that geochemical variations represent one intrusive phase or multiple phases of chemically identical magma batches. The Leslie pipe incorporates both wall rock granitoid and mantle xenoliths.

The Aaron pipe is mainly filled with pelletal volcaniclastic kimberlite that incorporates fragments of shale and biotite- and garnet-bearing country rock. The

southeast wall of the pipe is composed of hypabyssal kimberlite (Fig. 2.2b). The tuff and tuff breccia of the Torrie pipe intruded late Archean K-rich granitoids and have abundant clay and organic fragments (Orr and Luth, 2000).

2.3.2. Samples

Samples of the Leslie (LS-1 to -5) pipe were selected from 81 pieces of core collected every two to three meters from drill hole LDC-09 (Fig. 2.2a) in the interval between 20 to 231 meters. Sample LS-5 is located near the contact with wall rock and shows extensive serpentinization, whereas all four others are massive and extremely fresh hypabyssal kimberlite well suited for study of their primary mineral compositions.

Aaron samples (AN-1 to -7) were chosen from 95 pieces of core collected every 1 – 2 meters from drill hole 97-57 in the interval between 47 to 160 meters (Fig. 2.2b) and represent different kimberlite facies. Samples AN-1, 2, 6 and 7 are grey, hypabyssal kimberlite with little or no alteration; AN-3 is more altered and contains xenoliths of country rock, and AN-4 and AN-5 are friable, green volcaniclastic, with serpentine alteration and abundant wall-rock xenoliths.

Two samples from the Grizzly pipe (GR95-19 and GR95-43) are fresh macrocrystal hypabyssal kimberlite (similar to the Leslie kimberlite). Four samples from the Torrie pipe (TQY 94-17-3, TQY 94-17-13, TQY 94-17-15, TQY 94-17-18) are organic-bearing kimberlite tuff and tuff breccia. Sample locations within the drill core were not recorded during collection of samples from the two latter pipes.

2.3.3. Petrography

All Leslie samples and the hypabyssal facies of the Aaron pipe are macrocrystic hypabyssal monticellite kimberlite (Fig. 2.3a) according to the terminology of Scott Smith (1992). They contain abundant macrocrysts and phenocrysts of olivine, macrocrysts of garnet surrounded by secondary reaction rims, pale- to emerald-green clinopyroxenes (± garnet inclusions, reaction rims), kink-banded, altered biotite and mantle-derived micro-xenoliths set in relatively fresh matrix of dominantly monticellite and late olivine. Anhedral olivine macrocrysts (up to several mm) constitute 20-45 % of the rock and are oval with minor serpentinization along margins and fractures.

Olivine phenocrysts were distinguished using two criteria: euhedral shape and parallel extinction under crossed polars. They are small (0.2 – 1 mm), fresh and sometimes broken. Phenocrysts locally show distinctive zoning on backscattered-electron images (Fig. 2.3b) with the cores darker or brighter than the margins. The interiors are often rounded and anhedral indicating partial dissolution before overgrowth by a later generation of olivine. The margins of phenocrysts often contain inclusions of euhedral (1 to 10 μm) aluminous magnesian chromites (Fig. 2.3a). The matrix includes fresh, euhedral microphenocrysts of olivine (up to 0.2 mm) and abundant monticellite (up to 80 μm)(Fig. 2.3c) surrounded by a fine-grained aggregate of serpentine with zoned perovskite, altered chromite, magnetite, late-stage phlogopite (in Leslie samples), Mg-rich ilmenite, calcite, apatite, and minor sulfides (pyrite).

Samples close to the contact with wall rocks are more extensively altered. LS-5 from the Leslie pipe has olivine macro- and phenocrysts that show significant serpentinization along fractures and margins. Calcite and serpentine aggregates occur as

pseudomorphs on olivine microphenocrysts and monticellite. The groundmass is altered to calcite, abundant clay minerals and laths of phlogopite. Mineralogically this rock is a macrocrystic hypabyssal calcite serpentine kimberlite. Sample AN-3 from the contact between hypabyssal and volcaniclastic kimberlite of the Aaron pipe is even more altered. The olivine macro- and phenocrysts are often broken, highly fractured and serpentinized at the margins. Garnet macrocrysts are completely pseudomorphed by chlorite.

The volcaniclastic kimberlite of the Aaron pipe contains abundant xenoliths of biotite-rich metamorphic country rock. Megacrysts and phenocrysts are broken and fractured. Olivine phenocrysts with fresh cores have margins partially or completely replaced by a fine-grained brownish-red aggregate (Fig. 2.3d), set in a carbonate-rich matrix. The matrix is not uniform, consisting of calcite-serpentine aggregate with abundant opaques or dominated by calcite that forms rounded grains (Fig. 2.3e) surrounded by aggregates of serpentine and clay minerals.

Olivine phenocrysts in the Leslie, Aaron, Grizzly and Torrie kimberlites contain numerous oxide inclusions. The inclusions (1-10 μm) are mainly magnesiochromites but Torrie olivines also contain inclusions of rutile and ilmenite. All oxide inclusions are located within rims of olivine phenocrysts and can often be found in the same olivine grain (Fig. 2.3f). The oxides do not show any particular distribution relative to one another and were probably crystallized at the same stage. The euhedral shape of the oxide minerals indicates crystallization from melt.

Petrographic study of the Leslie and Aaron samples shows that in both of these pipes the degree of secondary alteration increases with depth in the borehole. LS-1, 2, 3 and AN-1 are extremely fresh kimberlites, LS-4 and AN-2 are slightly altered, LS-5 and

AN-3 more altered and AN-4, 5 are volcaniclastic kimberlite and show extensive alteration and contamination by country rock (Fig. 2.2).

2.4. ANALYTICAL METHODS

Electron microprobe analyses of minerals were carried out with a JEOL JXA 8900R electron microprobe (EMP) at the University of Alberta (U of A) and a CAMECA SX50 electron microprobe at the University of British Columbia (UBC). Major and minor elements were determined at 15.0 kV acceleration voltage and a beam current of 20.1 nA (UBC) and 15 nA (U of A) with a 5 μm beam for olivines and a 1 μm beam for chromites, ilmenites and rutile. Analytical conditions were 20 s counting time on peaks for all major elements, 60 s for Ni and 80 s for V and Zn. Data reduction was done with the "PAP" $\varphi(\rho Z)$ method (Pouchou and Pichoir, 1985). Natural and synthetic standards were used for calibration. Analyses obtained for the same chromite grain at both UBC and U of A differ by less than 5% for major elements, by up to 10% for Ti and by more than 10% for V, Mn, Ni, Zn. The Fe^{3+} and Fe^{2+} of the chromites and ilmenites were calculated on the basis of perfect stoichiometry (Droop, 1987).

Whole rock analyses were performed at the Geochemical Laboratories of McGill University, Montreal, Quebec using methods described by Price et al. (2000). The major and trace elements were measured by X-ray fluorescence (XRF) spectrometry, and CO_2 using a LECO induction furnace and absorption bulb. H_2O was calculated as difference between LOI and CO_2.

Oxygen and carbon isotope analyses of whole rock and carbonate fraction were performed at the University of Alberta using a Finnagan MAT 252 mass spectrometer.

Oxygen from silicate was extracted by the BrF_5 technique (Clayton and Toshiko, 1983). C and O from carbonates were liberated using phosphoric acid (McCrea, 1950).

2.4.1. Calculation of $Fe^{3+}/\Sigma Fe$ in oxides

A common problem in the application of oxygen barometers is the uncertainty in the $Fe^{3+}/\Sigma Fe$ of the phases determined by stoichiometry. To address this problem, Wood and Virgo (1989) proposed using of secondary spinel standards with Fe^{3+} determined by Mössbauer to correct stoichiometrically calculated Fe^{3+} in spinel. We analyzed three magnesiochromites with Fe^{3+} known from Mössbauer spectroscopy (Kopylova and McCammon, 2003). The composition of these chromites is very close to the composition of chromite inclusions in kimberlite olivine phenocrysts (Table 2.2). We observed no systematic relationship between Al/Al+Cr and $(Fe^{3+}/Fe_{tot})_{true\text{-}probe}$ for our standards and were thus unable to use the correction of Wood and Virgo (1989), but the chromite standards allowed us to evaluate the possible effect of stoichiometric calculation of Fe^{3+} on the T – fO_2 values. The maximum differences in fO_2 and T calculated for the Fe^{3+} values obtained by both methods are +0.2/-0.7 log units and less than ±50°C respectively (Fig. 2.4), similar to those in the oxygen barometer. We use these values as uncertainties in our calculations.

2.5. MINERAL CHEMISTRY

2.5.1. Olivine

Olivine is the most abundant mineral in kimberlite, occurring as mantle xenocrysts, as large rounded anhedral macrocrysts, and as euhedral and subhedral phenocrysts. Being the most common mineral on the liquidus of kimberlite melt (Mitchell, 1986), olivine

phenocryst compositions can provide information about the melt from which they crystallized. Olivine phenocrysts and xenocrysts in kimberlite cannot be distinguished by composition; only by shape (Mitchell, 1986). We analyzed only euhedral grains (0.3-0.8 mm long) showing parallel extinction that we were confident were the product of melt crystallization. We address the compositional differences between olivine phenocrysts from different kimberlite pipes, the uniformity of olivine populations within one pipe, and examine zoning patterns in some olivines.

Olivine phenocrysts from kimberlites typically show rims with constant composition surrounding cores of diverse compositions. This diversity has been explained by crystallization from different magma batches of kimberlite (Mitchell, 1986). In our samples the cores have the same average Mg-no as the rims but show a much broader range of Mg-no (Fig. 2.5a, Appendix 1).

The different composition of olivine cores can be easily recognized on backscatter electron (BSE) images (Fig. 2.3b). Olivine cores often have irregular shapes with rounded edges similar to dissolution forms. The dark phenocryst cores (Mg-no 0.92-0.93) have low Cr_2O_3 and CaO common for mantle olivines (Larsen and Pedersen, 2000 and references therein). These cores are similar in composition to olivine macrocrysts from the same kimberlite, and their irregular shape indicates that they are likely broken pieces of larger crystals. The largest range in MgO content and the most Fe-rich compositions were observed in phenocryst cores from the Leslie kimberlite (Fig. 2.5c). The origin of the olivine cores is unknown, but the rims we believe are the product of kimberlite melt crystallization. Sharp compositional changes on the rim – core boundary of zoned phenocrysts are inconsistent with diffusive processes and therefore show that the rims grew on cores of a previously existing olivine, and are not the result of re-equilibration

with the groundmass (Fig. 2.6). The Mg-no of the rims from the Leslie, Aaron and Grizzly kimberlites cluster around 92. Rims in the Torrie kimberlite are more Fe-rich (Mg-no 0.91) (Fig. 2.5d) and may indicate different conditions or bulk composition of the melt.

A very exotic composition of an olivine rim (Mg-no 0.97) was recorded in grain LS3-k (Fig. 2.5) from the Leslie kimberlite. The very low NiO-content and extremely high CaO and MnO-content of this olivine indicate crystallization at a very late stage (Fig. 2.5 and Appendix 1) or some significant change in the melt conditions (e.g., higher fO_2).

Phenocryst cores and margins have different Ni, Ca and Mn contents (Fig. 2.7). Cores are higher in NiO than rims (Fig. 2.7a) as was described by Mitchell (1973). In the Leslie kimberlite core compositions form two trends with a positive correlation between Mg-no and NiO that may indicate their different origin (Fig. 2.7c). The rims form two separate groups in terms of NiO-content (Fig. 2.5b, Fig. 2.7a). The higher NiO group plots with the cores. The compositions we used in thermobarometry are all from the low NiO group. The cores contain low CaO, likely reflecting crystallization at high pressures (Simkin and Smith, 1970) (Fig. 2.7b), whereas margins have a larger CaO range. This may suggest a significant decrease of P (change in magma depth) during crystallization of phenocryst margins. The cores from the Leslie kimberlite show a negative trend between CaO and Mg-number, and MnO behaves very similar to CaO.

Thus, the composition of olivine phenocryst cores and rims is uniform in the four pipes. The only exceptions are more Fe-rich composition of the rims from the Torrie kimberlite and a larger compositional range and presence of some compositional trends in the cores from the Leslie kimberlite; which are absent in all the other pipes studied.

2.5.2. Oxides

Oxide minerals are found in kimberlites as macrocrysts of unknown origin, xenocrysts, inclusions in phenocryst olivine and as late groundmass minerals (Mitchell, 1986). The chromite inclusions in olivine phenocrysts in all four kimberlites in this study are titanian aluminous magnesian chromites (according to the classification of Mitchell, 1986) with Cr/(Cr+Al) = 0.7 - 0.9, Mg/(Mg+Fe^{2+}) = 0.59 - 0.64 and 1.1 - 4.2 wt % TiO_2 (Table 2.2). Their composition is distinctively different from magnesian ulvöspinel of the groundmass. Compared to chromite inclusions in the Wesselton kimberlite (Shee, 1984), Lac de Gras chromites have slightly higher Cr, Al, Mg and lower Ti and Fe.

There are compositional variations for chromites among the different kimberlite pipes (Fig. 2.8). All chromites have a similar range of Mg-no, but plot in different fields on a Cr/(Cr+Al) vs Ti diagram. Chromites from the Torrie pipe have lower Cr content than chromites from the three other pipes. The Ti content in chromite increases in the order: Aaron < Grizzly < Leslie< Torrie (Fig. 2.8b). None of the chromites show any significant correlation between Ti and Fe^{3+}/Fe_{tot} (Fig. 2.8c).

Ilmenite inclusions in olivine phenocrysts from the Wesselton kimberlite (Shee, 1984) are distinctively different in composition from other groups of ilmenites found in the same kimberlite. The Torrie ilmenite inclusions (Table 2.3) are very close in composition to those of Wesselton except for two grains (Table 2.3) that have higher MgO similar to groundmass ilmenites from Wesselton. These two inclusions probably came in contact with the latest magma during crystallization of groundmass and their original compositions may have been altered. For geothermometry and oxygen barometry (see below) we used only ilmenites with unaltered compositions.

Rutile forms tabular, euhedral inclusions in olivine (Fig. 2.3f) and is high in Cr_2O_3 (2.6 to 3.6 wt %) and Nb_2O_5 (3.3 wt %)(Table 2.3). The composition of the rutile corresponds to the microphenocrystal olivine paragenesis according to the classification of Mitchell (1995).

2.6. GEOCHEMISTRY

2.6.1. Major element chemistry

Major element compositions for the Leslie and Aaron samples from this study are compared with others from the literature in Table 2.4 and Fig. 2.9. Compared to primitive magma compositions from the Jericho kimberlite, all samples from this study have higher MgO and SiO_2 (Fig. 2.9a). All hypabyssal samples lie on an olivine-control line whereas near-contact samples (LS-5 and AN-3) are displaced from this trend towards a serpentine-control line.

The covariation of Al_2O_3 and SiO_2 is commonly used to distinguish contamination in kimberlites (Mitchell, 1986). All Leslie hypabyssal samples lie within the contamination-free field (Fig. 2.9b) whereas the Aaron hypabyssal samples overlap this field. The Aaron volcaniclastic and Leslie tuffisitic kimberlite breccia samples lie along a trend consistent with contamination from granitoid country rocks (Ward et al., 1995). In all hypabyssal samples the Si/Mg atomic ratio, which can be used as an indicator of crystal contamination (Ilupin and Lutz, 1971; Mitchell, 1986), is less than 0.88 (Table 2.4), characteristic for uncontaminated rocks. Another measure of crustal contamination and/or weathering is the Contamination Index (C.I.) = $(SiO_2+Al_2O_3+Na_2O)/(MgO+2K_2O)$. A value of C.I. less than 1 corresponds to uncontaminated fresh kimberlites (Clement, 1982). In volcaniclastic samples from Aaron, Si/Mg is greater than 0.88 and

C.I. greater than 1 (Table 2.4), indicative of country rock contamination or alteration, consistent with the Al_2O_3 - SiO_2 plot (Fig. 2.9b). The Leslie tuffisitic kimberlite breccia (Berg and Carlson, 1998) has higher C.I. and likely reflects contamination. The Cr and Ni content of hypabyssal samples is higher than in volcaniclastic samples.

2.6.2. Stable isotopes

Stable isotopes were used to estimate the influence of meteoric and magmatic fluids on the emplacement and crystallization of kimberlite magma in the Leslie and Aaron pipes. The carbonate fraction of the Leslie and Aaron kimberlites has a mean $\delta^{13}C_{PDB}$ of -4.9 ‰, similar to the isotopic composition of mantle-derived material (e.g. Kirkley et al., 1989) and close to the Jericho (Price et al., 2000) and Wesselton kimberlite (Kirkley et al., 1989) carbon isotope ratios (Table 2.5). The $\delta^{18}O_{SMOW}$ of the carbonate fraction for samples AN-2, 3 and LS-4 has a mean of 9.5 ‰, and falls within the field of the Wesselton kimberlite representing primary mantle ratios. LS-3 shows enrichment in $\delta^{18}O$ (17.4 ‰) similar to the Jericho carbonates (~ 16.5 ‰). The nature of this enrichment is not well understood, but it is not likely to be a result of interaction with meteoric waters (which have negative $\delta^{18}O$) or of surface weathering processes ($\delta^{18}O$ ~ 26.5 ‰, Sheppard and Dawson, 1975). Other possible explanations for $\delta^{18}O$ enrichment in carbonates include oxygen isotope exchange with magmatic fluid. Extensive crystallization of groundmass serpentine ($\delta^{18}O$ ~ 2 ‰) prior to carbonate crystallization could also shift isotopic ratios of residual liquids to higher $\delta^{18}O$ (Kirkley et al., 1989).

The whole-rock $\delta^{18}O$ values for the Leslie and Aaron kimberlites are –1.5 to 3.7 ‰, lower than those of the Jericho kimberlite (Table 2.5). These values are typical of kimberlite groundmass minerals (serpentine and Fe-Ti oxides with $\delta^{18}O$ of 2 and 3 ‰

respectively) (Sheppard and Dawson, 1975). Sample AN-3, which is close to the contact between hypabyssal and volcaniclastic kimberlite, has a negative $\delta^{18}O$ value, possibly indicating interaction with meteoric fluids along the interface of these two facies.

2.7. GEOTHERMOMETRY AND OXYGEN BAROMETRY

The lack of any significant alteration in olivine phenocrysts and oxide inclusions permits application of thermometers and oxygen barometers to estimate the T and fO_2 of crystallization in kimberlite magma. Fresh euhedral olivines were identified with a petrographic microscope, and further examined with SEM for the presence of oxide inclusions. Any oxide inclusions located on a cracks or in slightly altered parts of olivine grains were ignored.

2.7.1. Olivine-Spinel

For olivine - spinel assemblages the reaction:

$$6\ Fe_2SiO_4 + O_2 = 3\ Fe_2Si_2O_6 + 2\ Fe_3O_4 \qquad (1)$$

olivine orthopyroxene chromite

can be used as an oxygen barometer. An experimentally-calibrated version of this oxygen barometer developed by Ballhaus et al., (1991) requires electron microprobe data for olivine and spinel and the T of equilibration. The composition of the chromite inclusions from the Lac de Gras kimberlites in terms of Mg-, Cr-number and Fe^{3+}/Fe_{tot} is within the range of spinel compositions used in the experimental calibration. The kimberlite chromites, however, contain much higher Ti. Temperatures were determined by the olivine-spinel $FeMg_{-1}$ exchange thermometer ($T_{Ol\text{-}Sp}$) of O'Neill and Wall, (1987) as

simplified by Ballhaus et al., (1991). Results at four different P of equilibration are given in Table 2.6.

The oxygen barometer (Reaction (1)) requires the presence of orthopyroxene. Ballhaus et al. (1991) reported that for orthopyroxene-undersaturated rocks the oxygen barometer produces the maximum fO_2 values. Since silica activity (a_{SiO2}) of kimberlites is well below that required to stabilize orthopyroxene, a correction has to be made to the calculated fO_2 values. The log a^{opx}_{fs} term in the Ballhaus et al. (1991) equation can be substituted with an expression for a_{SiO2} according to the reaction:

$$Fe_2SiO_4 + SiO_2 = Fe_2Si_2O_6 \qquad (2)$$

olivine orthopyroxene

where:

$$\log a^{opx}_{fs} = -\Delta G°(2)/2.303RT + \log a^{ol}_{fa} + \log a\, SiO_2 \qquad (3)$$

Ballhaus et al. (1991) simplified the expression for the oxygen barometer by canceling orthopyroxene against the ideal part of a^{ol}_{Fa}. This simplification is valid for rocks with X^{ol}_{Fe} close to 0.1 and silica activity close to that of the forsterite – enstatite (Fo-En) buffer. The difference in fO_2 values calculated with the oxygen barometer between orthopyroxene-saturated and undersaturated rocks is approximately 3* ($\log a_{SiO2}^{rock} - \log a_{SiO2}^{Fo\text{-}En\ buffer}$). Thus, the corrected fO_2 values can be re-written as:

$$\Delta\log(f_{O2})^{FMQ} = \Delta\log(f_{O2})^{FMQ}(\textit{Ballhaus et al., 1991}) + 3^* (\log a_{SiO2}^{rock} - \log a_{SiO2}^{Fo\text{-}En\ buffer}) \qquad (4)$$

Silica activity is not well known for kimberlites. Mitchell (1973, 1986) proposed that the groundmass mineral assemblages limit a_{SiO2} at a given T and P. The upper limit of a_{SiO2} in kimberlites from this study are constrained by the presence of monticellite, and so lies below the diopside-monticellite (Di-Mnt) buffer:

$$CaMgSiO_4 + SiO_2 == CaMgSi_2O_6 \quad (5)$$

monticellite diopside

Silica activity for Fo/En and Di-Mnt buffers at the T and P of interest was calculated from the Gibbs free-energy changes for the corresponding reactions (Table 2.6) using the thermodynamic data of Holland and Powell (1998). The difference in a_{SiO2} between the Fo/En and Di-Mnt buffers was used to adjust the fO_2 values obtained from the Ol-Sp oxygen barometer (see (4) above) to give the maximum fO_2 for the kimberlite magmas. The results recalculated in ΔNNO units (= log fO_2 sample – fO_2 NNO buffer at P and T) are shown in Table 2.6 and Fig. 2.10.

We assume olivine – chromite co-crystallization most likely occurred at or below 1.0 GPa because monticellite, which limits a_{SiO2}, is not stable at higher P in the melting interval of kimberlite (Edgar et al., 1988).

2.7.2. Olivine-Ilmenite

Olivine phenocrysts from the Torrie kimberlite also contain inclusions of chromites, Mg-rich ilmenites and rutile. The revised Fe-Mg exchange olivine-ilmenite ($T_{Ol\text{-}Ilm}$) thermometer in QUILF-95 (Andersen and Lindsley, 1981; Andersen et al., 1993) can be used to estimate the equilibration temperature of Ol-Ilm assemblages. The QUILF-95 method has been calibrated between 400°C - 1500°C, to 3.2 GPa and X_{gek} = 0 - 1. The calculated $T_{Ol\text{-}Ilm}$ are similar to those recorded by $T_{Ol\text{-}Sp}$ (Table 2.6, Fig. 2.10).

The ilmenites in the Torrie olivines have compositions very similar to bleb-like ilmenite inclusions in euhedral olivine phenocrysts from the Wesselton kimberlites (Shee, 1984) and are distinctively different from macrocryst and groundmass ilmenites. Some of the Torrie ilmenite inclusions contain greater than 18 wt% MgO and correspond to

groundmass ilmenites (Shee, 1984) likely resulting from re-equilibration with the groundmass. In the QUILF-95 calculations these ilmenites show an absence of equilibrium and were not used in the T-fO_2 calculations.

2.7.3. Ilmenite-Rutile

Coexisting ilmenite and rutile inclusions in the Torrie olivine phenocrysts serve as an oxygen barometer based on the reaction:

$$2Fe_2O_3 \text{ (in ilmenite)} + 4TiO_2 \text{ (rutile)} = 4FeTiO_3 \text{ (in ilmenite)} + O_2 \quad (6)$$

(Zhao et al., 1999). We calculated activities a^{Ilm}_{FeTiO3}, a^{Ilm}_{Fe2O3} from Ghiorso and Sack, (1995) for each ilmenite inclusion using $T_{O\text{-}Ilm}$ at 1.0 GPa. The a^{Rut}_{TiO2} is the mole fraction of TiO_2 in rutile. The ilmenite compositions on which the rutile – ilmenite barometer is calibrated are more Fe-rich than the Torrie ilmenites. Nevertheless, the estimated fO_2 values are quite similar to those calculated from the Ol-Sp oxygen barometer when uncorrected for the lower a_{SiO2} in kimberlites (Table 2.6, Fig. 2.10).

2.8. DISCUSSION

2.8.1. Crystallization temperatures and redox regime in kimberlite magma

The values of $T_{Ol\text{-}Sp}$ calculated at 1.0 GPa for olivine rims in the Leslie, Aaron, Grizzly and Torrie kimberlites are between 1030°C and 1170° with a mean value of 1080°C (Fig. 2.10). The whole range of calculated $T_{Ol\text{-}Sp}$ for the four pipes is within the uncertainty of ±50°C. As expected, $T_{Ol\text{-}Sp}$ correlates positively with the Mg-content of the chromites, but such a correlation can also be an artifact of analyzing small chromite inclusions (5-10 μm) in an Mg-rich host phase like olivine. The potential exists for

excitation of the surrounding olivine, increasing the MgO and SiO_2 content of the chromites and as a result, the calculated T. To obviate this problem, we rejected from consideration all chromites with greater than 0.2 wt % of SiO_2. The absence of any correlation between SiO_2 in chromites and $T_{Ol\text{-}Sp}$ suggests that our criteria for rejection are sound. We also believe that these results represent the real crystallization T of kimberlite melt having olivine and chromite on its liquidus for several reasons. Firstly, if the chromite inclusions did not crystallize simultaneously with olivine, they would more likely concentrate along a distinct boundary between the core and rim in olivine grains. On the contrary, chromites are randomly distributed throughout the olivine rims. Secondly, Fe-Mg exchange between spinel inclusions and olivine is very rapid in mafic magma (Scowen et al., 1991), implying equilibrium compositions of olivine – chromite pairs in our samples. Thirdly, the $T_{Ol\text{-}Sp}$ values plot within the olivine + spinel + monticellite ±calcite + liquid fields in the melting interval of kimberlite, and so are consistent with the mineralogy in our samples, and olivine-spinel co-precipitation observed experimentally in kimberlite (Edgar et al., 1988).

We do not know the pressure (P) at which the olivine phenocrysts crystallized, but pressure has only a minor influence on $T_{Ol\text{-}Sp}$ (20°C/GPa) and fO_2 (0.03 log units/GPa). The $T_{Ol\text{-}Sp}$ values from olivine-chromite co-crystallization would be below the kimberlite solidus at pressures greater than 2.0 GPa (Canil and Fedortchouk, 1999, Foley, 1990) so we suggest 2.0 GPa as a maximum value.

$T_{Ol\text{-}Ilm}$ records 1064°C, 1134°C and 1332°C at 1.0 GPa (from QUILF-95, Andersen et al., 1993), similar to $T_{Ol\text{-}Sp}$ when calculated at 1.0 GPa, but differing by more than 150°C at 3.0 GPa (Table 2.6). The only olivine phenocryst (TQ15-n) where both $T_{Ol\text{-}}$

$_{Ilm}$ and $T_{Ol\text{-}Sp}$ can be applied shows only a 35°C difference when calculated at 1.0 GPa, signifying consistency between thermometers, and a suitable assumed P for the calculations.

The range of fO_2 values calculated from coexisting Ol and Sp for the four pipes is from ΔNNO= +0.4 to +0.9 (Fig. 2.10, Table 2.6) at silica activity of the Fo-En buffer. Assuming Ol-Sp co-precipitation at P below 1.0 GPa, and a lower silica activity of the melt limited by the presence of monticellite, the corrected fO_2 values are ΔNNO= -3.0 to –2.2. Application of the Ilm-Ru oxygen barometer to the Torrie samples produces values of ΔNNO= +0.7 and +0.9 (Table 2.6), very close to the Ol-Sp data when not corrected for lower silica activity. As was discussed above, kimberlite ilmenites are more Mg-rich than the compositional range calibrated for the Ilm-Ru oxygen barometer (Zhao et al., 1999). The MgO-content of ilmenites negatively correlates with the calculated *log* fO_2 values suggesting that the Torrie Ilm – Ru assemblage also produces the maximum fO_2 values.

Ballhaus et al. (1991) used Ti-free spinels in their experimental calibration. The high TiO_2 (1-4 wt%) in the kimberlite chromites from this study might have influenced the fO_2 calculation. The absence of a correlation between the Ti-content of our chromites and calculated fO_2 suggests that this is not the case. Furthermore, a study by Andersen et al. (1991) shows that for Mg-rich olivines there is only a minor effect of Ti content in spinels on isopleths of X_{Mg}^{sp} for coexisting ol_{ss}-sp_{ss}.

Fig. 2.11(a) shows that the Ol-Sp assemblages in the margins of olivine phenocrysts records fO_2 values similar to those estimated by Mitchell (1973, 1986) for olivine and magnetite in the groundmass of kimberlite. This suggests that during

kimberlite crystallization from 1100° (Ol-Sp phenocrysts) to 600°C (groundmass) the fO_2 of the melt evolves parallel to the NNO buffer.

2.8.2. Estimation of kimberlite melt composition and amount of accumulated olivine

Olivine-liquid equilibria at known crystallization temperatures in our samples can provide constraints on kimberlite melt compositions along their liquid line of descent, and on the proportions of liquid and olivine from different sources (xenocrysts and phenocrysts) during crystallization. The partitioning of MgO and FeO between olivine and melt is a function of T, P and melt composition (e.g. Langmiur et al., 1992). Using the composition of olivine phenocrysts in our kimberlites and their crystallization temperatures we can determine the MgO and FeO content in the kimberlite liquid that was in equilibrium with these phenocrysts. Different expressions for this relationship have been proposed (Beattie, 1994; Ford et al., 1983; Langmiur et al., 1992; Roeder and Emslie, 1970; Sugawara, 2000). The effect of alkalis in the melt is incorporated in the expression of Langmiur et al. (1992):

$$\mathrm{Ln}(X^{ol}_{MgO}/\ X^{liq}_{MgO}) = 6921/T + 0.034\ Na + 0.63\ K + 0.1154\ P - 3.27 \qquad (7)$$

where T is in Kelvin, P is in kilobars, and compositional terms are in cation mole percent. The calculated MgO content (mol %) for the Leslie and Aaron kimberlite liquids in equilibrium with the olivine phenocrysts are shown on Fig. 2.12. Due to the presence of H_2O and CO_2, kimberlites may crystallize Mg-rich olivines at a T much lower than that of other mantle-derived igneous rocks, resulting in an underestimation of the MgO content in the liquid in equilibrium with olivine. Therefore, the values shown on Fig. 2.12 are lower limits for kimberlite melt composition.

Some constraints can be placed on the proportions of liquid and olivine (xenocrysts and phenocrysts) during crystallization of the olivine phenocryst rims. Mass-balance of bulk rock MgO and FeO of the unaltered kimberlite samples (LS-1, 2, 3, 4 and AN-1, 2, 6, 7) with olivine and the melt composition calculated using $K_{D\ ol\text{-}liq}^{FeMg}$ is shown on Fig. 2.12a. Melt compositions will plot along the line determined by distribution coefficient of MgO and FeO between olivine and liquid established by Roeder and Emslie (1970) and independent on T (Fig. 2.12a). A tie-line between melt compositions along this line and the most Mg-rich olivine cores ($Fo_{94.2}$ in Table in Appendix 1) recorded in our samples provide the upper constraints on the proportion for melt (28 mol%) and accumulated olivine (72 mol%). A lower limit of 11 mol% liquid and 89 mol% of accumulated olivine is constrained by the calculated MgO and FeO content of the kimberlite melt (Fig. 2.12a). For simplicity all compositions on Fig. 2.12a were recalculated with all iron as FeO due to the reduce nature of our kimberlite and low Fe^{3+}/Fe_{tot} values estimated for the Leslie and Aaron kimberlites by the method of Kress and Carmichael (1988) at the T and fO_2 determined from Ol-Sp thermobarometry.

Constrains on the amounts of mantle xenocrysts and earlier phenocrystic olivine accumulated in the melt, requires knowledge of the composition of kimberlite melt when it first reached its liquidus. Some approximations for the primary kimberlite melt are aphanitic kimberlites from the Wesselton mine (South Africa) (Edgar et al., 1988) and from the Jericho pipe (N.W.T., Canada) (Price et al., 2000). The MgO/FeO ratios of the latter primary kimberlite liquids evolve during olivine fractional crystallization along the lines (with arrows) shown on Fig. 2.12b and reach the MgO/FeO ratio of the kimberlite melts equilibrated with Ol-Sp assemblage in this study after crystallization of 41, 37 and 26 mol% of olivine respectively (Table 2.7).

The tie-lines between the compositions of the Jericho and Wesselton aphanitic kimberlites and mantle olivine give the proportion of xenocrysts accumulated in these melts (Fig. 2.12b). The amount of earlier generations of phenocrysts present in the melt by the time of Ol-Sp co-precipitation in rims can be then calculated (Table 2.7). For all three inferred primary melt compositions, the mole proportion of olivine phenocrysts present in the kimberlite melt during Ol-Sp crystallization is 10 mol% (Table 2.7) regardless of the primary composition the kimberlite melt which is unknown. Kimberlites in this study contain between 11 and 28 mol% liquid, 10 mol% of the earlier generations of phenocrysts, and 62 to 79 mol% of accumulated mantle olivine.

2.8.3. Application to diamond dissolution

Diamonds in transit to the Earth's surface in kimberlite can undergo transformation into graphite, or oxidation into CO_2 or carbonate. These processes are widely observed in natural diamonds as resorption resulting in rounded crystals, etching, or frosting, and can lead to the complete destruction of diamond, with significant decreases in the economic grade of a kimberlite pipe. It is not well understood whether the resorption of diamonds occurs in the mantle during kimberlite accumulation and ascent to shallower levels (Harris, 1987; Taylor et al., 1995), or during emplacement in kimberlite magma (Robinson et al., 1989). There is also the potential for reaction of diamonds with heated meteoric waters during surface eruptions (Sheppard and Dawson, 1975).

High-temperature kimberlite melt is a very reactive media for diamonds and can possibly cause resorption. The degree and kinetics of diamond dissolution are controlled by T, fO_2 and fCO_2 (e.g. Arima, 1998). Assuming that Ol-Sp co-crystallization occurred below 1.0 GPa, the maximum fO_2 values of kimberlite magmas (at a silica activity of the

Di-Mnt buffer) are in graphite stability field very close to the position of GCO buffer (Fig. 2.11). With a decrease in P, fO_2 values shift into the field of CO_2 stability. Thus, any diamonds liberated from xenoliths at depth experienced dissolution in the graphite stability field while stones coming in contact with the magma at the latest stages of eruption might have been resorbed in the CO_2 stability field. Diamond dissolution experiments in silicate melt at conditions within the graphite stability field (Arima, 1998, Sonin et al., 1997) produced resorption features similar to those recorded in natural diamonds, in agreement with our fO_2 data.

The present study allows us to evaluate the possible T – P – fO_2 path of the Lac de Gras kimberlites at depth. According to Carmichael (1991), the redox state of erupted magmas is determined in their source region. Extrapolating the calculated fO_2 conditions to higher T and P in the mantle (Fig. 2.13) shows that these kimberlites transported diamonds through the graphite stability field well below the D/GCO buffer without carbonatization.

The Ol-Sp thermometry and oxygen barometry can potentially be applied to kimberlite pipes that show significant differences in the degree of resorption of their diamond populations. Correlation of any of the dissolution features in diamonds with T and fO_2 of kimberlite magmas may help to better understand the nature of the resorption process, or possibly to predict the degree of diamond preservation in a particular pipe.

2.9. CONCLUSIONS

Inclusions of chromites are common in margin zones of olivine phenocrysts in hypabyssal and volcaniclastic kimberlites from the Leslie, Aaron, Grizzly and Torrie in the Lac de Gras area and can be used for estimation of T and fO_2 in kimberlite magmas.

$T_{Ol\text{-}Sp}$ shows that the margins of olivine phenocrysts crystallized at 1030°C (Leslie) - 1170°C (Torrie) at the maximum fO_2 of ΔNNO –3.0 to –2.2 (calculated at 1.0 GPa and silica activity of the melt limited by the presence of monticellite).

Mass balance of the melt equilibrated with olivine phenocryst rims and bulk rock suggests crystallization of the olivine – chromite assemblage from a magma that contains between 11 and 28 mol% of liquid, 10 mol% of earlier precipitated olivine phenocrysts and between 62 and 79 mol% of mantle xenocryst olivine.

The T – fO_2 values obtained for four Lac de Gras kimberlites show that the diamonds entrained in these kimberlites ascended in the stability fields of graphite. At the latest stages of eruption (below 0.1 GPa) moving into CO_2 stability field is possible.

ACKNOWLEDGEMENTS

We sincerely thank Jon Carlson and BHP/Billiton Diamonds Inc. for access to drill core, for support and suggestions during sampling and permission to publish. L. Shi and M. Raudsepp provided assistance with EMP analyses at U of A and UBC, respectively. M. Raudsepp is greatly thanked for valuable suggestions during microprobe work. We especially thank M. Kopylova and C. McCammon for providing us the chromite grains with Fe^{3+} measured by Mössbauer spectroscopy. The manuscript has been improved by the review of N. Green, A. Woodland and J.K. Russell. This research was supported by a UVic graduate scholarship to YF and NSERC of Canada Discovery grant to DC.

Table 2.1 Composition and age of the Leslie, Aaron, Grizzly and Torrie kimberlites

Locality	Age (Ma)	Kimberlite facies	Equilibration T&P of mantle xenoliths
Leslie pipe	52.7±2.9*	mainly hypabyssal with a remnant of tuffistic kimberlite breccia (TKB)	eclogites 725 –1438°C at 2.5-8.5 GPa (Fung, 1998)
Aaron pipe	45.2±1.3*	pelletal volcaniclastic and hypabyssal	
Grizzly pipe	50.8 ±4.8*	macrocrystic, heterolithic hypabyssal	650 - 1200°C at 2.1 – 6.2 GPa (Boyd & Canil, 1997)
Torrie pipe	late Cretaceous-early Paleocene**	macrocrystic, heterolithic, volcaniclastic kimberlite tuff and tuff breccia	849 – 1350°C at 2.4 to 6.0GPa (MacKenzie & Canil, 1999)

* - based on Rb-Sr systematics on phlogopite macrocrysts (Creaser et al., 2003)
** - from palynology (Nassichuk & McIntyre, 1995).

Table 2.2 Analyses of chromite inclusions in olivine phenocrysts from the Leslie, Aaron, Grizzly and Torrie kimberlites

Sample	MgO	Al2O3	SiO2	CaO	TiO2	V2O3	Cr2O3	MnO	FeO	Fe2O3*	NiO	ZnO	Total	Fe3+/Fetot stoichiometry*	Fe3+/Fetot Mössbauer**
Leslie Pipe															
LS2-n	13.35	8.29	0.14	0.03	3.08	0.00	51.8	0.10	14.97	6.50	0.22	0.04	98.56		
LS2-k-2	12.86	8.37	0.17	0.10	2.90	0.00	52.5	0.15	15.57	5.78	0.17	na	98.55		
LS2-m-1b	12.90	8.09	0.15	0.04	2.67	0.00	53.6	0.09	15.47	5.64	0.14	na	98.82		
LS2-m-2	12.53	7.85	0.10	0.11	2.56	0.01	53.7	0.15	15.54	5.81	0.16	na	98.48		
Aaron Pipe															
AN1-l	12.94	7.48	0.13	0.06	1.42	0.10	57.1	0.17	14.13	5.40	0.10	0.08	99.08		
AN1-k	12.70	7.79	0.13	0.00	1.41	0.18	56.4	0.12	14.58	5.51	0.16	0.08	99.09		
AN5-b-1B	13.33	8.74	0.16	0.04	1.11	0.14	56.0	0.07	13.15	6.10	0.16	na	98.95		
AN5-c-2B	12.42	5.40	0.12	0.04	1.21	0.06	59.9	0.14	14.26	5.24	0.12	na	98.87		
Grizzly Pipe															
Gr43-k2	13.68	9.73	0.19	0.01	1.61	0.11	54.0	0.11	13.73	6.10	0.18	0.11	99.58		
Gr43-e	13.18	7.49	0.13	0.06	2.07	0.05	55.3	0.22	14.38	6.66	0.16	0.16	99.82		
Gr43-a1	12.91	7.54	0.09	0.05	1.74	0.01	56.4	0.19	14.50	5.74	0.09	0.07	99.33		
Torrie Pipe															
TQ13-h-1	13.90	13.65	0.10	0.04	3.02	0.00	47.3	0.07	15.01	5.44	0.21	na	98.76		
TQ17-f-1	13.97	10.91	0.12	0.21	4.18	0.00	46.8	0.17	15.17	6.83	0.19	na	98.55		
TQ15-n	13.56	9.10	0.18	na	4.53	0.31	46.9	0.34	15.72	6.94	0.18	na	97.79		
TQ-18E-3	13.59	11.07	0.14	0.08	3.39	0.00	48.2	0.09	16.29	5.65	0.16	na	98.71		
Chromite Standards from Jericho xenoliths				**											
11-18-A	13.40	23.26	0.01	0.00	0.01	0.18	46.5	0.12	14.66	0.88	0.07	na	99.09	0.078	0.051
9-12-A	12.04	16.64	0.01	0.01	0.02	0.20	53.2	0.13	15.12	1.72	0.06	na	99.14	0.087	0.093
10-12a-A	10.60	11.68	0.01	0.01	0.08	0.32	54.1	0.16	17.84	4.47	0.08	na	99.34	0.253	0.184
11-18-B	13.30	23.21	0.00	0.01	0.02	0.20	46.5	0.11	14.63	0.87	0.08	na	98.89	0.075	0.051
9-12-B	12.14	16.67	0.01	0.00	0.02	0.20	53.8	0.10	15.24	1.74	0.04	na	99.92	0.085	0.093
10-12a-B	10.65	11.82	0.01	0.00	0.08	0.31	54.2	0.12	18.03	4.52	0.08	na	99.81	0.253	0.184

na - not analyzed

* - Fe3+ calculated using method of Droop (1987)

** - Fe3+ calculated from Mössbauer spectroscopy (Kopylova &McCammon, 2003)

Table 2.3 Analyses of Ilmenites and Rutile (the Torrie kimberlite)

NN	Samples	MgO	Al2O3	SiO2	CaO	TiO2	Cr2O3	MnO	Fe2O3*	FeO	NiO	Nb2O5	Ta2O5	Total
1	TQ15-n	17.06	0.15	0.06	0.03	53.5	3.95	0.37	6.56	17.23	0.15	0.08	0.00	99.16
2	TQ13-I-1	16.37	0.41	0.09	0.06	52.8	3.27	0.29	6.66	18.45	0.16	0.20	0.00	98.78
3	TQ13-I-2	17.04	0.21	0.08	0.07	52.7	5.03	0.22	5.82	17.07	0.14	0.16	0.00	98.50
4	TQ13-a-2	20.18	0.27	0.04	0.07	53.9	5.00	0.40	6.78	12.33	0.12	0.16	0.00	99.21
5	TQ13-I-2B	17.68	0.54	0.12	0.04	51.4	4.65	0.35	8.69	14.79	0.15	0.17	0.00	98.61
6	TQ13-c-2	0.67	0.00	0.23	0.11	92.0	2.61	0.00		0.76	0.00	2.98	0.16	99.53
7	TQ13-g-2	0.12	0.00	0.19	0.04	91.4	2.98	0.00		0.59	0.00	3.32	0.22	98.91
8	TQ17-b-1	0.04	0.00	0.06	0.03	90.7	3.61	0.00		0.41	0.01	3.36	0.65	98.86

analyses 1-3 - inclusions in olivine phenocrysts
analyses 4,5 - ilmenites re-equilibrated with groundmass
analyses 6-8 – rutile
* - Fe3+ calculated using method of Droop (1987)

Table 2.4 Major (wt %) and trace element (ppm) compositions of Leslie and Aaron kimberlites from the present study and from Berg and Carlson (1998) and Jericho primitive kimberlite from Price et al. (2000)

Sample	LS-1	LS-2	LS-3	LS-4	LS-5	AN-1	AN-2	AN-3	AN-4	AN-5	AN-6	AN-7	LDC-07-220	LDC-09-140	LDC-03-427	JD69	JD82
SiO_2	33.59	33.33	33.43	33.98	34.04	35.62	35.30	36.23	46.07	46.30	35.34	36.52	31.67	32.71	43.00	27.00	28.13
TiO_2	0.48	0.49	0.51	0.45	0.44	0.33	0.32	0.28	0.20	0.19	0.342	0.347	0.66	0.52	0.21	0.51	0.71
Al_2O_3	1.63	1.51	1.53	1.62	2.53	1.71	1.65	2.16	2.64	2.84	1.83	1.85	1.23	1.51	2.40	1.33	1.61
Fe_2O_3	8.34	8.32	8.53	8.14	7.55	8.31	8.37	7.40	6.38	6.35	8.39	8.65	9.24	8.65	7.42	6.04	7.32
MnO	0.16	0.16	0.16	0.15	0.13	0.15	0.15	0.13	0.10	0.09	0.158	0.162	0.17	0.16	0.11	0.14	0.16
MgO	40.07	40.36	41.18	39.87	35.77	40.87	41.37	35.75	30.61	30.28	40.21	40.83	40.93	39.53	34.27	22.39	23.09
CaO	6.74	7.09	8.44	6.41	5.82	4.68	5.64	4.48	2.79	2.77	6.34	3.76	8.09	8.40	4.28	19.37	16.66
Na_2O	0.23	0.20	0.19	0.25	0.18	0.08	0.13	0.19	0.13	0.26	0.12	0.13	0.00	0.03	2.55	0.15	0.19
K_2O	0.30	0.18	0.07	0.56	1.76	0.25	0.51	1.68	1.36	1.70	0.31	0.35	0.40	0.27	3.22	0.43	0.46
P_2O_5	0.41	0.37	0.33	0.39	0.34	0.37	0.26	0.34	0.15	0.18	0.348	0.394	0.26	0.40	0.34	0.61	0.78
CO_2	2.00	2.35	1.73	2.61	4.05	2.41	2.89	3.13	1.67	2.90	2.68	1.67				14.01	12.06
H_2O^*	5.57	4.99	3.73	5.37	6.99	5.00	3.49	7.94	7.70	6.25	3.36	4.73				7.10	6.70
Total	100.28	100.11	100.67	100.59	100.26	100.58	100.78	100.37	100.25	100.55	98.65	98.519	99.45	99.44	100.64	99.44	98.45
LOI	7.57	7.34	5.46	7.98	11.04	7.41	6.38	11.07	9.37	9.15	6.04	6.4	5.59	6.26	2.08		
C.I.	0.87	0.86	0.85	0.87	0.94	0.90	0.87	0.99	1.47	1.47	0.91	0.93	0.79	0.85	1.18	1.22	1.25
Si/Mg	0.66	0.65	0.64	0.67	0.74	0.68	0.67	0.79	1.18	1.20	0.68	0.69	0.61	0.65	0.98	0.94	0.95
Cr_2O_3	3433	3406	3378	3144	2609	3257	3302	2466	1593	1699	3269	3242				1917	2635
Ni	1696	1698	1694	1710	1571	1760	1790	1590	1537	1453	1784	1856				1099	1367
Sc	17	12	11	16	7	9	14	8	5	8							
V	74	72	85	118	72	73	56	41	60	53	61	67					
FeO^{**}	6.98	6.96	7.14	6.84	6.34	7.01	7.06	6.21	5.36	5.34	7.08	7.30	7.76	7.26	6.23	3.5	4.17
$Fe_2O_3^{**}$	0.59	0.59	0.60	0.54	0.50	0.51	0.52	0.49	0.43	0.42	0.52	0.54	0.62	0.58	0.49	2.15	2.69

LOI - loss on ignition

* - H_2O was calculated by subtraction of CO_2 from LOI

** - For LS-1-5 and AN-1-7 calculated by method of Kress and Carmichael (1988) at the T and fO_2 determined from Ol-Sp thermobarometry (Ballhaus et al., 1991) for Ol-Sp co-crystallization and for JD69 and JD82 from Price et al.(2000)

C.I. (Contamination Index) = $(SiO_2+Al_2O_3+Na_2O)/(MgO+2K_2O)$ after Clement (1982)

Si/Mg - atomic weight ratio after (Mitchell, 1986 and references therein)

Table 2.5 Carbon and oxygen isotopic composition of hypabyssal facies of the Leslie and Aaron kimberlites compared to the isotope data from the Wesselton (Kirkley et al., 1989) and Jericho (Price et al., 2000) kimberlites. The data are reported in standard 'δ' notation in parts per thousand with respect to PDB for carbon and SMOW for oxygen. Standard deviation is shown for the Jericho and Wesselton data in the brackets.

Sample	Carbonate fraction		Whole rock
	$\delta^{13}C_{PDB}$	$\delta^{18}O_{SMOW}$	$\delta^{18}O_{SMOW}$
LS-4 (n=2)	-5.3	10.9	1.0
LS-3	-4.1	17.4	3.7
AN-3	-5.3	8.4	-1.5
AN-2	-4.5	9.2	1.6
Wesselton (mean)	-6.4 (0.8)	11.7 (2.6)	
Jericho kimberlite			
JD51	-5.2 (0.1)	16.6 (0.2)	8.2 (1.4)
JD69	-4.5 (0.1)	16.1 (0.2)	6.2 (1.4)
JD82	-4.8 (0.1)	16.3 (0.2)	6.4 (1.4)

Table 2.6 Equilibrium temperatures and oxygen fugacities calculated for Leslie, Aaron, Grizzly and Torrie kimberlites by Ol-Sp, Ol-Ilm and Ru-Ilm thermobarometery

Sample		Ol-Sp T, °C[a]				Ol-Sp Oxygen fugacity[b]			log a_{SiO2}[c]			Ol-Ilm T,°C[e]		Ilm-Ru Oxygen fugacity[f]	
olivine	oxide	0.1 GPa	1 GPa	3 GPa	5 GPa	$\Delta \log fO_2^{FMQ}$	$\log fO_2$	ΔNNO	Di-Mont	En-Fo	corr ΔNNO[d]	1 GPa	3 GPa	$\log fO_2$	ΔNNO
LS2-n-m	LS2-n		1085	1102	1138	1173	1.3	-7.7	0.9	-1.63	-0.52	-2.47			
LS2-h-3	LS2-k-2	1033	1049	1084	1118	1.1	-8.6	0.7	-1.72	-0.55	-2.81				
LS2-m-1	LS2-m-1b		1029	1044	1079	1114	1.1	-8.7	0.7	-1.73	-0.55	-2.87			
LS2-m-2	LS2-m-2	1015	1031	1065	1099	1.1	-8.8	0.7	-1.75	-0.56	-2.85				
AN1-l-m	AN1-l		1044	1061	1097	1132	0.9	-8.6	0.5	-1.70	-0.54	-2.99			
AN1-k-m	AN1-k		1037	1053	1089	1125	0.9	-8.7	0.5	-1.71	-0.55	-3.04			
AN5-b-1	AN5-b-1B		1067	1084	1121	1159	1.1	-8.1	0.6	-1.66	-0.53	-2.74			
AN5-c-2	AN5-c-2B		1037	1053	1088	1123	0.9	-8.7	0.5	-1.71	-0.55	-3.01			
Gr43-k2	Gr43-k2	1057	1074	1111	1148	1.1	-8.2	0.7	-1.67	-0.54	-2.75				
Gr43-e-c	Gr43-e		1096	1113	1149	1186	1.2	-7.6	0.8	-1.61	-0.51	-2.52			
Gr43-a1-m	Gr43-a1		1082	1098	1135	1172	0.9	-8.1	0.5	-1.63	-0.52	-2.89			
TQ13-h-1	TQ13-h-2	1050	1067	1104	1142	0.8	-8.6	0.4	-1.69	-0.54	-3.06				
TQ17-f-1	TQ17-f-2		1123	1140	1177	1215	1.3	-7.2	0.9	-1.57	-0.50	-2.32			
TQ-18E-2	TQ-18E-3		1030	1046	1081	1117	1.0	-8.7	0.6	-1.72	-0.55	-2.92			
TQ15-n	TQ15-n	1153	1169	1206	1243	1.3	-6.8	0.9	-1.52	-0.48	-2.21	1134	1327	-7.4	0.7
TQ13-l-1	TQ13-l-1											1064	1249	-8.2	0.9
TQ13-l-1	TQ13-l-2											1332	1557	-5.3	0.7

a Temperatures calculated from $FeMg_{-1}$ Ol-Sp thermometer Ballhaus *et al.* (1991) and O'Neill & Wall (1987)

b Oxygen fugacities at 1 GPa calculated relative to FMQ buffer from the oxygen barometer by Ballhaus *et al.*(1991)

c Silica activity of diopside-monticellite (Di-Mont) and enstatite-forsterite (En-Fo) buffers calculated using thermodynamic data of Holland&Powell (1998)

d Corrected maximum values of oxygen fugacities of kimberlites calculated for silica activity of diopside - monticellite buffer

e Temperatures calculated for olivine-ilmenite assemblage by QUILF-95

f Oxygen fugacities at 1 GPa calculated from equation (6) Zhao *et al.* (1999)

Table 2.7 Proportions of magma constituents and melt composition during crystallization of Ol – Sp assemblage calculated for the composition of primary kimberlite melt correspondent to the aphanitic kimberlites from Jericho pipe (N.W.T., Canada, Price et al., 2000) and Wesselton mine (South Africa, Edgar et al., 1988).

Primary Melt	J-69	J-82	W
Magma composition during Ol rims crystallization			
mantle olivine, mol%	75	73	63
phenocryst olivine, mol%	10	10	10
melt, mol%	15	16	27
Melt equilibrated with Ol – Sp assemblage			
MgO, mol%	12.2	15.7	25.5
FeO, mol%	3.7	4.8	7.7
Product of Ol fractional crystallization			
Ol phenocrysts, mol%	41	37	26
melt, mol%	59	63	74

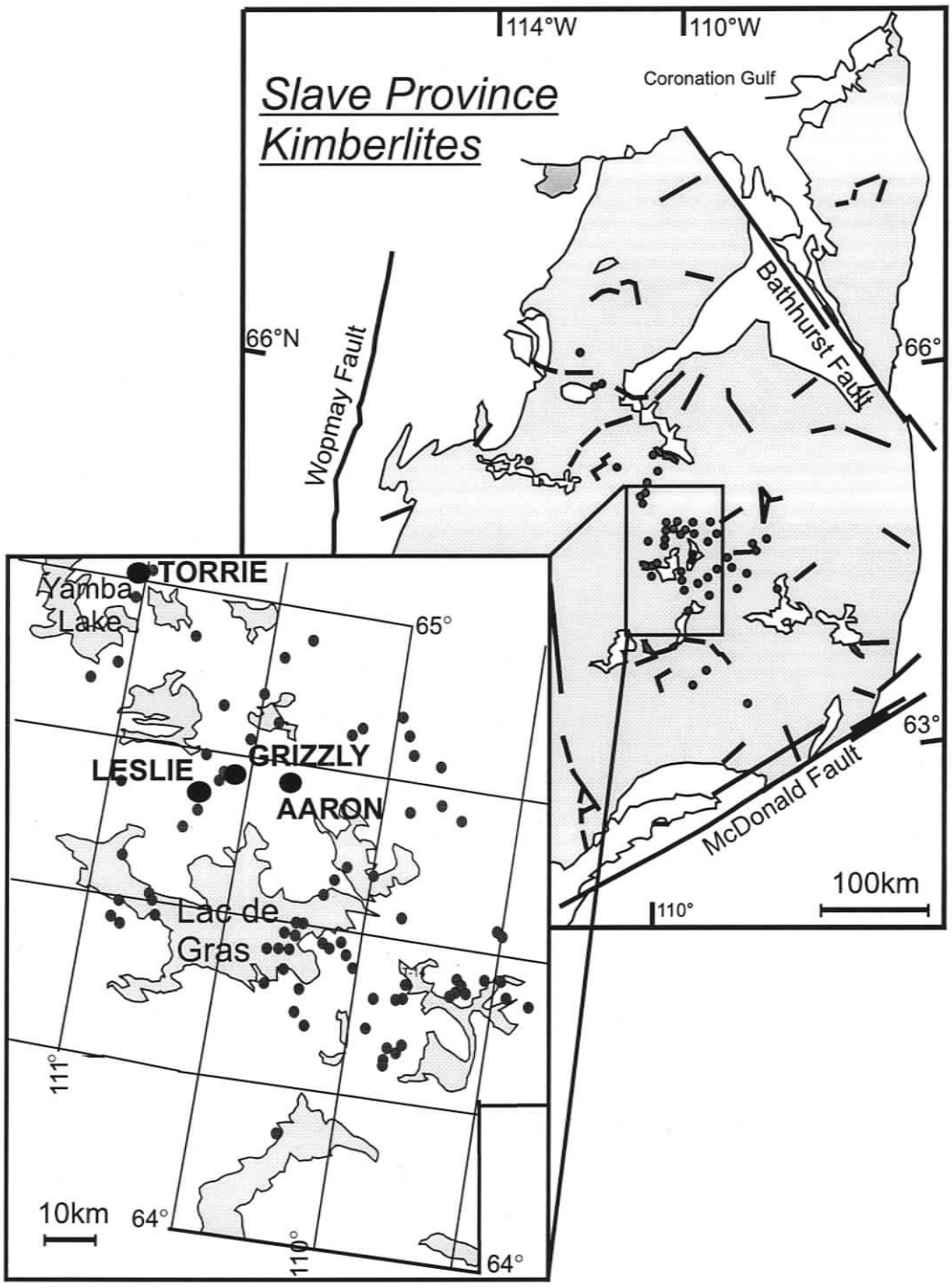

Figure 2.1 Location map showing distribution of kimberlite pipes in the Lac de Gras area (from Ward *et al.*, 1995 and references therein).

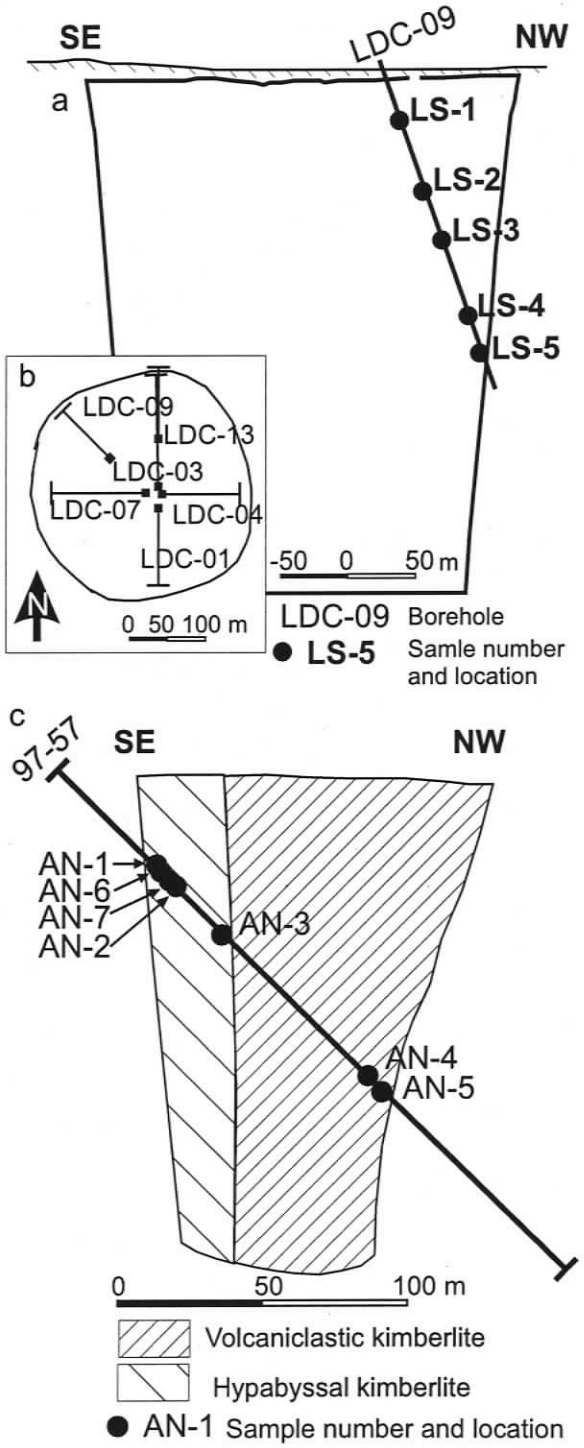

Figure 2.2 (a) Cross-section of the Leslie kimberlite pipe showing the location of borehole LDC-09 and the samples used in this study. Inset (b) is a plan view of the Leslie pipe with drill hole locations (from Berg & Carlson, 1998) (c) Cross-section of the Aaron kimberlite pipe showing location of drill hole 97-57 and the samples used in this study.

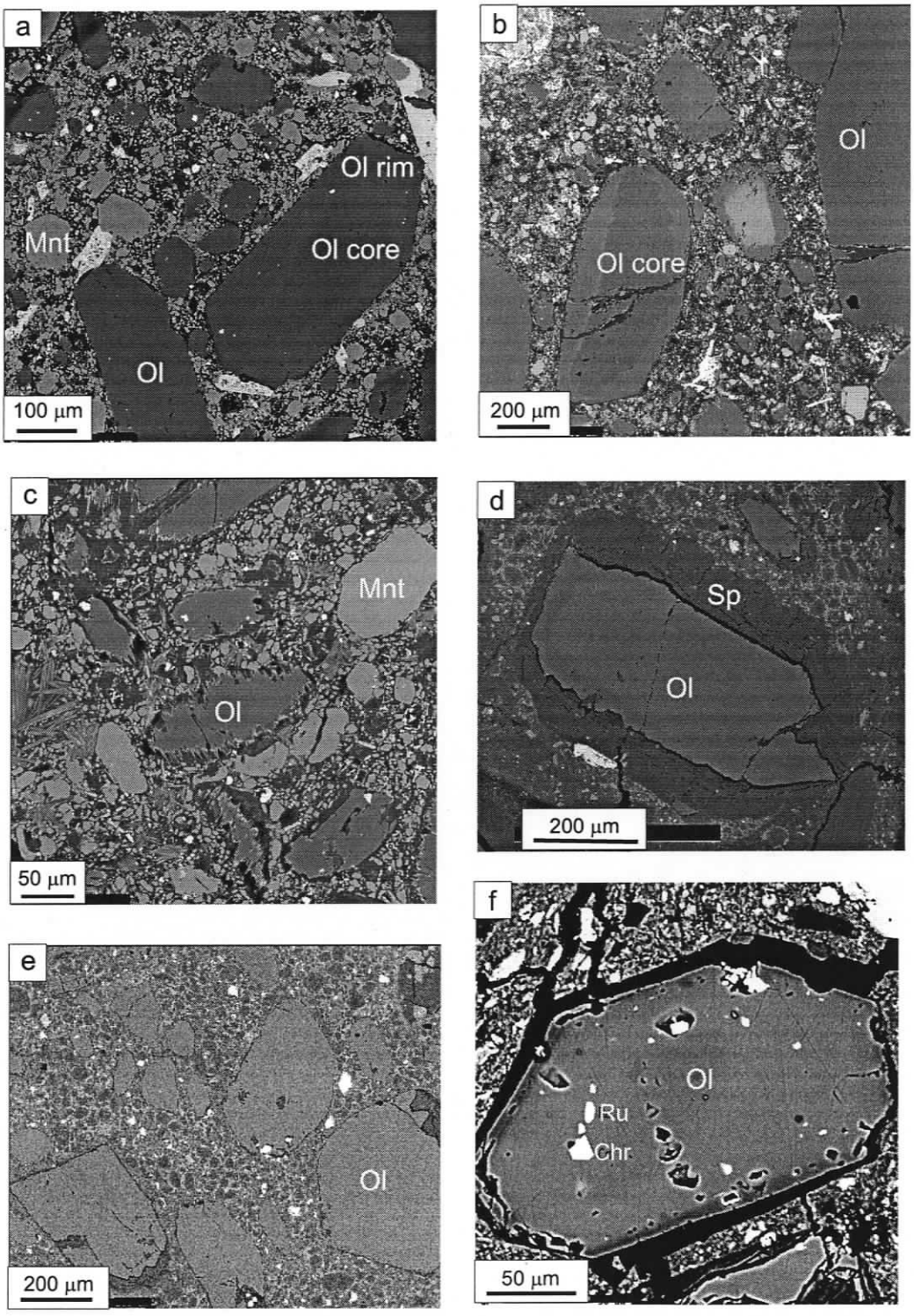

Figure 2.3 Back scattered electron images of kimberlites with scale bars shown. (a) Macrocrystic hypabyssal monticellite kimberlite (LS-3). (b) Normal and reverse zoning in olivine phenocrysts (LS-2). (c) Microphenocrysts of olivine and monticellite in groundmass of hypabyssal facies kimberlite (LS-1). (d) Serpentinization of olivine rim in diatreme facies kimberlite (AN-4). (e) Calcite- and serpentine-rich groundmass in diatreme facies kimberlite (AN-4). (f) Euhedral chromite and rutile inclusions in margins of olivine phenocryst from the Torrie kimberlite.

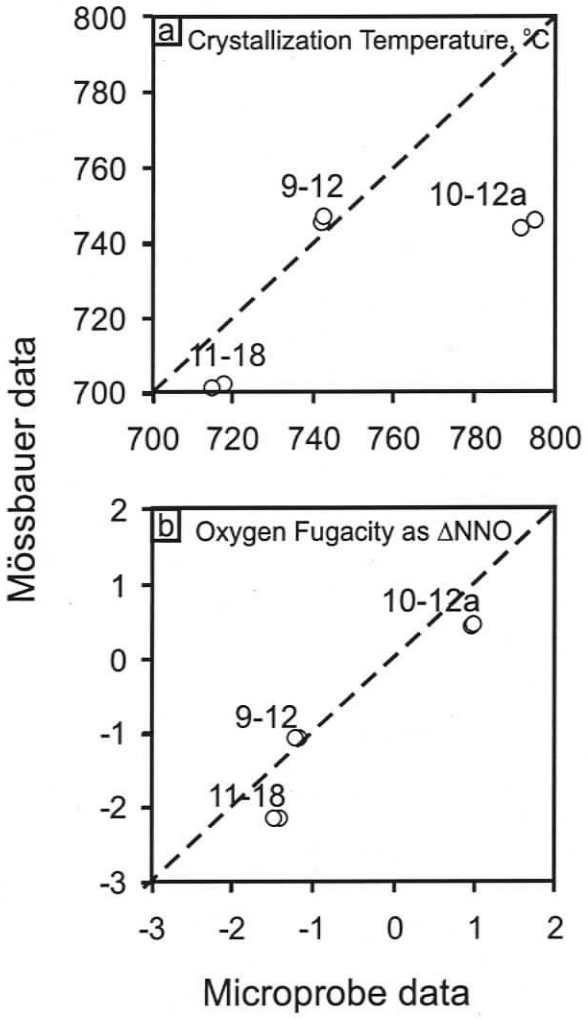

Figure 2.4 Ol-Sp crystallization temperatures (A) and oxygen fugacity shown in ΔNNO units (= log fO_2 sample - fO_2 NNO buffer at P and T) (B) plotted against Fe^{3+}/Fe_{tot} of the chromites known from Mössbauer spectroscopy (Kopylova and McCammon, 2003) and calculated from stoichiometry. The plot shows that the errors produced in T fO_2 values due to stoichiometric calculation of Fe^{3+}/Fe_{tot} in chromites are within the uncertainties of the thermobarometer.

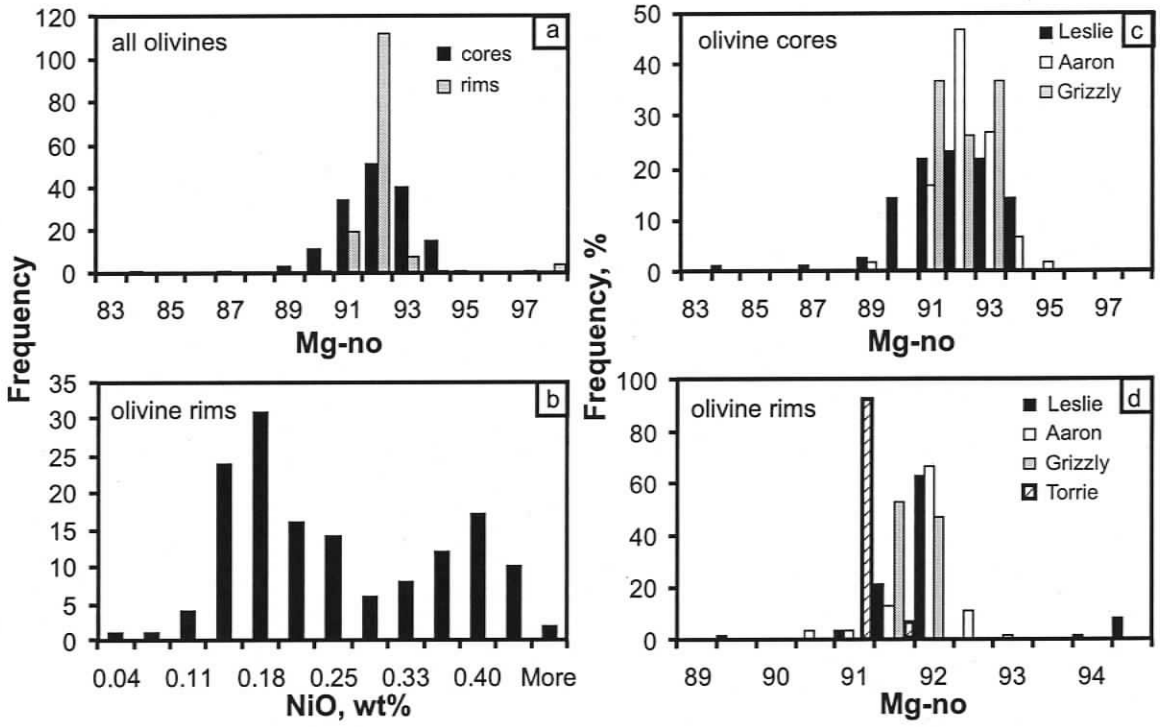

Figure 2.5 Histograms of olivine phenocryst compositions from the Leslie, Aaron, Grizzly and Torrie kimberlites: (a) distribution of Mg-no (Mg/Mg+Fe) in the olivine cores and rims, (b) distribution of NiO-content in the olivine rims, (c) distribution of Mg-no in the olivine cores and (d) in the olivine rims from different kimberlite pipes.

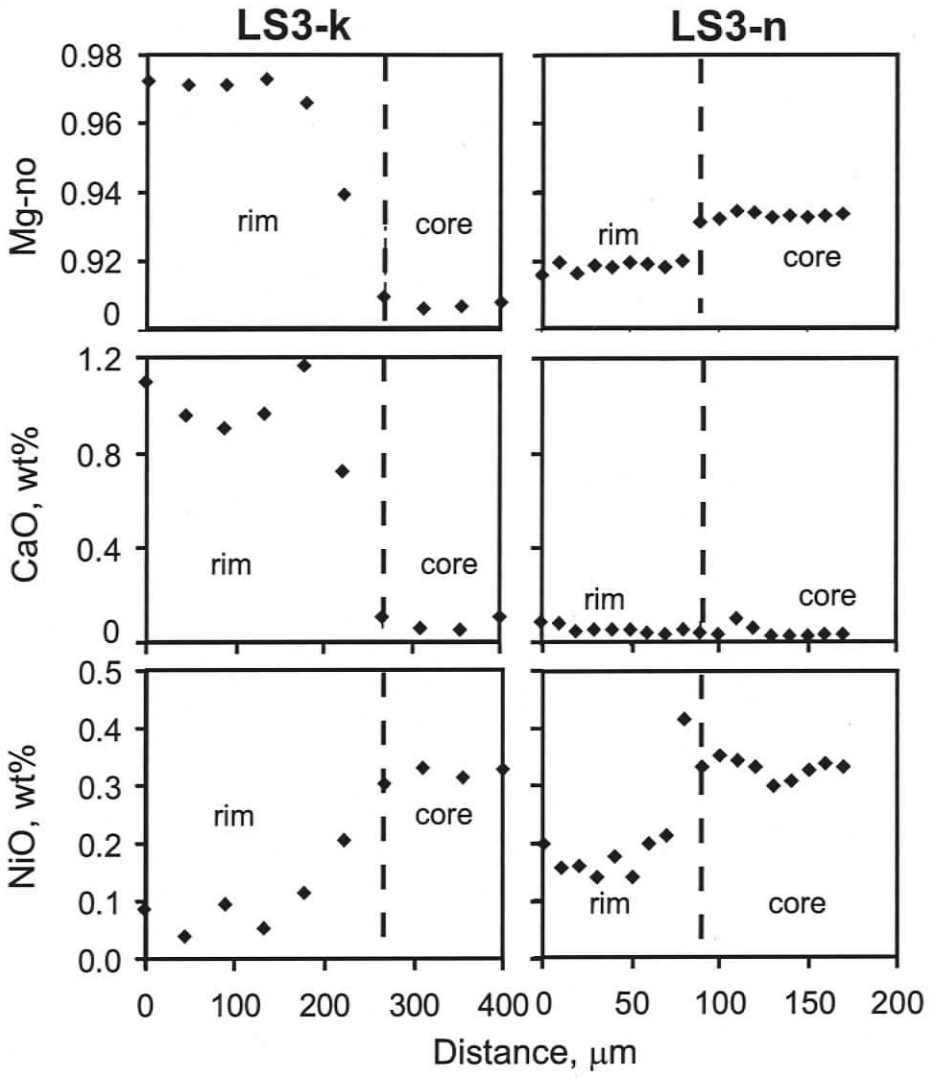

Figure 2.6 Element profiles in zoned olivine phenocryst illustrating sharp compositional changes between the rim and core of olivine.

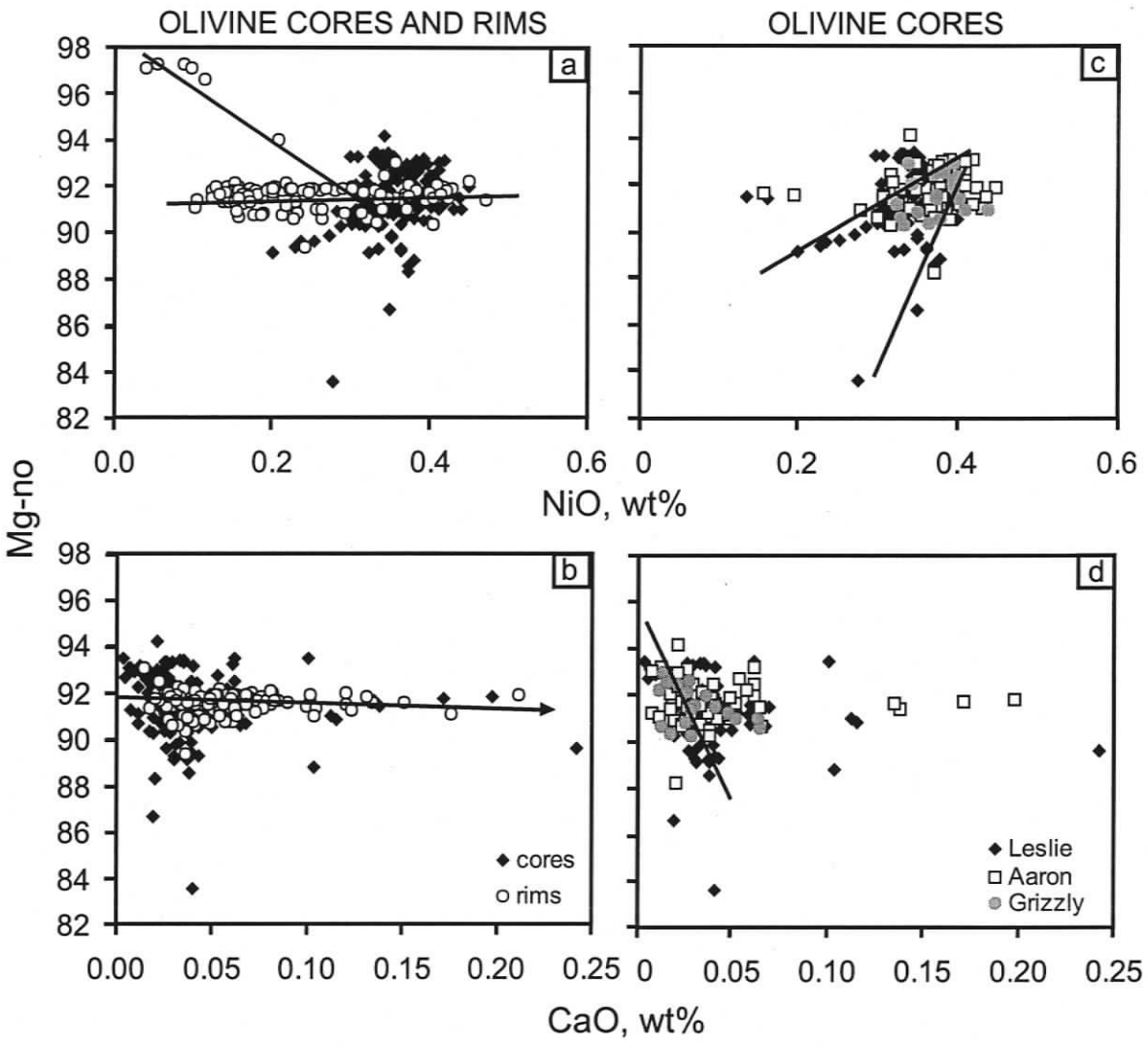

Figure 2.7 Composition of olivine cores and rims in the Leslie, Aaron, Grizzly and Torrie kimberlites. (a) Mg-no vs NiO (wt%) and (b) Mg-no vs CaO (wt%) for the cores and rims in phenocryst olivine. The crystallization trends for the rims is shown. (c) Mg-no vs NiO (wt%) and (d) Mg-no vs CaO (wt%) for olivine cores from different kimberlite pipes with the crystallization trends for the Leslie olivines shown.

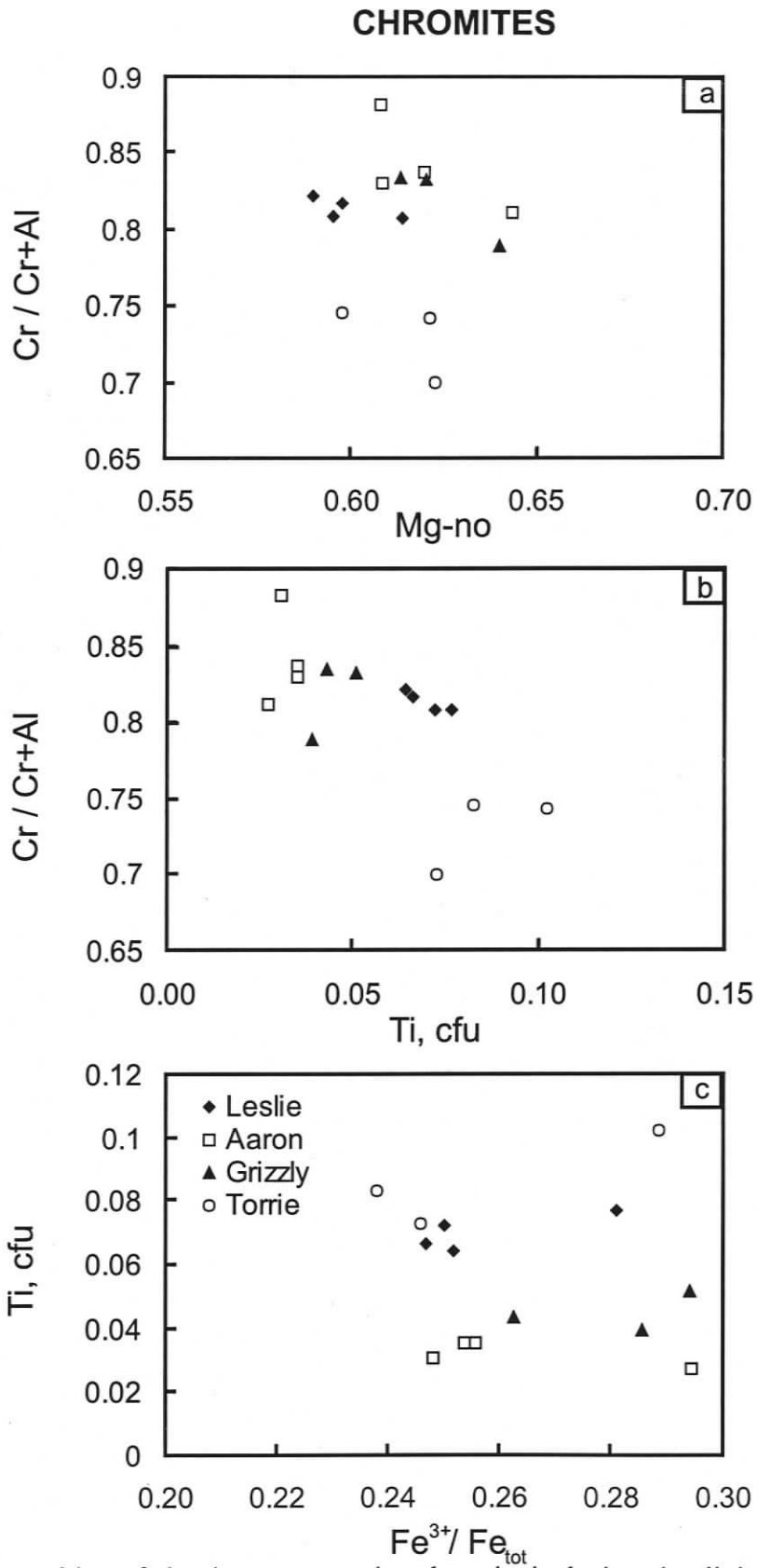

Figure 2.8 Composition of aluminous magnesian chromite inclusions in olivine phenocrysts from the Leslie, Aaron, Grizzly and Torrie kimberlites.

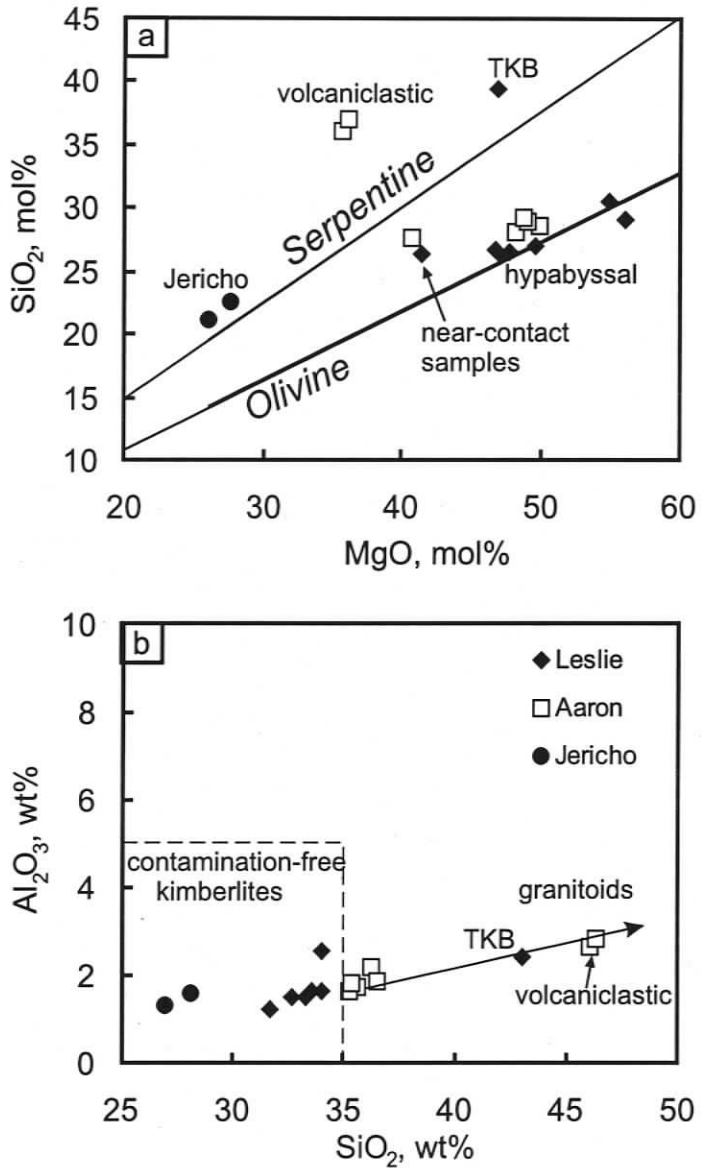

Figure 2.9 Whole rock compositions of the Leslie and Aaron samples from this study (LS-1-5 and AN-1-1) compared with other data for fresh kimberlite from the Leslie (Berg and Carlson, 1998) and Jericho kimberlite pipes (JD69, JD82) (Price et al., 2000). (a) SiO_2 vs MgO diagram showing Ol- and Serpentine-control lines shown. The line of constant olivine composition is Fo_{92}, and the composition of secondary serpentine is from Mitchell (1986). (b) Al_2O_3 vs SiO_2 diagram showing the field of contamination-free kimberlites from Mitchell (1986). The arrow shows the shift in kimberlite composition caused by contamination with granitoid country rock.

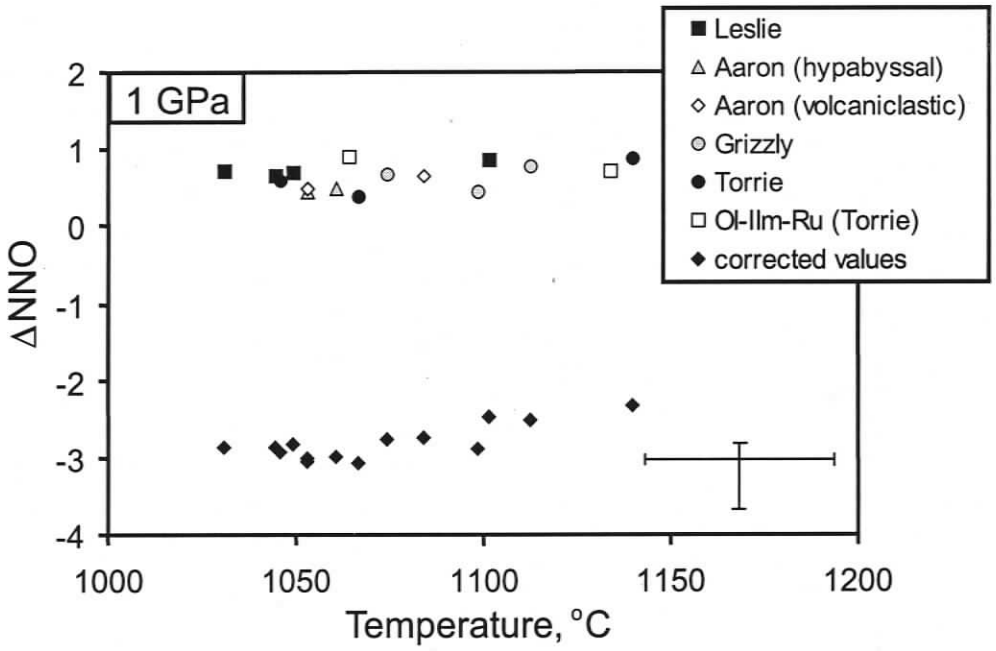

Figure 2.10 Oxygen fugacity and crystallization temperatures for olivine spinel assemblages in four kimberlite pipes and olivine ilmenite and ilmenite rutile assemblages for the Torrie pipe. fO_2 is shown in ΔNNO units (= log fO_2 sample - fO_2 NNO buffer at P and T). Black diamonds represent the maximum fO_2 values of all kimberlites corrected to a silica activity at the diopside-monticellite buffer. The uncertainty on each point are shown in the upper right.

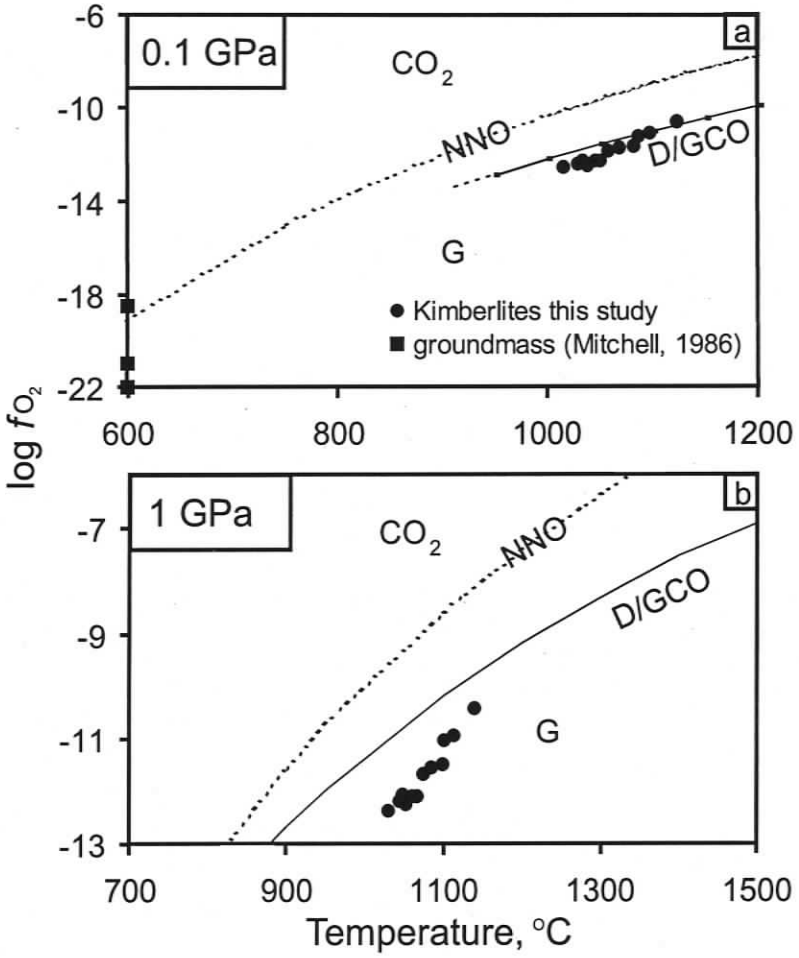

Figure 2.11 Stability fields of graphite (G) and CO_2 in log fO_2 T space calculated at (a)0.1 GPa and (b) 1 GPa compared to T fO_2 data from the Lac de Gras kimberlites recalculated at these pressures and corrected for silica activity. Positions of the NNO (Ballhaus et al., 1991) and G/DCO buffers (Frost and Wood, 1997) shown for comparison. The plot shows T - fO_2 estimates for kimberlite groundmass calculated for olivine - magnetite assemblages by Mitchell (1986).

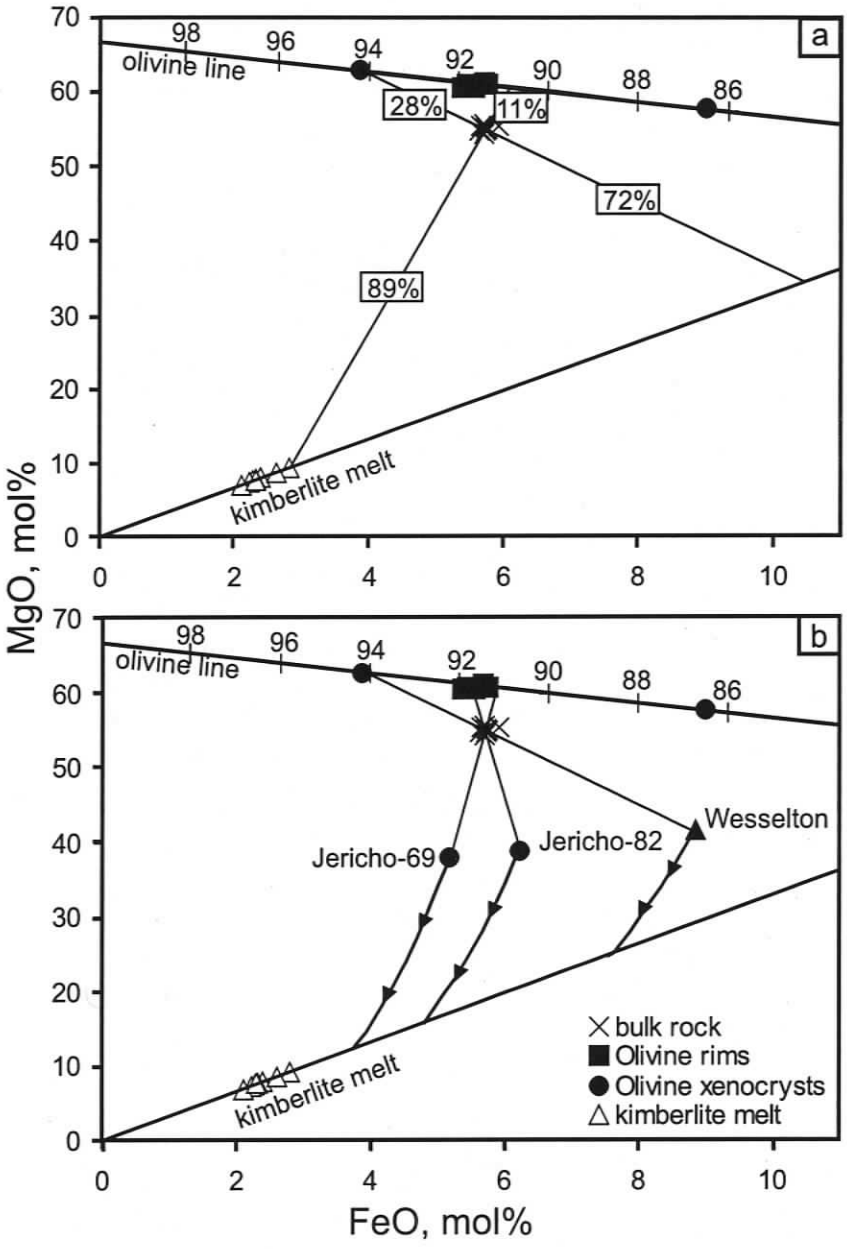

Figure 2.12 MgO and FeO mole proportions of bulk rock of unaltered Leslie and Aaron kimberlites, olivine phenocryst rims and equilibrated with them kimberlite melt. Olivine compositions plot along the "olivine line" with the Fo-components shown. a) Mass balance of bulk rock composition with the kimberlite melt and the correspondent olivine. The minimum and maximum values for the amount of olivine (both mantle and early phenocrysts) accumulated in the kimberlite melt are shown. b) Proportion of mantle olivine accumulated in the primary kimberlite melt that has MgO and FeO content equal to those of the Jericho-69, -82 and Wesselton aphanitic kimberlites, arrows show the paths of fractional crystallization of olivine for the latter three compositions.

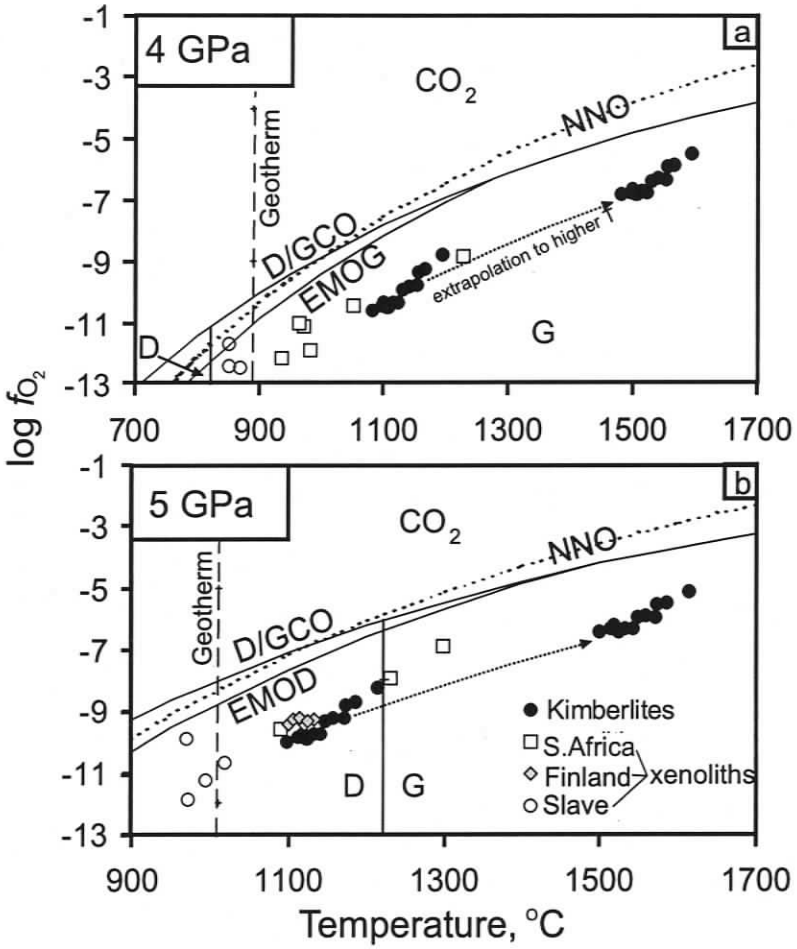

Figure 2.13 Stability fields of diamond (D), graphite (G) and CO_2 in log fO_2 T space calculated at (a) 4 GPa and (b) 5 GPa, compared to T fO_2 data from the Lac de Gras kimberlites recalculated and extrapolated to these pressures and to higher temperatures. For the extrapolation we made an assumption that kimberlite fO_2 relative to NNO buffer stays constant through the kimberlite crystallization from 5.0 GPa to 0.1 GPa. The fO_2 recorded by kimberlite-borne mantle xenoliths from southern Africa (McCammon et al., 2001), Eastern Finland (Woodland and Peltonen, 1999), and the Slave Province, Canada (Kopylova and McCammon, 2003) are similar to that of kimberlite magmas. Curves for the enstatite-magnesite-olivine-diamond/graphite (EMOD/G) buffer were calculated from Holland and Powell (1990), the D/G transition is from Kennedy & Kennedy (1976), and the position of the Lac de Gras geotherm is from MacKenzie & Canil (1999). The G/DCO and NNO buffers are as in Fig. 2.11.

CHAPTER 3

DISSOLUTION FORMS IN LAC DE GRAS DIAMONDS AND THEIR RELATIONSHIP TO THE TEMPERATURE AND REDOX STATE OF KIMBERLITE MAGMA

Yana Fedortchouk

Dante Canil

School of Earth and Ocean Sciences, University of Victoria, Victoria, B.C., Canada

Jon A. Carlson

BHP Billiton Diamonds Inc., Kelowna, B.C., Canada

3.1. ABSTRACT

The degree and character of diamond dissolution was compared to crystallization temperatures (T) and oxygen fugacities (fO_2) estimated from chromite inclusions in olivine phenocrysts in several kimberlites from Lac de Gras, Northwest Territories, Canada. The T and fO_2 values calculated at an assumed pressure of 1 GPa are in the range 970 – 1140 ± 50°C and 2.8 to 4.4 log fO_2 units below the nickel-nickel oxide (NNO) buffer. The T and fO_2 vary between kimberlites from northwest and southeastern clusters within 150°C and 1 log unit respectively. A detailed description of morphological forms and surface dissolution features for diamond parcels from the Panda, Beartooth, Grizzly, Misery and Jay kimberlites (>7000 stones) show that an increase in diamond resorption in the kimberlites corresponds to increase in T. The development of various surface

dissolution pits and structures correlates with higher fO_2 of kimberlites and therefore mainly happens in the magma. The two processes of diamond dissolution – volume resorption and surface etching, do not show a strong correlation with each other, since some of the resorption occurs in the mantle. We suggest that the fO_2 of the kimberlite magma plays an important role in the both processes. The proportion of plastically deformed brown diamonds does not correlate with the degree of volume resorption, but does correlate with the development of surface forms. The diamond grade is higher in kimberlites with lower fO_2 confirming that conditions of kimberlite crystallization can have notable effect on diamond dissolution.

3.2. INTRODUCTION

Natural diamonds recovered from kimberlites usually show a variety of morphological forms and surface features (Sunagawa, 1984), reflecting the complex history of diamond growth, dissolution and transformation during its residence in the mantle and ascent in kimberlite melts. Diamond dissolution (resorption) can be a complex multi-stage process (Gurney et al., 2004) resulting in a variety of dissolution forms. Etch pits, ruts, corrosion sculptures, frosting and other surface features are commonly accepted as the result of resorption and may lead to a very irregular form, and decrease in quality, of a diamond. For the formation of dodecahedra and tetrahexahedron (THH) diamond forms, two mechanisms, primary growth (Mendelssohn and Milledge, 1995, and references therein) and resorption of octahedron stones (Robinson et al., 1989) were proposed. The latter is a commonly accepted mechanism supported by recent experimental studies of diamond dissolution that showed significant volume loss (Kozai and Arima, 2003). Therefore,

diamond resorption processes greatly influence the grade and value of diamonds in a kimberlite pipe.

High-temperature kimberlite magma is a reactive media for diamonds. Experimental studies on diamond dissolution in alkaline melts (Khokhryakov and Palyanov, 1990; Kozai and Arima, 2003; Sonin et al., 2002) have produced many of the resorption features observed in natural diamonds. Their results support the suggestion (Robinson et al., 1989) that the reaction with kimberlite is the main mechanism of diamond destruction. Resorption in the mantle was also documented (Gurney et al., 2004 and references therein).

Experiments show that the mechanism for the diamond dissolution and resorption is oxidation by volatiles in kimberlite (CO_2 and H_2O) or components with variable valence states (e.g. Fe^{2+} - Fe^{3+}) where C is oxidized into CO_2 in the graphite stability field (Harris and Vance, 1974; Arima, 1998). Experiments on dissolution of diamond octahedrons in kimberlitic and lamproitic melts produced THH and dodecahedral forms where dissolution increased with temperature (T) and was suppressed by addition of CO_2 (Kozai and Arima, 2003). The oxidation of diamonds in a gas flow greatly increases at higher fO_2 (Evans and Phaal, 1961; Cull and Meyer, 1986; Sonin et al., 2000). Furthermore, T and fO_2 were found to influence the orientation of trigon etch pits commonly observed on natural diamonds (Yamaoka et al., 1980) and the presence or absence of other etching forms (Sonin et al., 2002). The presence of water enhances the dissolution rate of diamond and causes a change in morphological forms from the formation of trigonal layers on flat-faced octahedrons (Chepurov et al., 1985; Pal'yanov et al., 1995) at dry conditions to ditrigonal layers in the presence of water. Thus, experimental studies have established the strong influence of intensive variables of

kimberlite melt (T, fO_2, CO_2 and H_2O content) on the degree of diamond dissolution and the morphology of resorption forms.

At present, the characterization of mantle material entrained in kimberlites is the main tool for the prediction of grade and quality of diamonds in a pipe (Fipke et al., 1995). Since the properties of the host kimberlite influence the rate and character of diamond resorption they may also be reflected in the characteristics of a diamond population. To test this idea, we compare the T and fO_2 of kimberlite melt crystallization with the diamond content and the character of resorption in diamonds from several well-characterized kimberlite pipes in the Lac de Gras region (NWT, Canada). Exceptionally fresh kimberlites from the Lac de Gras region allowed us to apply olivine-spinel (Ol-Sp) thermometry and oxygen barometry (Ballhaus et al., 1991) to chromite inclusions in olivine phenocrysts in these kimberlites. Two clusters of kimberlites (North-West and South-East) in the Lac de Gras area differ in their degree of diamond resorption (Gurney et al., 2004). A detailed description of the morphology and surface features of individual stones was compiled for five kimberlite pipes from both clusters. One goal of the present study is to relate T – fO_2 data of kimberlite melts to different types of resorption and overall grade of the pipes in order to test to what extent these parameters can be used in assessing the diamond potential of a pipe. A second objective is to establish what type of resorption coincides in time with the later stages of olivine phenocryst crystallization.

3.3. GEOLOGICAL BACKGROUND

The Lac de Gras kimberlites were emplaced in Archean rocks of the east-central part of the Slave Province, Canada (Davis and Kjarsgaard, 1997; Pell, 1997; Creaser et al., 2004) and are subdivided according to their age and spatial distribution into North-West (~53

Ma), South-East (~56 Ma) and central clusters (~48 Ma) (Gurney et al., 2004). Thermobarometric data was obtained for eight kimberlite pipes that fall within all three clusters (Table 3.1, Fig.3.1). The diamond populations from five of these pipes: Panda, Misery, Beartooth, Grizzly and Jay, were described in terms of their morphology and presence of various resorption features. The Ranch Lake kimberlite may represent an extension of the NW group (Lockhart et al., 2004).

The composition and petrography of the nine kimberlites from this study is summarized in Table 3.1. Hypabyssal facies kimberlites contain fresh phenocrysts of olivine (0.2 – 1 mm) without any notable alteration. In volcaniclastic facies only margins of olivine are serpentinized. The matrix of hypabyssal kimberlite contains abundant monticellite (up to 80 μm) surrounded by a fine-grained aggregate of serpentine and calcite. Monticellite is absent in the matrix of volcaniclastic facies that consist of serpentine-calcite aggregate with numerous calcite grains (up to 100 μm) precipitated from a fluid phase.

3.4. METHODS

3.4.1. Sample Selection and Thermobarometry

The kimberlite samples we selected for the T – fO_2 calculations represent the main kimberlite body for the pipes having a complex structure (Fig.3.2). For the Panda and Misery pipes, however, kimberlite dykes were also studied. Both volcaniclastic and hypabyssal facies samples were collected for the Aaron pipe.

Olivine phenocrysts in both hypabyssal and volcaniclastic facies contain inclusions of euhedral (5 to 10 μm) aluminous magnesian chromites. The chromites occur

in the margins of olivine phenocrysts and therefore record the conditions in kimberlite magma at the end of the phenocryst crystallization. For olivine - spinel assemblages the reaction:

$$6\ Fe_2SiO_4 + O_2 = 3\ Fe_2Si_2O_6 + 2\ Fe_3O_4 \qquad (8)$$

olivine orthopyroxene chromite

was used as an oxygen barometer and $FeMg_{-1}$ exchange thermometer ($T_{Ol\text{-}Sp}$) (O'Neill and Wall, 1987; Ballhaus et al., 1991) . The uncertainty in $T - fO_2$ calculations from the $Fe^{3+}/\Sigma Fe$ of chromites determined from the microprobe data (Table 3.2 and 3.3) was evaluated using secondary standards (Wood and Virgo, 1989) (Fig. 3.3). The $\log fO_2$ values calculated from the Ol-Sp oxygen barometer are maxima and require a correction for the low silica activity of kimberlite melts (Fedortchouk and Canil, 2004). The maximum silica activity is limited by the presence of monticellite that crystallizes following the Ol-Sp assemblage, as observed petrographically and by experiment in kimberlite (Edgar et al., 1988). The silica activity in kimberlite must lie below the reaction:

$$CaMgSi_2O_6 = SiO_2 + CaMgSiO_4$$

The lower silica activity of kimberlite magmas, relative to the Ballhaus et al. (1991) calibration, results in lower calculated fO_2 values. A minima in calculated fO_2, however, and thus in silica activity, is limited by the lack of FeNi metal (i.e. the Ni precipitation curve – O'Neill and Wall, 1987) in kimberlite olivines we studied. The criteria for the selection of olivine and chromite grains suitable for these calculations, the applicability of Ol-Sp thermobarometry for this assemblage and further details of the calculation at variable Si activity in the melt are described at length elsewhere (Fedortchouk and Canil, 2004). The lack of knowledge of the exact silica activity affects the absolute accuracy of

our fO_2 estimates, but our study mainly concerns relative differences in fO_2 between pipes, and the precision in the measurements ensures such differences are real (Fig. 3.3).

3.4.2. Uncertainties of T – fO_2 calculations

Electron microprobe analyses of minerals were carried out with a CAMECA SX50 electron microprobe at the University of British Columbia (UBC). Major and minor elements were determined at 15.0 kV acceleration voltage and a beam current of 20.1 nA with a 5 μm beam for olivines and a 1 μm beam for chromites. Analytical conditions were 20 s counting time on peaks for all major elements, 60 s for Ni and 80 s for V. Data reduction was done with the "PAP" φ(ρZ) method (Pouchou and Pichoir, 1985) . Natural and synthetic standards were used for calibration. The Fe^{3+} and Fe^{2+} of the chromites were calculated on the basis of perfect stoichiometry (Droop, 1987).

The uncertainty in the $Fe^{3+}/\Sigma Fe$ of chromites calculated from the microprobe data was evaluated using secondary standards (Wood and Virgo, 1989) of two magnesiochromites (10-12a, 9-12) with Fe^{3+} determined by Mössbauer spectroscopy (McCammon and Kopylova, 2004) (Table 3.4). The presence of an inclusion in 10-12a grain produced the larger differences in T and fO_2 between the two methods because the Mössbauer spectra were obtained for the whole grain. We used only 9-12 chromite for evaluation of the accuracy, whereas precision was estimated based on reproducibility of analyses for both chromites in five different microprobe sessions.

The uncertainties in the calculation of the absolute values for T and ΔNNO were ±30° and ±0.8 log units, respectively (Fig. 3.3); that is, within the uncertainties of the thermometer and oxybarometer. The uncertainties in calculation of relative differences in T and ΔNNO

between our kimberlites are much smaller due to high precision of the EMP method (±20°, ±0.5 log unit (Fig. 3.3). To assure a high precision for analyses and calculations, the exact same procedure was followed during every microprobe session. Samples from one kimberlite were analyzed in different sessions and gave identical results.

3.4.3. Diamond descriptions

Diamond parcels from the Panda, Beartooth, Misery, Grizzly, and Jay kimberlites (>1,500 carats, >26,000 stones) were recovered from reverse circulation drill holes collared within each pipe. The parcels were sieved into nine classes using Tyler sieves (square mesh). The diamonds range from approximately 4 carats to less than 0.001 carat (sieve size of +3.5 to –25 mm or +9 mm to –710 μm respectively). For the sieve classes with less than 200 stones all diamonds were individually described. The larger populations were randomly split and approximately 25 - 50% of the stones (at least 100 from each group) were described. To ensure that this approach produces representative diamond populations we extended the description of a few sieve classes from Panda to a larger number of diamonds and found no influence on the results. In total over 7,000 stones (almost 1000 carats) were individually described.

The physical properties recorded in the diamonds include weight, colour, colour intensity, crystal morphology, presence of internal fractures and inclusions, surface growth and dissolution features. A more detailed description scheme exists (Gurney et al., 2004), but only the influence of resorption processes on crystal morphology and development of etch features are addressed in this study. To collect information from the larger number of stones we used an optical microscope for the observation of the diamond

surface features. Therefore, resorption events forming the smallest etch pits may not be reflected in our data.

The classification of crystal morphology was simplified into four major forms: octahedron and cube (primary forms), tetrahexahedroid (THH) (secondary form) and irregular broken stones. For the purpose of this study we did not distinguish between two products of octahedron resorption: dodecahedron and THH. We recorded the degree of resorption, however, as the percentage of the octahedral faces dissolved. We divided octahedrons into three groups according to percentage resorption of octahedral faces: 1) 0%, 2) <25%, 3) 25-50%. THH was classified as a stone with more than 50% resorption. The degree of resorption was recorded only for octahedron – THH crystal morphologies. The evolution of cube morphology with resorption is not well understood, but cubes are only a minor portion of the diamond populations from kimberlites we studied.

3.5. RESULTS

3.5.1. Resorption in Lac de Gras diamonds

Natural stones often show several growth zones where some dissolution may have occurred between different growth events and conditions (Taylor et al., 1995). Dissolution may change the morphology of the diamond to produce a variety of crystal forms with various combinations of octahedron and THH faces, and may develop etch pits, ruts, hillocks, striation, disks, frosting, and corrosion structures on the diamond surface (Robinson et al., 1989). The presence of etch pits depends on the conditions of the etching and the diamond morphology: trigons form on (111) and squares on (100) faces. They often show few generations from the earlier large pits to the later small ones (Fig. 3.4a).

For our purpose we combined all of the observed dissolution features into two major groups. The first, resorption, refers to the development of secondary THH faces on the octahedral crystals that may be accompanied with a substantial loss of volume. The degree of resorption is described as ratio of octahedron to THH (O/THH). The second, etching or surface features, describes all the diverse surface structures produced by the dissolution processes.

3.5.1.1. Resorption

The diamond populations of kimberlites from different clusters within the Lac de Gras area have the same diamond types in terms of their morphology and colour, but the proportion of these types differ significantly between the clusters (Gurney et al., 2004). The degree of resorption is very low in Panda and Beartooth diamonds (NW cluster) which are dominated by mainly colourless flat-faced octahedrons (Fig. 3.5a, Table 3.5, 3.6). In contrast, diamonds from Misery and Jay (SE cluster) are highly resorbed (Fig. 3.5b) with a very high proportion of THH and brown stones (Fig. 3.5a, Tables 3.5, 3.6). The Grizzly population is drastically different from the other NW kimberlites by having a very high proportion of brown stones and resorbed THH forms.

3.5.1.2. Main types of surface features on Lac de Gras diamonds

The terminology for the description of diamond surface features in this study is based on previous work (Robinson et al., 1989; Afanasiev et al., 2000).

Etch pits (trigons, hexagons, squares). Negatively oriented trigon pits (Fig. 3.4b) developed on (111) face of octahedrons are very common on the Lac de Gras diamonds. In rare cases they develop into hexagons. Square pits are less common than trigons and

appear on THH faces in the (100) direction (Fig. 3.4c). Positively oriented trigons are usually too small to be seen under the optical microscope and therefore were not recorded in the present study.

Ruts are slots and etch channels present in all types of diamonds (Fig. 3.4d). They form after fractures and, therefore, depend not only on the intensity of the dissolution processes, but also on the presence of cracks on the diamond surface. Nevertheless, the kimberlites with a higher proportion of rutted diamonds underwent more extensive dissolution.

Hillocks (Fig. 3.4e) are irregularities of pyramidal, drop-shaped or elongate shape and are common on THH faces.

Striations (Fig. 3.4f) are common features on THH and along the edges of resorbed octahedrons from all the pipes, but were recorded only in Grizzly and Jay stones, and include different types of lamination and stepped patterns. It is not always possible to distinguish between the growth and dissolution forms. Step-faces on the octahedrons we assigned to growth if they have sharp edges, whereas those with rounded corners and curved edges were considered as secondary forms.

Frosting (Fig. 3.4g) is believed to form in near-surface conditions (Afanasiev et al., 2000) and therefore is not a focus of our study. We recorded the presence of frosting, but did not distinguish between its coarse and fine types.

There is a proportion of octahedral and THH diamonds in all the pipes that do not show any traces of dissolution and have glossy surfaces (Fig. 3.4h).

The presence of different types of surface dissolution features in octahedron and THH stones from the five Lac de Gras pipes is given in Table 3.7 and on Fig. 3.6. The main forms are various etch pits and ruts that show similar distribution patterns between

the pipes, indicating that they may be formed by the same process. Etch pits and ruts are present on the larger proportion of stones from the Panda and Beartooth and notably less so in Misery and Jay. Frosting is a very common feature in octahedrons and THH from Grizzly and in THH from Misery and Jay. In general, surface etching is more common in Panda and Beartooth and less in Misery and Jay kimberlites.

3.5.2. T-fO_2 Calculations for Lac de Gras kimberlites

In the present study we expanded previous T and fO_2 calculations (Fedorthcouk and Canil, 2004) to a larger number of pipes where the diamond data is available. We can also compare the crystallization conditions of kimberlites from different clusters (Table 3.8, Fig. 3.7).

Oxygen fugacity and crystallization temperatures obtained for the eight Lac de Gras kimberlites form distinctive separate trends for each pipe (Fig. 3.7a). They show that during co-crystallization of Ol-Sp assemblage the melt became more reduced relative to the NNO buffer. The fO_2 evolution with T in the kimberlites is approximately parallel to Wustite – Magnetite (WM) buffer and therefore the differences in fO_2 between different kimberlite bodies is more obvious when viewed relative to the WM buffer to eliminate the T effect (Fig. 7b). A decrease in fO_2 during groundmass crystallization in kimberlites was also described at temperatures below 800°C (Mitchell, 1986).

As noted above, the silica activity of the kimberlites is somewhere below that of the Diopside Monticellite (Di-Mnt) buffer and the fO_2 values shown on Fig. 3.7 are therefore maximum values. The minimum fO_2 values are limited by the lack of any native metal to be slightly above the Ni precipitation curve just above the IW buffer (O'Neill and

Wall, 1987). Thus, log fO_2 of the kimberlites could be in the range –11.5 to –13 at 1100°C and an assumed pressure of 1GPa. The uncertainties of our fO_2 calculations are smaller than this range of fO_2 (Fig. 3.3 and methods). We do not know the pressure of Ol-Sp co-crystallization, but for the range of possible pressures under which monticellite is stable in these kimberlites (0.1 GPa to 1 GPa - Fedortchouk and Canil, 2004) the effect of P is 20°C/GPa on $T_{Ol\text{-}Sp}$, 0.14 log unit/GPa on silica activity, and 0.4 log units/GPa on fO_2.

The margins of olivine phenocrysts from all the kimberlites have uniform composition of Mg# (Mg/Mg+ Fe) 0.91-0.92 (Table 3.2). Olivines from the Torrie and Ranch Lake pipes have slightly lower and higher Mg#, respectively, than phenocrysts from the seven other pipes. The variations in calculated T and fO_2, however, are mainly determined by the variation in chromite composition. The inclusions in olivine phenocrysts are titanian aluminous magnesian chromites (according to Mitchell, 1986) with a positive correlation between Cr/Cr+Al (0.6 – 0.9) and Fe^{2+}/Fe^{2+}+Mg (0.3 – 0.5) corresponding to the macrocrystal trend of Mitchell (1986) but TiO_2 (1 – 4 wt%) of the Lac de Gras chromites are slightly higher (Table 3.3). Variations in the chromite composition between different kimberlites are most distinctive in terms of the Cr- and Ti-content (Fig. 3.8). In the Torrie kimberlite, Mg# is low in the both mineral phases and probably indicates the higher Fe-content of its melt. The high TiO_2 of the Torrie chromites and presence of other Ti-bearing phases (ilmenite and rutile) suggest that the Torrie kimberlite melt was probably enriched in Ti compared to the other magmas.

3.6. DISCUSSION

3.6.1. Variations in T and fO_2 of kimberlites

The precision of the T and fO_2 calculations (Fig. 3.3 and methods) permits an examination of the *relative* differences between the kimberlites. The T and fO_2 values of the Ekati kimberlites correlate with their division by age and location into clusters. The fO_2 decreases and crystallization T slightly increases from the NW cluster (Panda, Beartooth and Leslie kimberlites) to the Central zone (Aaron) and further to the SE cluster (Misery) (Fig. 3.9). The Grizzly kimberlite has two T-fO_2 trends, one between the NW cluster and the Aaron pipe, and another closer to the Misery pipe (Fig. 3.7b). The Grizzly pipe is geographically part of the NW group (Fig. 3.1), but its age estimation has larger uncertainties and it may be as young as the Central zone pipes (Table 3.1). Both T-fO_2 trends in the Grizzly pipe have similar chromite compositions. The differences in fO_2 are due to the low Mg of the olivines crystallized at lower fO_2. These olivines also have higher CaO contents. This variation in T-fO_2 data within the Grizzly pipe may be due to some local effect within the kimberlite or perhaps the mixing of different magmas.

Variations between all the kimberlites are within 150°C and 1 log fO_2 unit. The fO_2 variation between the kimberlite melts may be due to the differences in the redox regime of their mantle source or produced during ascent and crystallization of the melts. In the first case, the increase in fO_2 of the mantle source would be lateral from SE to NW or fluctuate with time (Table 3.1, Fig. 3.9). In the second case, the original fO_2 of the melts could diverge due to differences in their degassing history, mixing with other

magmas or entrainment of different xenolithic material. Differences in the crystallization path are unlikely given the similarities in mineral assemblages of all the kimberlites.

3.6.2. Influence of magma crystallization conditions on diamond populations

Substantial differences in the appearance and quality of diamonds between the NW and SE kimberlite clusters in the Lac de Gras field were revealed by Gurney et al. (2004). A significant increase in resorption and in the proportion of brown stones from the NW group (Panda, Beartooth, Leslie) to the SE group (Misery, Jay) was observed. The Grizzly diamonds differ greatly from the other NW kimberlites by having a much higher proportion of brown stones and substantial resorption. Gurney et al. (2004) explored how local events in the mantle and variations in sampling of different mantle domains by kimberlite magmas could produce the observed differences in the diamond populations. In a complementary way, we focus instead on the surface features and morphology of diamonds to see how they may correlate with the properties of the host kimberlite melt.

A significant effect of T and fO_2 on the rate of diamond dissolution was demonstrated by experiment (Sonin et al., 2000; Kozai and Arima, 2003). Our data shows a general correlation between the characteristics of the diamond population and the T and fO_2 of the host kimberlite. Increases in the degree of resorption for diamonds from Panda and Beartooth to Misery and Jay (Fig. 3.5a,b) correlate with an increase in crystallization T (Fig. 3.7b). The more extensive development of surface etch features in Panda and Beartooth diamonds correlates with their higher oxidation state (Fig. 3.7b). The Grizzly diamonds are notably different from the other NW kimberlites and have much larger T and fO_2 variation than the other pipes from the NW cluster.

Interestingly, our data show a negative correlation between the grade of a pipe (carats /tonne) and the fO_2 of the melt (Fig. 3.10). The grade is a general parameter and depends on a great variety of factors that include how diamondiferous the mantle source is, the mantle processes that might influence diamond presence or appearance, the sampling of the mantle by kimberlite and the properties of the kimberlite melt. The correlation indicates that magma redox may be important for the character of diamonds recovered from a kimberlite and deserves closer investigation.

To test the influence of conditions in kimberlite melt on diamond preservation we also examined the Ranch Lake kimberlite, which contains a good suite of "diamond" indicator minerals, implying sampling of a diamondiferous source, but nevertheless has a low diamond grade (Cookenboo, 1996). The high oxidation state of this kimberlite (Fig. 3.7, Table 3.8) indicates that this parameter can play an important role in diamond preservation.

The resorption of octahedron to form THH may greatly influence the diamond volume and resultant grade of a pipe. Our data shows, however, that resorption increases with T, and that diamond grade decreases with increasing fO_2. Furthermore, the degree of resorption and grade do not necessarily correlate. For example, the Misery kimberlite has the highest grade, yet contains significantly more resorbed stones than Panda (Table 3.1 and 3.2).

The relative importance of events in the mantle or magmatic resorption is not known. As a result, the relationship between the degree of resorption and diamond grade may be very complex and partly reflect the history of the diamonds in both the mantle and the kimberlite. Conversely, there is also a possibility that the higher proportion of THH may indicate a lower degree of resorption. In a kimberlite, some diamonds included in

xenoliths during emplacement are never exposed to interaction with the melt and remain unresorbed. The stones that are released from a xenolith react with melt, and in reactive media will be completely destroyed, resulting in a high O/THH ratio but low grade. In a less reactive melt, the liberated diamonds are only partially dissolved and preserved as THH, resulting in low O/THH ratio but high grade. For stones released from xenoliths, more reactive kimberlites will have a higher proportion of THH amongst small diamonds, whereas less reactive kimberlites will have O/THH ratio approximately similar in all size categories. In Panda and Beartooth, the O/THH ratio decreases towards the small diamonds while in Misery it is approximately constant. Thus, there is a possibility that Panda and Beartooth diamonds underwent stronger dissolution than those at Misery, and in this case, the degree of resorption may be influenced by the oxidation state of the kimberlite magma.

The T dependence of diamond dissolution kinetics in kimberlite melts is well known from experiments. Kinetic data (Kozai and Arima, 2003) show that a change in T from 1000 to 1100°C results in 3-fold increase in resorption (in mm/hour). Diamond oxidation in gases at controlled fO_2 can provide a proxy for diamond dissolution in melts with variable fO_2 (Evans and Phaal, 1961;Cull and Meyer, 1986; Sonin et al., 2000). Experimental data by Sonin et al. (2000) shows that at fO_2 and T calculated for olivine – chromite kimberlite assemblages (carbon-carbon oxide fO_2 buffer and 1100°C) change in 1 log unit fO_2 results in more than eight times faster diamond oxidation. Thus, even small difference in fO_2 of kimberlite melt may produce a notable difference in diamond grade of the pipe. This is confirmed by more recent data on the influence of fO_2 on diamond dissolution kinetics in kimberlite melts (Kozai and Arima, 2005).

3.6.3. Types of resorption produced by kimberlites

Some diamonds show a complex superposition of various dissolution features produced at different times (Fig. 3.4a). Diamond oxidation in experiments at different conditions (burning in air, dissolution in melts at variable T and P) produce similar surface features some of which also develop during diamond growth (e.g. Afanasiev et al., 2000). Thus, it is usually not possible to distinguish resorption developed in the mantle from dissolution in a kimberlite melt; the appearance of a diamond may be a combination of both. A group of diamonds resided within the same domain would possibly share similar properties (degree of plastic deformation, impurities, nitrogen content and aggregation state) and undergo the same dissolution events. On the other hand, diamonds with identical properties, but that resided in the different parts of the mantle, may show similar behaviour when resorbed in kimberlite. Variations in the amount and distribution of defects within the diamond structure may result in different responses to resorption (Mendelssohn and Milledge, 1995). All these factors complicate our understanding of the influence of kimberlite crystallization conditions on the character of resorption in different diamond parcels. By examining any possible correlations between different types of resorption, and diamond properties and degree of resorption, we use the Lac de Gras diamond data to get a better understanding on what type of resorption could have occurred in the kimberlite, as opposed to in the mantle.

3.6.4. Relationships between dissolution forms

The proportions of stones with different types of surface dissolution features vary between the five Lac de Gras pipes (Fig. 3.6). The correlation between etching and rutting processes agrees with their simultaneous development in experiments. The relationship

between trigon and square pits is usually not obvious because the trigons and squares develop in (111) and (100) directions, respectively, in some cases forming simultaneously (Fig. 3.11a). On the contrary, frosting shows no connection with the development of etch pits (Fig. 3.6) consistent with its development at a later stage of kimberlite emplacement where different parameters, possibly local conditions during emplacement, may play an important role.

In experiments (Kozai and Arima, 2003) the resorption of octahedral faces is usually accompanied by the development of trigon and hexagon pits. Nevertheless, in the diamond parcels from this study some of the significantly resorbed stones have remnants of flat octahedron faces without any etch pits (Fig. 3.11b). Moreover, there is no correlation between the resorption and etching. We calculated the proportion of stones with etch pits in the (111) direction in variously resorbed diamond groups (Fig. 3.12). The highest proportion of etched stones was recorded in the least resorbed parcels (Panda and Beartooth). Furthermore, within each kimberlite etching generally decreases with increasing resorption. The exception is the unresorbed groups with the lowest etching. These diamonds probably never experienced mantle resorption and were protected, perhaps in xenoliths, whilst in kimberlite melt. The low etching recorded in THH's, on the other hand, may be due to little preservation of the octahedron face (111) where the trigon and hexagon pits are formed on a diamond.

The multi-stage character of etching and resorption can be seen on individual diamonds (Fig. 3.4a, Fig. 3.11c-f). Some of the trigon pits present on (111) faces are cut by ditrigonal layers formed during resorption in the (101) direction (Fig. 3.11c-e). The resorption therefore either postpones the etching or develops simultaneously. On the

contrary, other trigons (Fig. 3.11f) were formed on previously resorbed surfaces clearly postponing resorption.

The lack of a positive correlation between etching and the degree of resorption in all five kimberlites indicate that these two processes do not accompany each other in every dissolution event and that each may be affected by different parameters. The total proportion of stones with various surface features produced by etching may therefore be more informative of the degree of diamond dissolution in kimberlite melt than the proportion of resorbed stones, which tend to be the product of resorption in both the kimberlite and the mantle.

3.6.5. Correlation of diamond properties and resorption

Internal diamond properties such as hydrogen and nitrogen content, defect aggregation state and plastic deformation are thought to influence resorption (Mendelssohn and Milledge, 1995). Indeed, the most resorbed Lac de Gras diamond parcels (e.g. Misery and Jay) have the highest proportion of brown stones. Because brown colour is generally attributed to incipient graphitization produced during plastic deformation (Urusovskaya and Orlov, 1964; Robinson et al., 1989) the presence of these defects in the diamond structure may result in the susceptibility of brown stones to destruct through dissolution (V.P. Afanasiev, personal communication, 2004). The fracturing of diamonds will also accelerate resorption. We made an attempt to evaluate the effect of diamond colour and fractures on the presence and the extent of some dissolution forms for the five Lac de Gras diamond parcels.

The degree of resorption (O/THH), and the presence of etch pits, ruts and frosting were examined as a function of colour (colorless to brown stone ratio, W/Br) and of the

amount of internal fractures and cracks (Fig. 3.13). The Panda and Beartooth kimberlites have high O/THH and W/Br, but for the three pipes with low O/THH and W/Br ratios, there is no positive correlation between these two parameters. This suggests that differences in colour cannot explain the observed diversity of diamond dissolution characteristics in the five parcels. The presence of trigon etch pits on the other hand, gradually increases in diamond groups having more brown stones (Fig. 3.13). This correlation is even stronger for the development of frosting. Neither forms of dissolution correlate with the amount of diamond fractures.

3.7. CONCLUSIONS

We show the fO_2 of kimberlite magmas determined from Ol-Sp oxygen barometry to be 2.8 to 4.4 log units below the NNO buffer. The T – fO_2 values for individual kimberlite pipes in the Lac de Gras area form trends showing more reducing conditions with decreasing T. There are significant variations in T – fO_2 values between the NW and SE clusters of kimberlites that are larger than uncertainties in the oxybarometry and correlate with substantial differences in the diamond populations (Gurney et al., 2004). The fO_2 decreases and crystallization T increases from the NW to SE cluster, whereas within the NW cluster Panda and Beartooth kimberlites have similar diamond populations and T-fO_2 values.

Various dissolution features in diamonds from the five Lac de Gras pipes correlate with T-fO_2 values for their kimberlite melts. The Misery kimberlite has the highest proportion of resorbed diamond forms (THH) and the highest crystallization T. The diamonds from more oxidized kimberlites (Panda and Beartooth) have more extensive development of surface dissolution features. There is no correlation between surface

etching and volume resorption in our kimberlites. Development of etch features is more extensive in diamond groups with a higher proportion on brown (possibly plastically deformed) stones, whereas the degree of resorption does not follow this correlation. We suggest that the development of the surface etching mainly occurs in kimberlite melt and therefore is controlled by fO_2. Resorption, on the contrary, depends on the conditions in both the kimberlite and in the mantle source and its relationship with conditions in the magma are obscure.

The diamond grade of a kimberlite correlates negatively with its fO_2. Whether the range of observed fO_2 values represents variations in the oxidation/reduction processes in the kimberlite magmas, or were inherited from their mantle source is uncertain. The high fO_2 values determined for the Ranch Lake kimberlite, which has good suite of 'diamond indicator minerals' but low diamond grade, indicates that fO_2 of the magma plays a role in diamond preservation. The established correlations between T-fO_2 values of kimberlites and diamond resorption features suggest that conditions of the host kimberlite may notably influence the entrained diamonds. This opens up the possibility that given more data, oxybarometry obtained for kimberlite melts can be potentially used for diamond grade predictions.

ACKNOWLEDGEMENTS

The diamond descriptions were completed by YF at BHP Billiton Diamonds Inc. whom we thank for generous access to drill core and diamonds, and for suggestions and permission to publish. We also thank T. Nowicki at Mineral Services Canada Inc, and M. Kopylova for providing some of the kimberlite samples, M. Kopylova and C. McCammon for the chromite 'Fe^{3+} standards', and M. Raudsepp for assistance with EMP analyses. We are grateful to J. Gurney for sharing his experience in diamond description,

and M. Arima, C. Ballhaus and O. Navon for reviews. This research was supported by a Natural Sciences and Engineering Research Council of Canada Postgraduate Scholarship to YF and Discovery Grant to DC.

Table 3.1 Geology, age, petrography and diamond grades for the Lac de Gras kimberlites used in the present study. The matrix phases are: Serp – serpentine, Mnt – monticellite, Cc – calcite, Dol – dolomite, Phl – phlogopite, Pv – perovskite, Chr – chromite, Ti-Mt – titano-magmetite, Pyr - pyrite (P – present, M – minor, "-" – absent).

Locality	Age (Ma)	Kimberlite Geology	Matrix Composition	Matrix Minerals								Grade
				Carb	Ap	Mnt	Phl	Pv	Chr	Ti-Mt	Pyr	ct/tonne[f]
NW Group												
Panda	53±1[a]	resedimented volcaniclastic kimberlite with minor primary volcaniclastic kimberlite[e]	Serp-Dol aggregate	P	P	-	-	P	P	P	-	0.95
Beartooth	53.1±1[b]	---	---					---				1.2
Leslie	52.7±2.9[b]	mainly hypabyssal with a remnant of tuffistic kimberlite breccia (TKB)	Mnt grains in Serp matrix with Cc, Ap	P	P	P	P	?	P	P	-	0.33
Grizzly	50.8 ±4.8[b]	macrocrystic, heterolithic hypabyssal kimberlite	Mnt grains in Serp matrix	P	P	P	P	P	P	P	-	0.5
SE Group												
Misery	---	volcaniclastic kimberlite with associated dykes of macrocrystic hypabyssal kimberlite [e]	Serp-Cc aggregate with Ap & Phl	P	P	-	P	P	P	P	-	4.19
Jay	---	---	---				---					2.01
Central area												
Aaron	45.2±1.3[b]											
- hypabyssal		hypabyssal kimberlite	Mnt grains in Serp matrix with Cc	P	P	P	P	P	P	P	-	
- volcaniclastic		pelletal volcaniclastic	Cc grains in Serp matrix	P	-	-	P	P	P	-	P	
Others												
Torrie	late Cretaceous-early Paleocene[c]	macrocrystic, heterolithic, volcaniclastic kimberlite tuff and tuff breccia	Cc grains in Serp matrix	P	M	-	M	-	P	P	P	
Ranch Lake	52.1±0.3[d]	---	Cc grains in Serp matrix	P	-	?	P	-	P	-	P	0.2

[a] - based on Rb-Sr systematics on phlogopite macrocrysts (Gurney et al., 2004)
[b] - based on Rb-Sr systematics on phlogopite macrocrysts (Creaser et al., 2004)
[c] - from palynology (Nassichuk & McIntyre, 1995)
[d] - Lockhart et al., 2004
[e] - from field guide to the Ekati Diamond Mine (materials for the 8 International Kimberlite conference)
[f] - diamond grades for Ekati pipes are from Natural Resources of Canada web-page and Cookenboo (1996).

Table 3.2 Analyses of rims of kimberlite olivine from the Leslie, Aaron, Grizzly, Torrie, Panda, Beartooth, Misery and Ranch Lake pipes used in Ol-Sp thermometery and barometery calculations.

Sample	MgO	Al2O3	SiO2	CaO	TiO2	Cr2O3	MnO	FeO	NiO	Total	Mg-no
Panda kimberlite											
PC132-2	50.4	0.01	41.2	0.10	0.010	0.08	0.14	7.97	0.17	100.1	91.85
PC132-16	50.4	0.00	41.1	0.08	0.024	0.17	0.14	8.16	0.10	100.2	91.68
PC132-19	50.6	0.01	40.9	0.09	0.035	0.11	0.09	7.91	0.22	99.9	91.93
PC132-24	50.3	0.02	41.0	0.12	0.007	0.08	0.14	8.58	0.13	100.4	91.27
PC132-26	50.4	0.03	41.0	0.10	0.013	0.07	0.19	8.63	0.16	100.6	91.24
PC132-31	50.2	0.02	41.1	0.07	0.047	0.06	0.10	7.90	0.36	99.88	91.89
PC132-32	50.6	0.01	40.9	0.08	0.000	0.03	0.13	8.31	0.12	100.1	91.56
PC132-1	50.2	0.01	40.5	0.06	0.025	0.41	0.11	8.05	0.17	99.58	91.74
Panda dyke											
puc31A-4	50.1	0.03	40.4	0.05	0.040	0.23	0.14	8.22	0.35	99.6	91.57
puc31A-5	50.8	0.00	41.4	0.04	0.039	0.07	0.13	8.09	0.21	100.8	91.8
puc31A-6	52.0	0.01	41.7	0.15	0.062	0.04	0.21	6.57	0.12	100.8	93.38
puc31A-7	50.6	0.00	41.4	0.04	0.049	0.11	0.12	7.95	0.22	100.5	91.91
Beartooth kimberlite											
BDC11-264-4	49.7	0.01	40.3	0.06	0.064	0.07	0.17	8.17	0.13	98.67	91.56
BDC01-179.8-1	50.7	0.04	40.9	0.05	0.000	0.09	0.14	7.93	0.34	100.2	91.93
BDC-01-159.8-2	51.0	0.02	41.0	0.03	0.010	0.06	0.12	8.04	0.37	100.6	91.87
BDC-01-158.1-2	50.5	0.02	40.8	0.04	0.037	0.06	0.10	8.02	0.39	99.99	91.82
Misery kimberlite											
316-3-1	50.6	0.01	40.9	0.06	0.026	0.06	0.11	8.35	0.40	100.5	91.53
316-3-2	50.4	0.00	41.0	0.06	0.000	0.09	0.14	7.99	0.39	100.1	91.84
93-12-279-1	50.5	0.02	41.0	0.05	0.000	0.08	0.12	8.02	0.42	100.2	91.82
93-12-279-2	50.4	0.01	40.8	0.07	0.000	0.07	0.16	8.12	0.40	100.1	91.71
93-12-279-3	50.5	0.02	40.7	0.06	0.038	0.12	0.11	7.97	0.43	99.97	91.87
93-12-279-4	50.5	0.00	41.0	0.05	0.012	0.04	0.13	8.20	0.39	100.3	91.65
93-12-279-5	50.6	0.03	40.8	0.05	0.000	0.04	0.10	8.17	0.44	100.3	91.7
93-12-279-6	50.5	0.01	40.9	0.04	0.002	0.12	0.18	7.64	0.43	99.83	92.18
93-12-279-7	50.3	0.03	41.1	0.10	0.000	0.05	0.19	7.99	0.15	99.9	91.82
93-12-279-3	50.1	0.03	40.6	0.04	0.033	0.10	0.14	7.85	0.43	99.41	91.93
93-12-279-8	49.8	0.02	40.5	0.05	0.013	0.06	0.10	7.78	0.40	98.69	91.93
Leslie kimberlite											
LS2-h-3	49.8	0.00	41.1	0.05	0.009	0.12	0.08	8.18	0.33	99.68	91.55
LS2-m-1	50.0	0.02	41.5	0.08	0.004	0.08	0.13	8.10	0.13	100.1	91.67
LS2-m-2	50.0	0.02	41.5	0.08	0.004	0.08	0.13	8.10	0.13	100.1	91.67
Ls2-n	50.9	0.02	40.5	0.05	0.044	0.02	0.10	8.44	0.36	100.4	91.48
Aaron kimberlite											
AN2-8	50.6	0.01	39.6	0.61	0.014	0.14	0.14	8.08	0.34	99.52	91.78
AN2-16	50.2	0.00	41.1	0.04	0.000	0.04	0.09	8.07	0.43	99.97	91.72
AN5-b-1	50.5	0.00	41.2	0.05	0.000	0.06	0.13	8.07	0.33	100.3	91.77
AN5-c-2	50.1	0.01	41.6	0.06	0.020	0.09	0.12	7.92	0.22	100.1	91.85
An1-l	50.2	0.01	40.9	0.05	0.014	0.09	0.07	8.10	0.38	99.88	91.71
An1-k	50.2	0.00	40.6	0.05	0.004	0.07	0.05	8.45	0.39	99.82	91.37
Grizzly kimberlite											
GR95-47-1	50.6	0.01	41.0	0.04	0.028	0.06	0.09	7.84	0.37	100	92
GR95-47-5	50.7	0.01	40.7	0.07	0.033	0.07	0.15	7.97	0.10	99.8	91.89
GR95-47-13	50.5	0.01	40.8	0.05	0.032	0.12	0.11	7.72	0.43	99.76	92.09
GR95-47-13	50.5	0.01	40.8	0.05	0.032	0.12	0.11	7.72	0.43	99.76	92.09
GR95-47-14	50.0	0.01	40.7	0.08	0.052	0.16	0.17	8.25	0.22	99.69	91.54
GR95-47-24	50.5	0.00	41.0	0.03	0.019	0.04	0.02	8.02	0.45	100.1	91.83
GR95-47-25	50.6	0.00	40.9	0.04	0.031	0.11	0.11	7.96	0.40	100.1	91.89
GR95-47-25	50.6	0.00	40.9	0.04	0.031	0.11	0.11	7.96	0.40	100.1	91.89
GR95-47-26	50.2	0.01	40.7	0.13	0.012	0.10	0.16	8.44	0.11	99.88	91.38
GR95-47-27	50.5	0.00	41.0	0.07	0.007	0.12	0.16	8.04	0.22	100.1	91.8
GR95-43-k2	51.0	0.02	41.1	0.03	0.000	0.06	0.09	8.17	0.42	100.9	91.76
GR95-43-e	50.5	0.01	41.1	0.06	0.017	0.17	0.11	8.57	0.23	100.8	91.31
GR95-43-a1	50.1	0.02	41.0	0.18	0.053	0.06	0.22	8.77	0.10	100.4	91.05
Torrie kimberlite											
TQ94-17-13-10	50.0	0.02	40.9	0.04	0.030	0.09	0.15	8.88	0.24	100.3	90.95
TQ-18E-2	49.7	0.01	40.5	0.07	0.044	0.09	0.12	8.62	0.15	99.33	91.14
TQ13-h-1	49.4	0.00	41.3	0.05	0.038	0.09	0.09	8.90	0.23	100.1	90.82
TQ17-f-1	49.3	0.00	40.8	0.10	0.049	0.07	0.12	8.73	0.34	99.52	90.97
Ranch Lake kimberlite											
RL1-3	51.3	0.00	40.5	0.03	0.023	0.04	0.10	7.85	0.45	100.2	92.09
RL3-2	51.6	0.01	41.0	0.17	0.023	0.01	0.09	7.34	0.38	100.6	92.61
RL3-5	50.1	0.00	41.0	0.04	0.042	0.01	0.14	8.80	0.32	100.5	91.03
RL3-6	51.4	0.02	41.0	0.05	0.041	0.07	0.12	7.65	0.31	100.6	92.29
RL3-12	50.9	0.01	41.0	0.14	0.004	0.00	0.14	7.61	0.26	100.1	92.26
RL2-1	50.6	0.02	41.4	0.03	0.026	0.00	0.07	7.60	0.24	99.95	92.23

Table 3.3 Analyses of chromite inclusions in olivine phenocrysts from the Leslie, Aaron, Grizzly, Torrie, Panda, Beartooth, Misery and Ranch Lake kimberlites.

Sample	MgO	Al2O3	SiO2	CaO	TiO2	V2O3	Cr2O3	MnO	FeO	Fe2O3*	NiO	Total
Panda kimberlite												
PC132-2	13.25	8.81	0.11	0.22	2.15	0.000	53.9	0.40	14.05	5.98	0.15	99.01
PC132-16	13.47	9.76	0.10	0.07	2.40	0.000	52.1	0.10	14.60	5.86	0.12	98.58
PC132-19	13.55	10.32	0.12	0.07	2.55	0.000	51.8	0.07	14.57	5.38	0.19	98.63
PC132-24	13.51	10.58	0.10	0.11	2.37	0.000	52.2	0.24	14.54	5.47	0.24	99.39
PC132-26	13.28	9.63	0.15	0.10	2.22	0.000	52.0	0.22	14.44	6.47	0.15	98.65
PC132-31	13.68	10.79	0.12	0.09	2.18	0.057	51.5	0.14	13.85	5.94	0.15	98.52
PC132-32	13.88	12.53	0.11	0.10	1.79	0.047	51.2	0.17	13.57	5.37	0.15	98.96
PC132-1	13.01	9.85	0.17	0.05	2.77	0.027	51.8	0.16	15.47	5.17	0.17	98.69
Panda dyke												
puc31A-4	12.26	6.94	0.15	0.02	1.86	0.075	56.7	0.06	15.51	5.55	0.17	99.34
puc31A-5	12.61	6.30	0.12	0.11	2.84	0.000	55.3	0.11	15.71	5.82	0.17	99.06
puc31A-6	12.35	4.97	0.07	0.02	3.24	0.000	55.8	0.16	16.10	5.91	0.23	98.82
puc31A-7	13.17	8.76	0.17	0.00	3.11	0.006	52.1	0.09	15.60	5.68	0.19	98.90
Beartooth kimberlite												
BDC11-264-4	13.04	9.16	0.08	0.03	3.09	0.000	53.0	0.22	15.88	5.16	0.19	99.86
BDC01-179.8-1	13.35	10.80	0.14	0.03	1.41	0.128	53.5	0.17	13.76	5.76	0.13	99.22
BDC01-179.8-2	12.74	8.20	0.09	0.03	1.22	0.100	56.8	0.09	14.12	5.47	0.13	98.94
BDC-01-159.8-2	12.99	9.60	0.15	0.05	2.23	0.071	52.8	0.09	14.90	5.72	0.17	98.76
BDC-01-158.1-2	13.26	9.70	0.13	0.00	3.49	0.000	50.7	0.10	15.81	5.35	0.24	98.76
Misery kimberlite												
316-3-1	13.35	10.23	0.15	0.06	1.51	0.054	53.3	0.15	13.71	6.00	0.20	98.69
316-3-1rim	13.49	10.21	0.13	0.06	1.44	0.013	53.2	0.12	13.64	6.22	0.12	98.65
93-12-279-1	15.04	14.11	0.18	0.05	1.07	0.115	51.0	0.08	11.44	5.70	0.23	99.02
93-12-279-2	15.63	17.68	0.18	0.02	0.81	0.092	47.1	0.10	10.83	5.73	0.20	98.37
93-12-279-3	15.22	14.55	0.14	0.03	1.03	0.090	51.3	0.11	11.34	5.35	0.18	99.33
93-12-279-4	14.69	12.89	0.14	0.05	1.30	0.001	51.7	0.12	12.17	5.60	0.16	98.84
93-12-279-5	14.19	10.50	0.19	0.01	1.23	0.006	54.2	0.06	12.68	5.23	0.14	98.38
93-12-279-6	15.55	17.52	0.16	0.04	0.84	0.081	48.1	0.15	10.97	5.20	0.14	98.77
93-12-279-7	14.35	11.62	0.18	0.04	1.11	0.087	54.1	0.19	12.21	5.44	0.23	99.50
93-12-279-3	14.63	14.57	0.14	0.03	0.98	0.102	51.3	0.09	12.05	5.02	0.25	99.20
93-12-279-8	14.14	10.96	0.15	0.00	1.38	0.063	54.1	0.07	12.62	4.91	0.18	98.54
Leslie kimberlite												
LS2-k-2	12.86	8.37	0.17	0.10	2.90	0.000	52.5	0.15	15.57	5.78	0.17	98.55
LS2-m-1b	12.90	8.09	0.15	0.04	2.67	0.000	53.6	0.09	15.47	5.64	0.14	98.82
LS2-m-2	12.53	7.85	0.10	0.11	2.56	0.007	53.7	0.15	15.54	5.81	0.16	98.48
Ls2-n	13.35	8.29	0.14	0.03	3.08	0.000	51.8	0.10	14.98	6.48	0.22	98.52
Aaron kimberlite												
AN2-8	12.32	8.38	0.09	0.01	1.02	0.133	56.2	0.06	14.51	5.83	0.16	98.76
AN2-16	13.02	8.79	0.11	0.01	1.20	0.108	56.2	0.17	13.70	5.46	0.14	98.93
AN5-b-1	13.33	8.74	0.16	0.04	1.11	0.143	56.0	0.07	13.15	6.10	0.16	98.95
AN5-c-2	12.42	5.40	0.12	0.04	1.21	0.058	59.9	0.14	14.26	5.24	0.12	98.87
An1-l	12.94	7.48	0.13	0.06	1.42	0.099	57.1	0.17	13.88	5.67	0.10	99.03
An1-k	12.70	7.79	0.13	0.00	1.41	0.180	56.4	0.12	14.10	6.04	0.16	99.07
Grizzly kimberlite												
GR95-47-1	13.41	8.21	0.12	0.02	1.76	0.022	55.2	0.12	13.63	5.79	0.18	98.46
GR95-47-5	12.33	4.54	0.11	0.05	2.85	0.000	57.7	0.11	16.07	5.48	0.15	99.38
GR95-47-13	13.32	10.28	0.11	0.07	1.76	0.021	53.2	0.05	14.17	5.40	0.20	98.61
GR95-47-13	13.20	9.38	0.15	0.05	1.83	0.026	54.2	0.08	14.33	5.37	0.17	98.75
GR95-47-14	13.62	10.35	0.20	0.05	1.61	0.018	53.9	0.14	13.88	5.12	0.18	99.06
GR95-47-24	13.85	9.71	0.13	0.01	2.50	0.000	52.1	0.10	14.06	6.02	0.15	98.67
GR95-47-25	13.33	7.97	0.12	0.04	1.70	0.000	55.5	0.16	13.78	5.97	0.13	98.71
GR95-47-25	13.99	11.06	0.16	0.06	2.11	0.027	51.5	0.05	13.54	5.88	0.24	98.60
GR95-47-26	14.01	11.75	0.14	0.04	1.61	0.113	52.1	0.15	13.05	5.90	0.10	98.90
GR95-47-27	12.90	7.12	0.09	0.08	2.31	0.000	55.8	0.18	14.78	5.43	0.13	98.78
GR95-43-k2	13.68	9.73	0.19	0.01	1.61	0.106	54.0	0.11	13.50	6.36	0.18	99.50
GR95-43-e	13.18	7.49	0.13	0.06	2.07	0.048	55.3	0.22	14.33	6.72	0.16	99.66
GR95-43-a1	12.91	7.54	0.09	0.05	1.74	0.013	56.4	0.19	14.49	5.74	0.09	99.26
Torrie kimberlite												
TQ94-17-13-10	14.49	13.83	0.13	0.04	3.24	0.000	46.2	0.09	14.40	6.12	0.13	98.64
TQ-18E-2	13.59	11.07	0.14	0.08	3.39	0.000	48.2	0.09	15.43	6.62	0.16	98.81
TQ13-h-1	13.90	13.65	0.10	0.04	3.02	0.000	47.3	0.07	15.01	5.44	0.21	98.76
TQ17-f-1	13.97	10.91	0.12	0.21	4.18	0.000	46.8	0.17	15.17	6.83	0.19	98.55
Ranch Lake kimberlite												
RL1-3	13.52	6.99	0.16	0.03	2.78	0.000	53.7	0.10	14.50	6.81	0.20	98.80
RL3-2	13.56	8.00	0.19	0.26	2.37	0.003	53.6	0.19	13.96	6.44	0.22	98.81
RL3-5	13.64	10.22	0.18	0.24	2.21	0.020	51.4	0.08	13.71	6.10	0.19	97.98
RL3-6	13.27	7.47	0.17	0.14	2.28	0.028	54.2	0.14	14.28	6.72	0.10	98.84
RL3-12	13.25	8.36	0.07	1.07	2.47	0.007	52.6	0.12	13.49	7.27	0.14	98.85
RL2-1	12.64	4.95	0.13	0.08	2.69	0.000	56.7	0.30	15.05	5.87	0.10	98.53

Table 3.4 Analyses of chromite standards from the Jericho mantle xenoliths

Microprobe Run	Sample	MgO	Al2O3	SiO2	CaO	TiO2	V2O3	Cr2O3	MnO	FeO	NiO	Total	Fe^{3+}/Fe_{tot} stoichiometry*	Fe^{3+}/Fe_{tot} Mössbauer**
1 run	9-12-1	12.23	16.89	0.00	0.02	0.02	0.202	53.1	0.13	16.73	0.06	99.41	0.098	0.093
1 run	9-12-2	11.91	16.50	0.01	0.00	0.00	0.185	53.2	0.16	16.68	0.06	98.73	0.081	0.093
1 run	9-12-3	11.98	16.55	0.01	0.00	0.03	0.205	53.2	0.11	16.59	0.06	98.76	0.081	0.093
1 run	10-12a-1	10.73	11.78	0.02	0.02	0.05	0.332	53.8	0.15	21.89	0.10	98.88	0.265	0.184
1 run	10-12a-2	10.44	11.53	0.01	0.00	0.06	0.373	54.1	0.19	21.90	0.08	98.71	0.255	0.184
1 run	10-12a-3	10.63	11.73	0.00	0.02	0.13	0.267	54.3	0.13	21.81	0.06	99.09	0.240	0.184
2 run	9-12-1	12.24	16.63	0.01	0.00	0.03	0.184	53.6	0.07	16.77	0.02	99.55	0.090	0.093
2 run	9-12-2	11.97	16.55	0.00	0.00	0.00	0.208	53.5	0.14	16.79	0.04	99.15	0.087	0.093
2 run	9-12-3	12.21	16.84	0.01	0.00	0.02	0.199	54.2	0.11	16.84	0.05	100.52	0.078	0.093
2 run	10-12a-1	10.64	11.94	0.01	0.00	0.07	0.309	54.3	0.17	22.14	0.08	99.63	0.251	0.184
2 run	10-12a-2	10.83	11.88	0.02	0.00	0.07	0.332	54.5	0.07	22.32	0.07	100.12	0.261	0.184
2 run	10-12a-3	10.49	11.63	0.00	0.00	0.09	0.296	53.8	0.10	21.82	0.08	98.33	0.246	0.184
3 run	9-12-1	12.29	16.52	0.02	0.00	0.02	0.189	53.6	0.13	16.77	0.08	99.63	0.096	0.093
3 run	9-12-2	12.18	16.26	0.01	0.00	0.01	0.206	53.9	0.05	16.67	0.04	99.32	0.092	0.093
3 run	9-12-3	12.44	16.57	0.00	0.00	0.03	0.199	53.2	0.17	16.71	0.03	99.36	0.103	0.093
3 run	10-12a-1	10.60	11.39	0.01	0.01	0.11	0.313	53.6	0.09	22.32	0.08	98.56	0.269	0.184
3 run	10-12a-2	10.78	11.50	0.00	0.02	0.11	0.323	54.1	0.14	22.30	0.09	99.30	0.270	0.184
3 run	10-12a-3	10.64	11.42	0.01	0.02	0.08	0.322	54.0	0.08	22.35	0.10	99.05	0.268	0.184
4 run	9-12-1	12.13	16.28	0.04	0.00	0.01	0.220	53.8	0.13	16.69	0.01	99.31	0.091	0.093
4 run	9-12-2	12.26	16.65	0.01	0.02	0.01	0.186	53.9	0.16	17.13	0.02	100.32	0.109	0.093
4 run	9-12-3	12.35	16.74	0.00	0.00	0.01	0.190	53.7	0.13	16.94	0.13	100.17	0.112	0.093
4 run	10-12a-1	10.40	11.44	0.01	0.00	0.07	0.360	54.0	0.15	22.37	0.09	98.90	0.270	0.184
4 run	10-12a-2	10.53	11.59	0.00	0.00	0.08	0.297	53.7	0.17	22.63	0.07	99.07	0.268	0.184
4 run	10-12a-3	10.40	11.54	0.01	0.02	0.08	0.271	54.4	0.12	22.46	0.04	99.30	0.244	0.184
5 run	9-12-1	12.18	16.37	0.01	0.00	0.01	0.143	53.3	0.12	16.69	0.03	98.88	0.092	0.093
5 run	9-12-2	12.30	16.66	0.03	0.02	0.04	0.263	53.5	0.09	16.92	0.06	99.83	0.122	0.093
5 run	9-12-3	12.39	16.84	0.00	0.00	0.00	0.238	54.1	0.08	16.45	0.00	100.14	0.088	0.093
5 run	10-12a-1	10.71	11.56	0.03	0.02	0.08	0.360	54.1	0.10	22.00	0.08	99.09	0.272	0.184
5 run	10-12a-2	10.59	11.38	0.01	0.01	0.12	0.335	53.6	0.11	22.38	0.10	98.64	0.273	0.184
5 run	10-12a-3	10.52	11.53	0.00	0.00	0.11	0.282	54.3	0.13	22.09	0.10	99.07	0.247	0.184

*- Fe3+ calculated using method of Droop (1987)

** - Fe3+ calculated from Mössbauer spectroscopy (McCammon & Kopylova, 2004)

Table 3.5 Morphology of diamonds from the five Lac de Gras kimberlites.

	NW Group			*SE Group*	
Locality	Panda	Bear-tooth	Grizzly	Misery	Jay
octahedron	1693	1107	427	4595	960
THH	259	328	592	9364	1759
cube	176	596	104	851	18
irregular	918	635	139	2100	193
other forms*			17		7
Total stones	3047	2667	1279	16909	2936
O/THH	6.5	3.4	0.7	0.5	0.5

* - other forms (cubo-octahedrons, cubo-THH, laminar dodecaherons etc) were recorded only in the Grizzly and Jay diamond parcel

Table 3.6 Degree of resorption in octahedron diamonds from the five Lac de Gras kimberlites present as per cent of octahedron faces resorbed (0% - no resorption, and >50% - is THH).

	NW Group			*SE Group*	
Locality	Panda	Bear-tooth	Grizzly	Misery	Jay
0%	164	67	200	2017	415
<25%	971	757	227	1588	290
25-50%	422	261	98	895	245
>50%	245	320	590	9367	1766
Total	1803	1404	1116	13965	2758

Table 3.7 Presence of various surface features (resorption and growth) in octahedron and THH diamonds from the five Lac de Gras kimberlites.

	NW Group			***SE Group***	
Locality	Panda	Bear-tooth	Grizzly	Misery	Jay
octahedrons					
trigons	1178	742	197	920	318
hexagons	21	16	30	46	9
ruts	726	302	36	296	74
frosting	90	32	183	439	173
step faces	302	184	206	2145	476
no etching	322	315	167	3217	473
total	1702	1107	427	4573	984
THH					
trigons	60	105	82	571	86
squares	5	0	37	276	58
hillocks	0	4	28	2036	105
striation*	nd	nd	179	nd	606
ruts	99	76	82	2432	198
frosting	7	9	461	4552	1260
no etching	89	182	249	4750	874
total	206	328	587	9325	1775

* - striation was present in all the pipes, but was described only in the Grizzly and Jay

Table 3.8 Equilibrium temperatures and oxygen fugacities calculated for Leslie, Aaron, Grizzly, Torrie, Panda, Beartooth, Misery and Ranch Lake kimberlites by Ol-Sp thermobarometery at an assumed pressure of 1 GPa

Sample	Ol-Sp T, °C [a]	$\Delta \log fO_2$ FMQ [b]	log a $_{SiO2}$ [c]		Corrected [d]		
			Di-Mont	En-Fo	log fO_2	ΔNNO	ΔWM
Panda kimberlite							
PC132-2	1069	1.1	-1.68	-0.54	-11.7	-2.7	-0.9
PC132-16	1059	1.1	-1.70	-0.54	-11.9	-2.8	-0.9
PC132-19	1040	1.0	-1.73	-0.55	-12.3	-3.0	-1.0
PC132-24	1074	0.9	-1.68	-0.54	-11.9	-3.0	-1.2
PC132-26	1086	1.2	-1.65	-0.53	-11.4	-2.6	-0.9
PC132-31	1058	1.1	-1.70	-0.54	-11.9	-2.8	-0.9
PC132-32	1057	0.8	-1.70	-0.54	-12.2	-3.1	-1.2
PC132-1	1016	1.0	-1.78	-0.57	-12.8	-3.1	-1.0
Panda dyke							
puc31A-4	1021	1.0	-1.77	-0.57	-12.7	-3.0	-1.0
puc31A-5	1052	1.2	-1.71	-0.55	-11.9	-2.7	-0.8
puc31A-6	967	1.7	-1.87	-0.60	-13.0	-2.5	-0.2
puc31A-7	1037	1.2	-1.74	-0.56	-12.2	-2.8	-0.8
Beartooth kimberlite							
BDC11-264-4	1036	0.9	-1.74	-0.56	-12.5	-3.1	-1.1
BDC01-179.8-1	1026	1.0	-1.76	-0.56	-12.6	-3.0	-0.9
BDC01-179.8-2	1024	1.0	-1.76	-0.56	-12.7	-3.1	-1.0
BDC-01-159.8-2	1018	1.1	-1.77	-0.57	-12.6	-2.9	-0.9
BDC-01-158.1-2	1032	1.1	-1.75	-0.56	-12.4	-2.9	-0.9
Misery kimberlite							
316-3-1 dyke	1066	1.0	-1.69	-0.54	-11.9	-2.8	-1.0
316-3-1rim dyke	1053	1.2	-1.71	-0.55	-12.0	-2.8	-0.9
93-12-279-1	1138	0.8	-1.57	-0.50	-10.9	-2.8	-1.2
93-12-279-2	1138	0.8	-1.57	-0.50	-10.9	-2.8	-1.3
93-12-279-3	1137	0.7	-1.57	-0.50	-11.0	-2.9	-1.4
93-12-279-4	1125	0.8	-1.59	-0.51	-11.1	-2.8	-1.3
93-12-279-5	1112	0.8	-1.61	-0.51	-11.4	-3.0	-1.3
93-12-279-6	1089	0.8	-1.65	-0.53	-11.7	-3.0	-1.3
93-12-279-7	1112	0.8	-1.61	-0.51	-11.3	-2.9	-1.3
93-12-279-3	1069	0.7	-1.68	-0.54	-12.2	-3.2	-1.3
93-12-279-8	1091	0.7	-1.65	-0.53	-11.8	-3.1	-1.3
Leslie kimberlite							
LS2-k-2	1049	1.1	-1.72	-0.55	-12.1	-2.8	-0.9
LS2-m-1b	1044	1.1	-1.73	-0.55	-12.2	-2.9	-0.9
LS2-m-2	1031	1.1	-1.75	-0.56	-12.4	-2.9	-0.8
Ls2-n	1101	1.3	-1.63	-0.52	-11.0	-2.5	-0.8
Aaron kimberlite							
AN2-8	999	1.1	-1.81	-0.58	-13.0	-3.1	-0.9
AN2-16	1052	0.9	-1.71	-0.55	-12.2	-3.0	-1.1
AN5-b-1	1084	1.1	-1.66	-0.53	-11.5	-2.7	-1.0
AN5-c-2	1053	0.9	-1.71	-0.55	-12.2	-3.0	-1.1
An1-l	1071	1.0	-1.68	-0.54	-11.8	-2.9	-1.1
An1-k	1073	1.0	-1.68	-0.54	-11.8	-2.8	-1.0

Table 3.8 (continued)

Grizzly kimberlite							
GR95-47-1	1078	1.1	-1.67	-0.53	-11.6	-2.7	-0.9
GR95-47-5	1052	1.1	-1.71	-0.55	-12.0	-2.8	-0.9
GR95-47-13	1015	1.0	-1.78	-0.57	-12.8	-3.0	-1.0
GR95-47-13	1021	1.0	-1.77	-0.57	-12.7	-3.0	-1.0
GR95-47-14	1065	0.8	-1.69	-0.54	-12.2	-3.1	-1.3
GR95-47-24	1088	1.2	-1.65	-0.53	-11.4	-2.6	-0.9
GR95-47-25	1080	1.1	-1.66	-0.53	-11.5	-2.7	-0.9
GR95-47-25	1075	1.1	-1.67	-0.53	-11.7	-2.8	-0.9
GR95-47-26	1106	0.9	-1.62	-0.52	-11.3	-2.8	-1.1
GR95-47-27	1063	1.0	-1.69	-0.54	-11.9	-2.9	-1.0
GR95-43-k2	1085	1.2	-1.66	-0.53	-11.4	-2.7	-0.9
GR95-43-e	1115	1.2	-1.61	-0.51	-10.9	-2.5	-0.9
GR95-43-a1	1099	0.9	-1.63	-0.52	-11.5	-2.9	-1.2
Torrie kimberlite							
TQ94-17-13-10	1111	1.0	-1.61	-0.51	-11.1	-2.7	-1.0
TQ-18E-2	1080	1.3	-1.66	-0.53	-11.4	-2.6	-0.8
TQ13-h-1	1067	0.8	-1.69	-0.54	-12.1	-3.1	-1.2
TQ17-f-1	1140	1.3	-1.57	-0.50	-10.4	-2.3	-0.8
Ranch Lake kimberlite							
RL1-3	1098	1.5	-1.63	-0.52	-10.9	-2.3	-0.6
RL3-2	1053	1.5	-1.71	-0.55	-11.6	-2.4	-0.5
RL3-5	1130	1.0	-1.58	-0.50	-10.9	-2.7	-1.1
RL3-6	1061	1.5	-1.70	-0.54	-11.5	-2.4	-0.5
RL3-12	1085	1.6	-1.66	-0.53	-11.0	-2.2	-0.4
RL2-1	1078	1.3	-1.67	-0.53	-11.4	-2.6	-0.4

a - Temperatures calculated from FeMg_1 Ol-Sp thermometer Ballhaus et al (1991) and O'Neill and Wall (1987)

b - Oxygen fugacities at 1 GPa calculated relative to FMQ buffer with oxygen barometer by Ballhaus et al.(1991)

c - Silica activity of Diopside-Monticellite (Di-Mont) and Enstatite-Forsterite (En-Fo) buffers calculated using thermodynamic data of Holland and Powell (1998)

d - Corrected maximum values of oxygen fugacities in kimberlites calculated for silica activity of Diopside - Monticellite buffer. Equation for NNO buffer is from Ballhaus et al. (1991 and references therein) and for WM buffer is from Frost (1991).

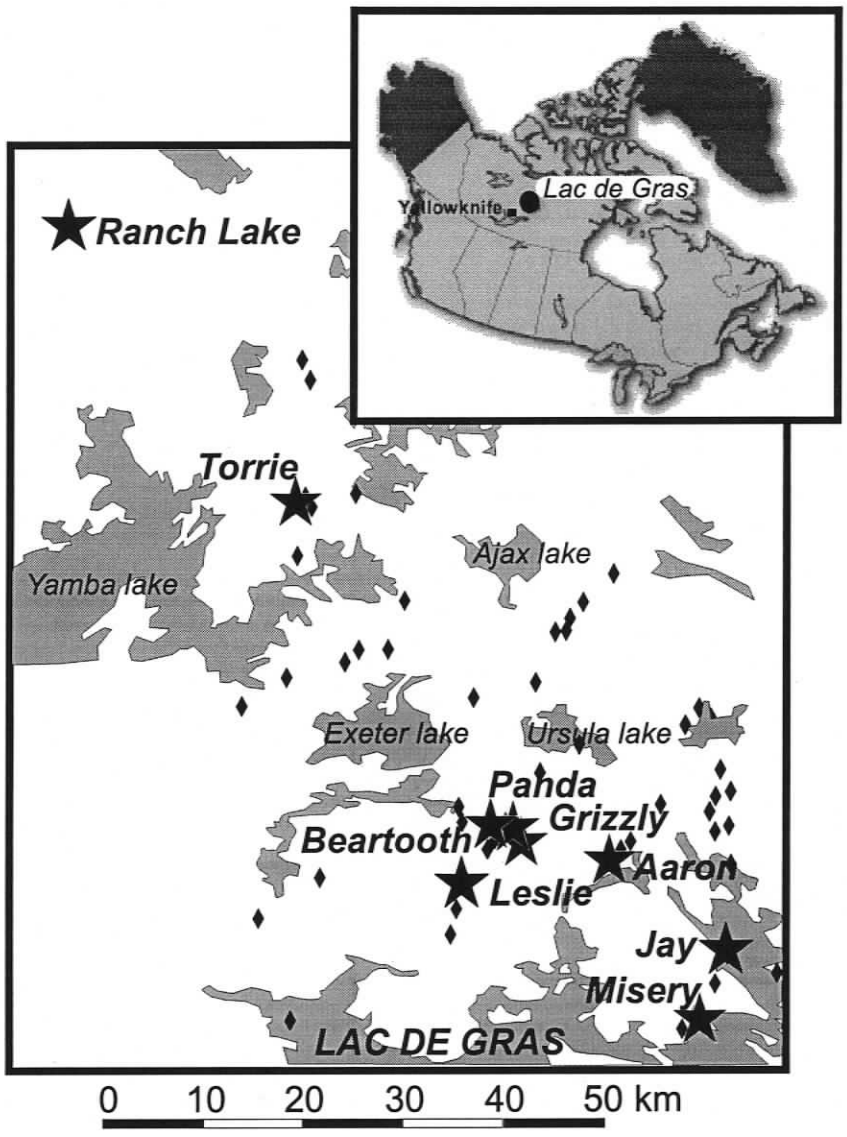

Figure 3.1 Location of kimberlite pipes (black diamonds) in the Lac de Gras kimberlite field, N.W.T., Canada. The kimberlites used in the present study are shown with black stars.

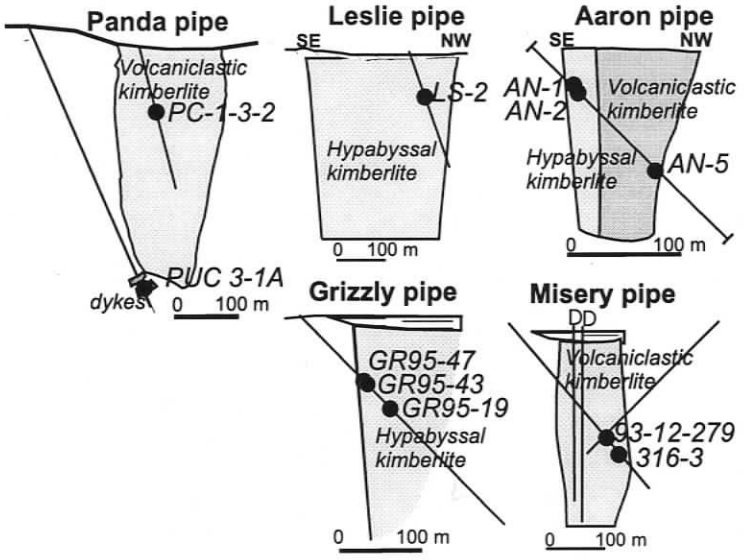

Figure 3.2 Cross-sections of the Panda, Leslie, Aaron, Grizzly and Misery kimberlite pipes with the location of samples used in this study shown. In the Misery pipe the diamonds described in this study were recovered from two drill holes "D".

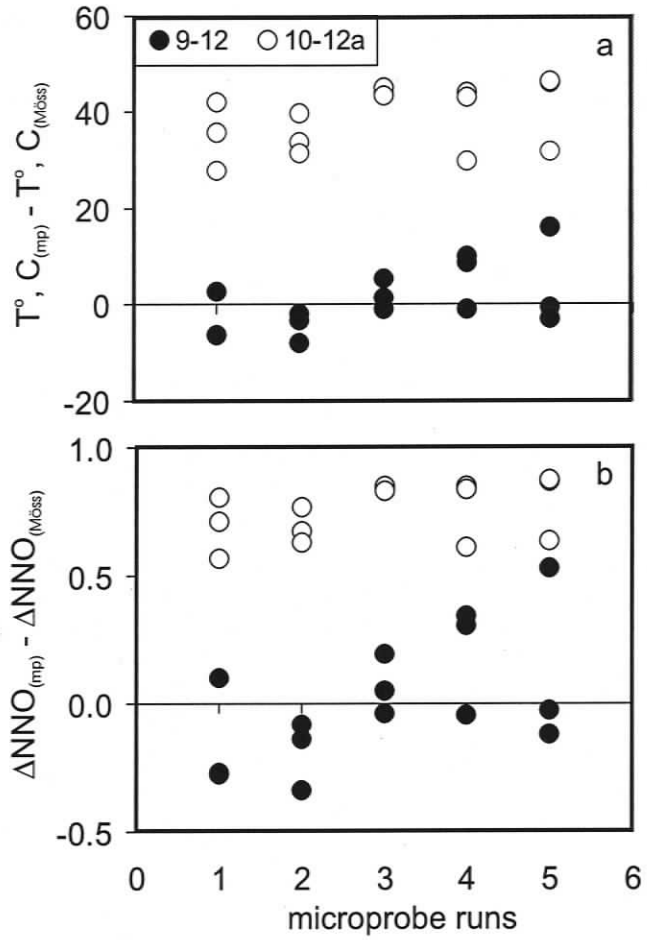

Figure 3.3 T fO_2 data obtained for two chromites with Fe^{3+} known from Mössbauer spectroscopy. The plots show differences in the (a) calculated temperature, and (b) fO_2 (expressed as ΔNNO) using microprobe data and Mössbauer spectroscopy data for Fe^{3+} in the two chromite grains.

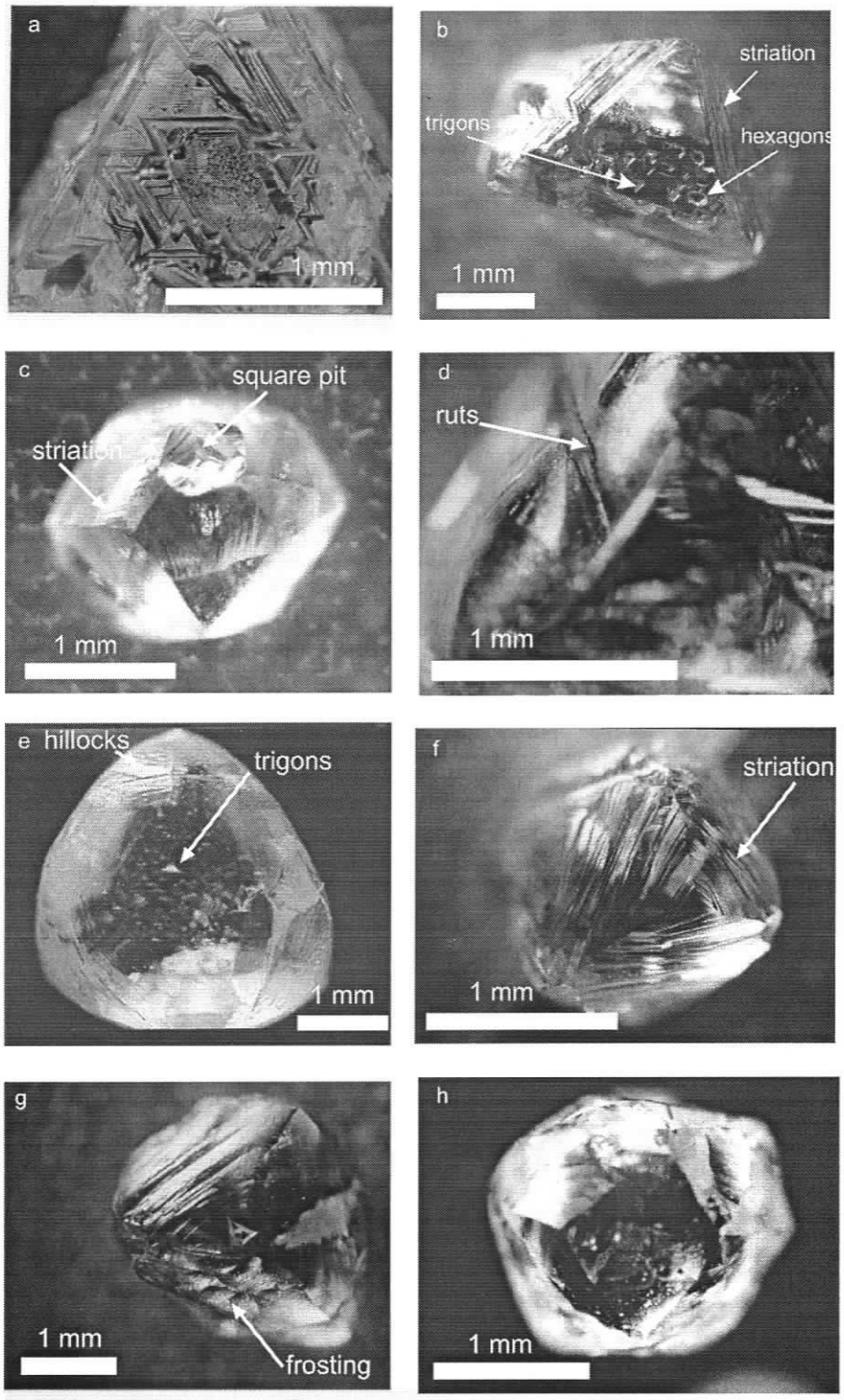

Figure 3.4 Examples of surface features in Lac de Gras diamonds used in this study: (a) Macle diamond with two types of trigon etch pits larger earlier trigons, and smaller later trigons. (b) Octahedral diamond with trigon and hexagon etch pits developed on face (111) and striation in the direction (110). (c) THH diamond with square pits developed on face (110) and striation. (d) Rut on a resorbed octahedron diamond. (e) Resorbed macle with hillocks and trigon pits. (f) THH diamond with striation. (g) Frosted surface of a resorbed octahedral diamond. (h) Glossy surface of THH diamond without any visible surface features.

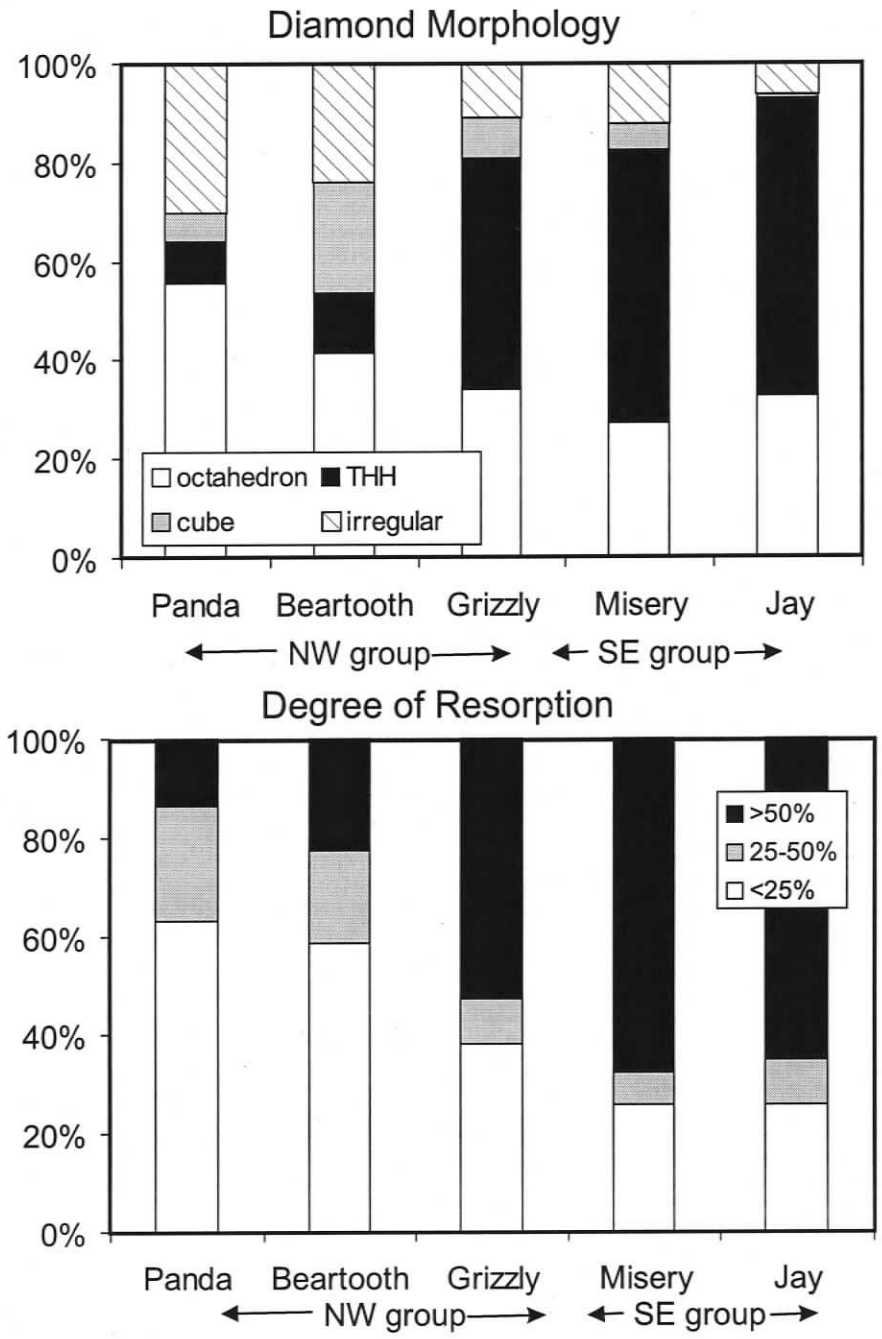

Figure 3.5 (a) Distribution of major morphological forms of diamond, and (b) proportion of variously resorbed octahedral diamonds in the Panda, Beartooth, Grizzly, Misery and Jay kimberlites. The plot shows the higher resorption for diamonds from the SE cluster of kimberlites.

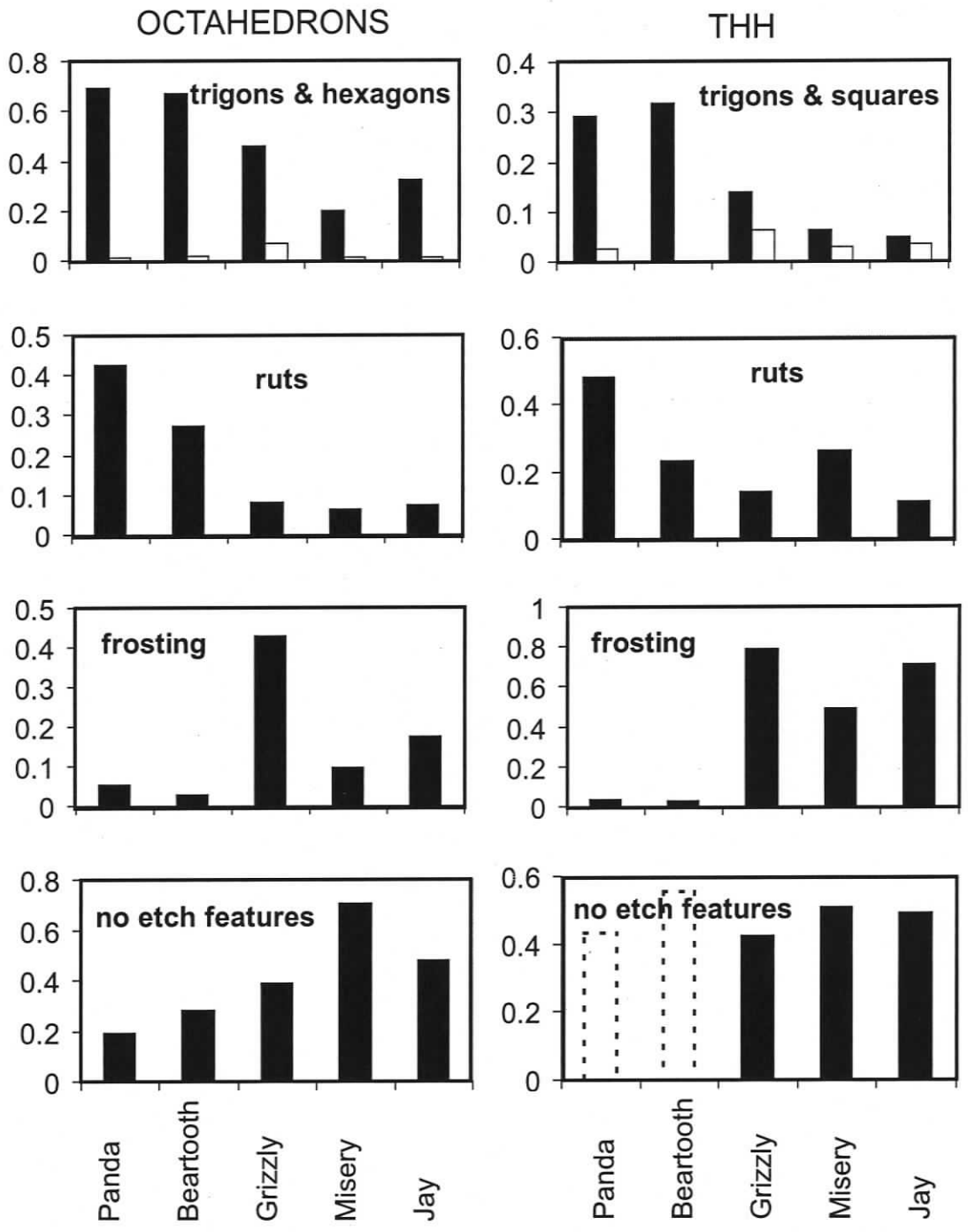

Figure 3.6 Proportions of stones with various surface features in octahedral and THH diamonds from the Panda, Beartooth, Grizzly, Misery and Jay kimberlites. Trigons are shown as black boxes, hexagons and squares as white boxes. The proportion of THH diamonds without etch features in Panda and Beartooth are shown as dash lines because the diamond descriptions for these parcels lack information on the presence of striations.

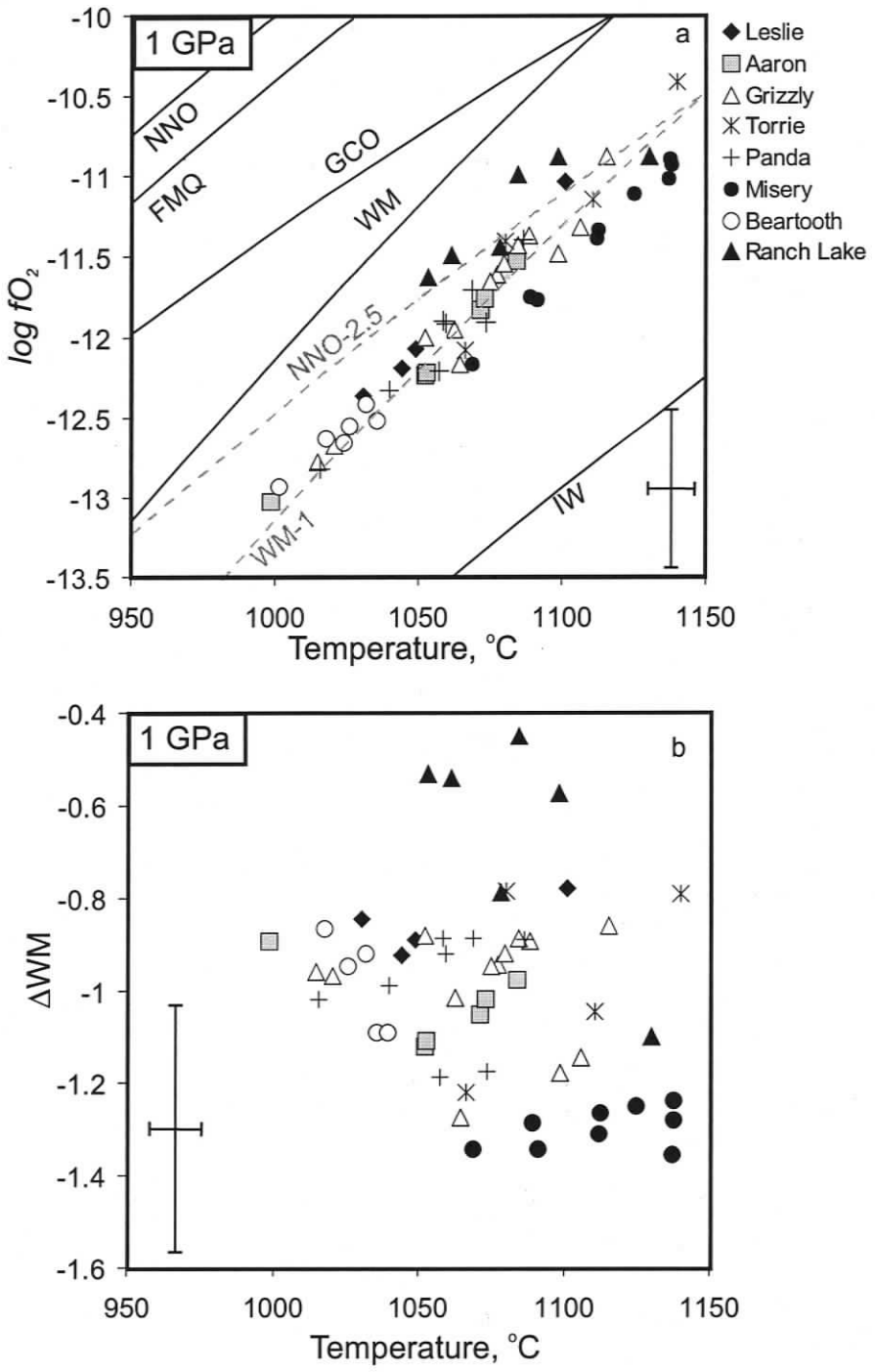

Figure 3.7 (a) Crystallization T and log fO_2 calculated from Ol-Sp thermometry and oxybarometry (Ballhaus et al. 1991) for eight Lac de Gras kimberlites compared to different oxygen buffers; fayalite magnetite quartz (FMQ) and nickel nickel oxide (NNO) , wustite- magnetite (WM) and iron-wustite (IW) ((O'Neill and Wall 1987; Frost 1991). The individual trends in each kimberlite are approximately parallel to the WM buffer and the relative differences between the kimberlites can best be seen relative to this buffer (b). Plot showing how the variations in T and fO_2 between the different kimberlites are larger than the precision of the method (shown as error bars).

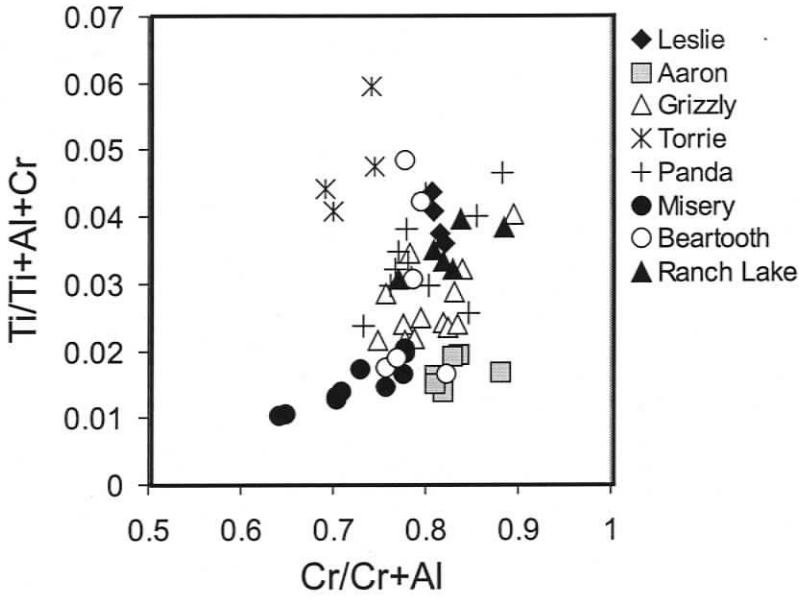

Figure 3.8 Composition of aluminous magnesian chromite inclusions in olivine phenocrysts from the eight Lac de Gras kimberlites. The plot shows that chromites from different kimberlites differ in Cr- and Ti- content.

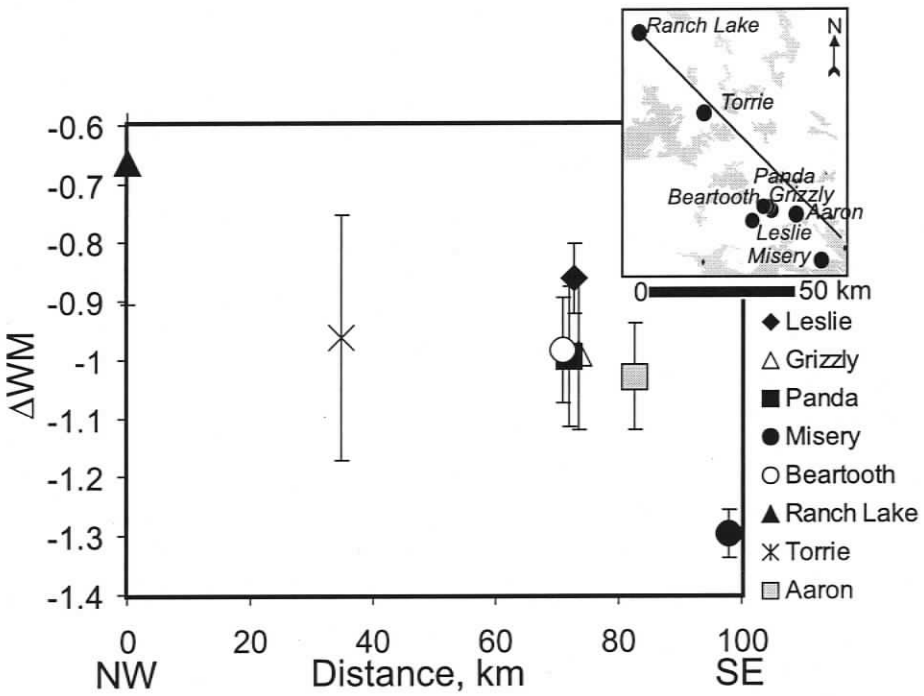

Figure 3.9 Change in fO_2 of kimberlites shown relative to WM buffer ($\log fO_2$ sample fO_2 WM buffer at P and T) from NW to SE in the Lac de Gras area. Note the general reduction of kimberlite melt in the SE direction. The distances are given on the line shown on the insert in the upper left corner.

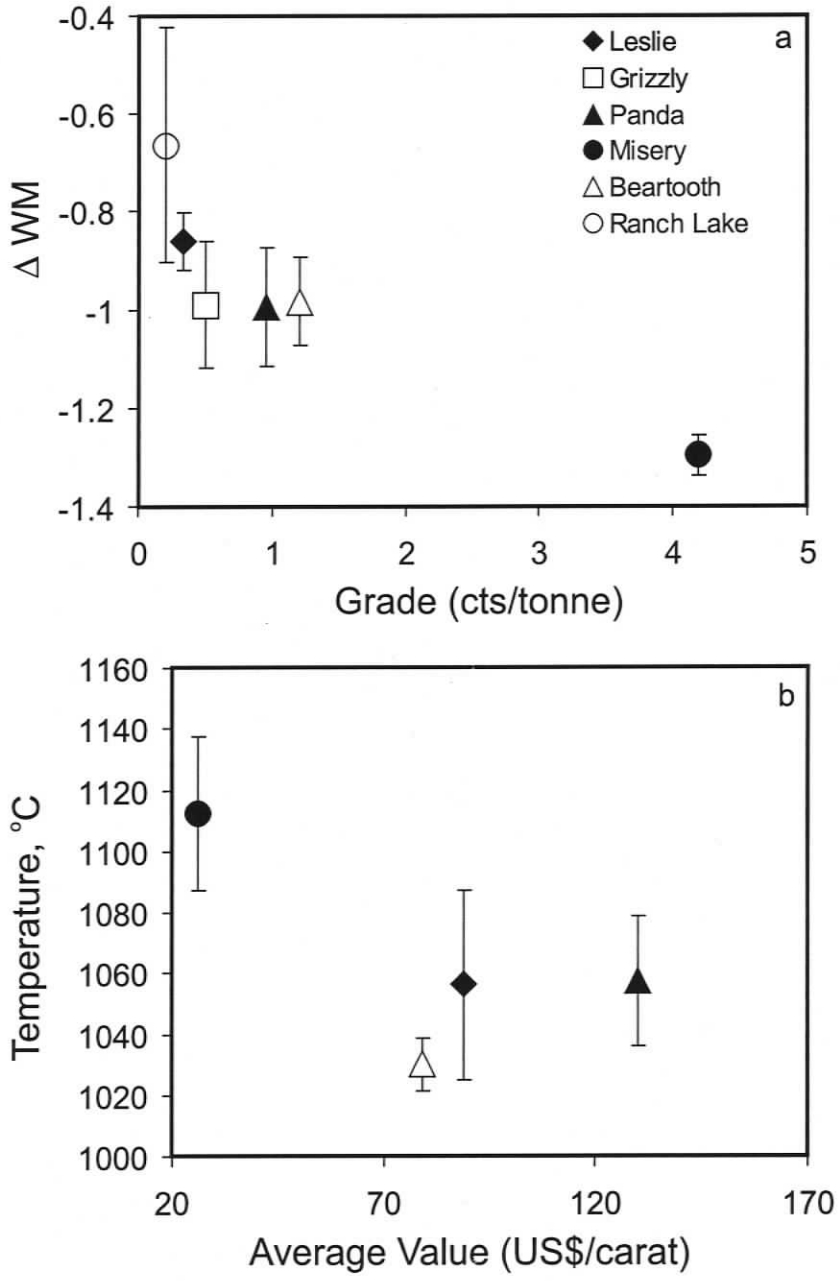

Figure 3. 10 Average values of fO_2 shown in ΔWM units vs. diamond grade of a kimberlite (carats/tonne). The error bars are one standard deviation. Diamond grades for Ekati pipes are from Natural Resources of Canada (http://www.nrcan.gc.ca/mms/cmy/content/1998/05.pdf) and for Ranch Lake from Cookenboo (1996).

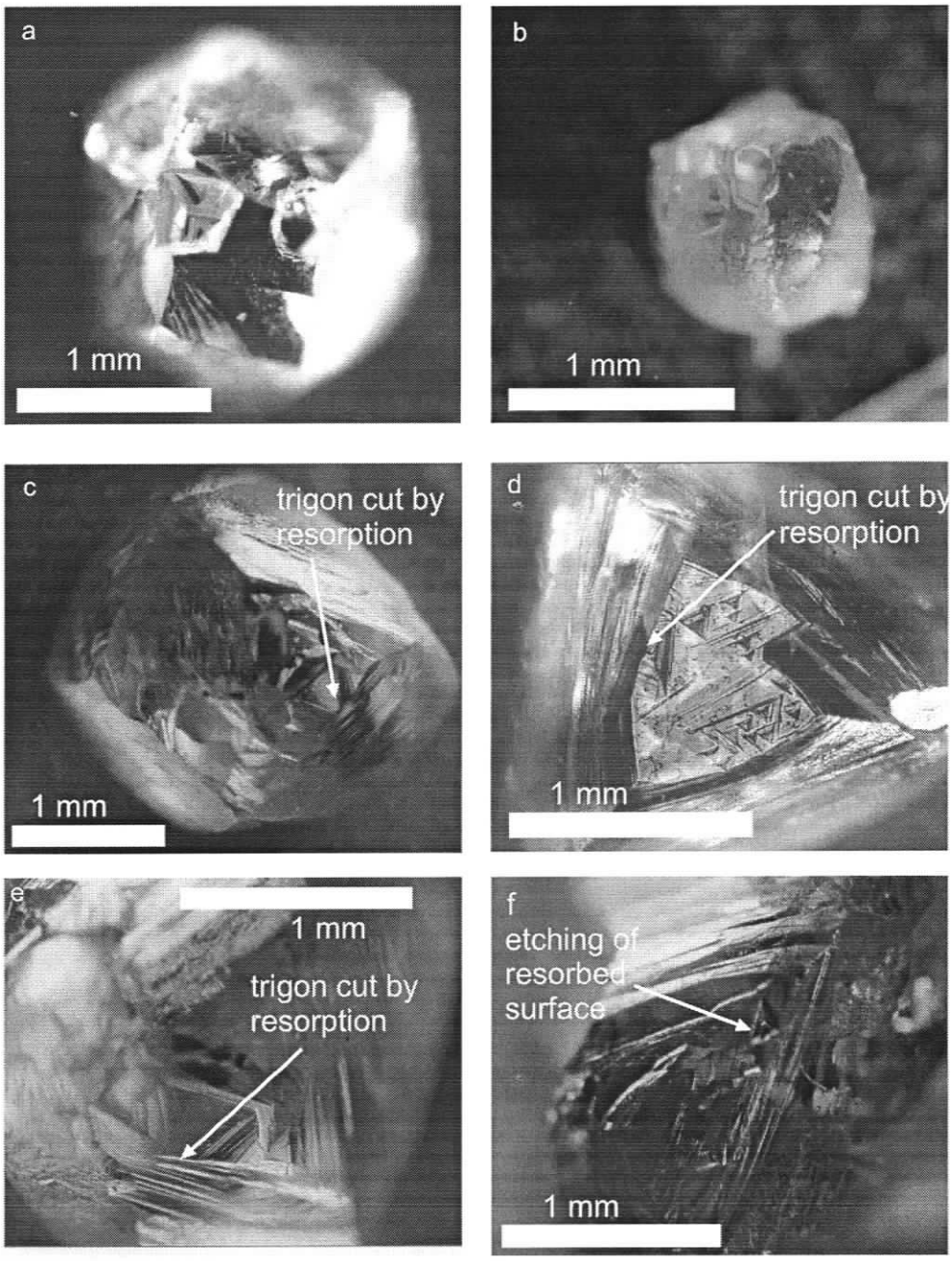

Figure 3. 11 Diamond photographs showing relationship between different dissolution forms: (a) Simultaneous formation of trigon and square pits(b) Non-etched remnant of octahedral face on a diamond completely rounded by resorption.(c, d, e) significantly resorbed octahedral diamonds with trigon pits cut by ditrigonal layers developed during resorption. (f) Trigon pits developed on a previously resorbed surface.

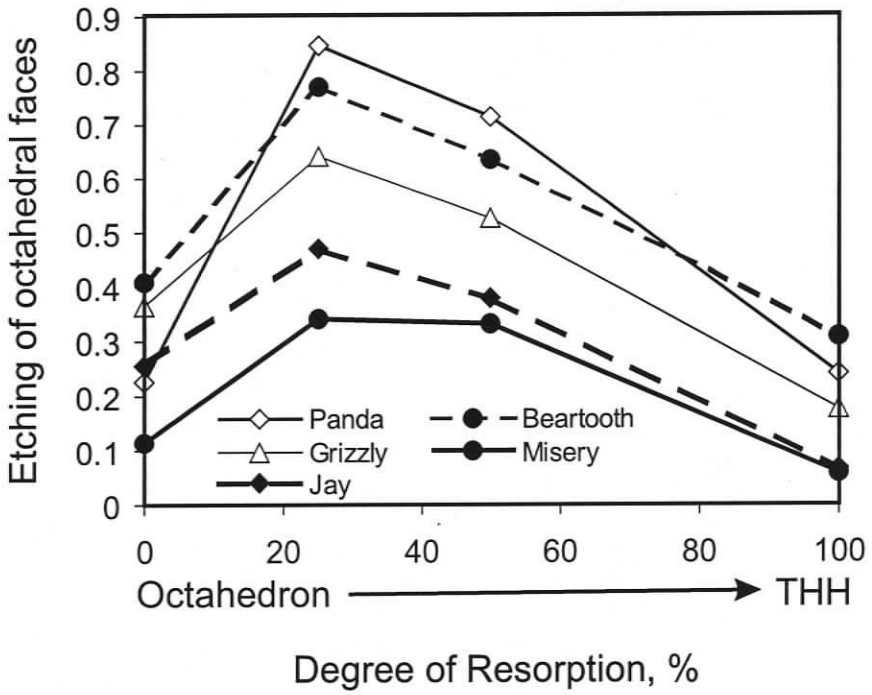

Figure 3. 12 Proportion of stones with trigon and hexagon pits in octahedral diamonds with different degrees of resorption. Degree of resorption shows percentage of octahedral faces resorbed (0% - unresorbed octahedron, <50% - THH). Note the lack of a positive correlation between resorption of primary octahedron and development of etch pits.

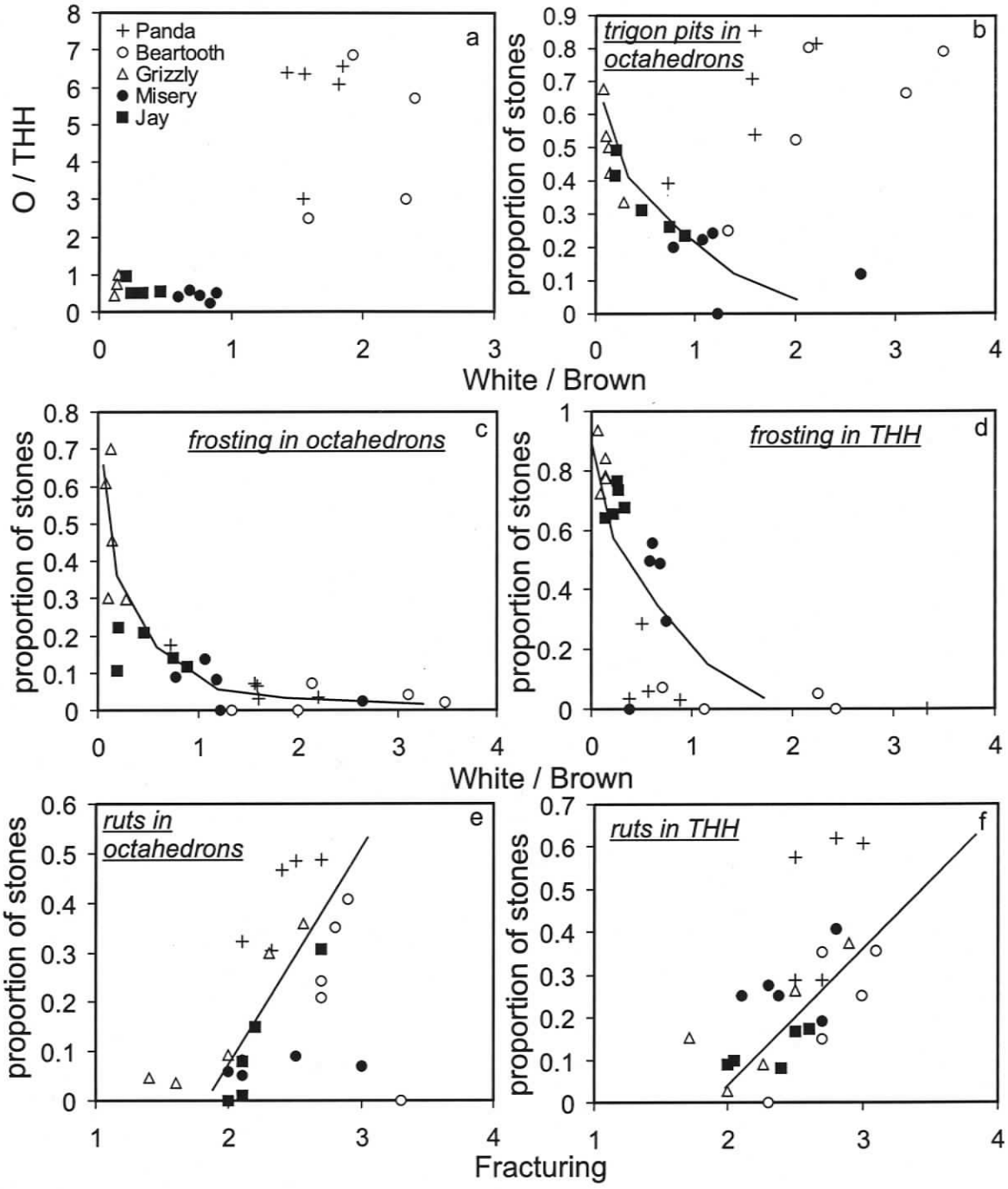

Figure 3. 13 Influence of diamond properties (colour and fractures) on the development of various dissolution forms in different diamond size groups for the Panda, Beartooth, Grizzly, Misery and Jay parcels. Only data for size groups with more than 100 stones are shown. (a) Degree of diamond resorption shown as octahedron to THH ratio (O/THH) vs. colorless/brown stone ratio (W/Br) for the five kimberlites.(b d) Higher proportion of stones with trigon pits (b) and frosting (c, d) in more brown diamond parcels. (e, f) Correlation between the presence of ruts on diamond surfaces and degree of internal fracturing. Fracturing ranges from 0 - no fractures present to 5 completely fractured stone and was calculated as an average for each size group.

CHAPTER 4

MECHANISMS OF DIAMOND OXIDATION AND THEIR BEARING ON THE FLUID COMPOSITION IN KIMBERLITE MAGMAS

Yana Fedortchouk

Dante Canil

School of Earth and Ocean Sciences, University of Victoria, Victoria, B.C., Canada

Elena Semenets

Gemological Research Inc., North Vancouver, B.C., Canada

4.1. ABSTRACT

Diamond oxidation experiments were undertaken in a piston-cylinder apparatus at 1350°C to 1500°C and 1 GPa in order to understand the mechanism of diamond oxidation in kimberlite melts and to determine the main rate-controlling parameters for this process. Only surface graphitisation, and no diamond resorption occur in melts that are fluid-undersaturated (synthetic kimberlite, carbonate melt, alkaline basalt, CaO-MgO-SiO_2-H_2O-CO_2 melts). In contrast, fluid over-saturated conditions (as evidenced by presence of bubbles) produce resorption features commonly seen in natural diamonds recovered from kimberlites. The diamond oxidation rate is the same in the melts with a free fluid phase, in a pure H_2O or CO_2 fluid, suggesting that the process of diamond oxidation is its reaction with the fluid and not with the melt. Both CO_2 and H_2O oxidize diamonds at a

similar rate, but produce very different surface features. Therefore, the surface features of natural kimberlite-hosted diamonds may provide information on the relative proportion of H_2O and CO_2 in the kimberlitic fluid. The common diamond morphologies imply significant amount of H_2O. The absence of diamonds with surface graphitisation and the abundance of resorbed diamonds in kimberlites suggest presence of free fluid phase in kimberlite magmas for hours or days. We found no correlation between the rate and character of diamond oxidation and the physical properties of diamonds (nitrogen content, colour).

Keyword: diamond oxidation rate, resorption features, experiments, fluid phase, kimberlite magmas, nitrogen content

4.2. INTRODUCTION

Natural diamonds have ubiquitous resorption features on their surfaces produced by interaction with their host magma during ascent (e.g. Robinson et al., 1989). The resorption results from diamond oxidation into CO_2 (Arima, 1998), has a significant impact on the diamond grade and the quality of stones of a kimberlite pipe, and may bear on their ascent and emplacement history. Many of the resorption features observed in natural diamonds have been produced by experiment (e.g. Chepurov et al., 1985; Kozai and Arima, 2005; Sonin et al., 2002), but the mechanism of this process is not completely understood yet. In order to determine the main rate-controlling factors for the diamond oxidation and to be able to predict the degree of diamond preservation in a kimberlite pipe, it is necessary to understand the mechanism of diamond oxidation in kimberlite magmas.

Experimental studies have shown a significant increase in the diamond oxidation rate with temperature (T) and oxidation state (fO_2) (Cull and Meyer, 1986; Evans and Phaal, 1961; Kozai and Arima, 2005; Sonin et al., 2000), which is also borne out in a general way in some natural kimberlites (Fedortchouk et al., 2005). The experiments by Kozai and Arima (2003) quantified the effect of T. A recent experimental study by Kozai and Arima (2005) on diamond dissolution in kimberlite and lamproite melts at 1 GPa shows significant change in the diamond dissolution rate between fO_2 fixed by hematite-magnetite (HM) equilibrium and iron-wustite (WI) equilibrium. All the previous experiments on diamond oxidation at controlled fO_2 involved etching in gases at 100 kPa but the results vary significantly between the different studies (Cull and Meyer, 1986; Evans and Phaal, 1961; Sonin et al., 2000). It is not also known whether diamond oxidation in gases proceeds by the same mechanism as in melts.

Much experimental work has focused on reproducing the many different surface resorption features found on natural diamonds by etching at variable T, pressure (P), H_2O content (e.g. Chepurov et al., 1985; Zhimulev et al., 2002) and in different melt compositions (Sonin et al., 2002). Nevertheless, the effect of each of those individual variables on the mechanism of diamond dissolution in kimberlite melts, or on the development of various surface etching forms is not completely understood.

Diamond is an unstable form of carbon in kimberlite melts and on the Earth's surface. A diamond can be converted to 1) graphite, 2) carbonate by the reaction with silicates or 3) oxidized. Diamond oxidation produces CO_2 and CO as the final products, and at certain conditions it is accompanied by surface graphitisation of diamonds (Evans and Phaal, 1961). Surface graphitisation is observed in some diamond dissolution experiments (Chepurov et al., 1985; Sonin et al., 1997) at temperatures much lower than

those required for "true" graphitisation and is believed to result from oxidation (Davies and Evans, 1972; Evans and Phaal, 1961). Graphitisation is almost never encountered on diamonds recovered from kimberlites (Sonin et al., 1997 and references therein). The diamond oxidation into CO_2 is a commonly accepted process of diamond dissolution (e.g. Arima, 1998). Arima (1998) and Kozai and Arima (2005) suggest that kimberlite melt dissolves diamond in the form of CO_2 and therefore CO_2 solubility in the melt controls the diamond dissolution rate. CO_2 solubility in turn depends on fO_2 and the composition of the melt (Kozai and Arima, 2005). Rudenko et al. (1979) argue that the physical dissolution of diamond in the melt is energetically impossible due to the very high energy required to break the three C-C bonds on the surface of the diamond lattice (Rudenko et al., 1979) and contend that only chemical oxidation through the diamond interaction with molecules of volatiles (e.g. CO_2, H_2O, CH_4, CO etc) is energetically possible. They therefore suggest that kimberlite melt itself cannot dissolve a diamond, but rather that the reaction with the fluid phase is required for the oxidation to proceed.

In the present study we explore the effect of fluids on diamond resorption in kimberlite magma systems (melt and/or fluid). We performed a series of diamond oxidation experiments in several synthetic compositions with various amounts of H_2O and CO_2 and conditions close to the experiments of Kozai and Arima (2005). We demonstrate that oxidation in volatile-undersaturated melts results in surface graphitisation of diamonds, not their resorption. The presence of a free fluid phase is required to produce the resorption features observed on natural diamonds. We further investigate the kinetics of diamond oxidation, the changes in diamond morphology and the character of etch surface features produced by oxidation of diamond in H_2O and CO_2 fluids.

Our results allow us to discuss the mechanism of diamond oxidation in kimberlites and to propose what determines the crystal morphology of a resorbed diamond; orientation and shape of etch pits and resorption forms on its surface. We further apply our results to characterize the fluid regime in kimberlite magmas.

4.3. METHODS

Both cubic plates and octahedral diamonds were used in the experiments. The plates (edges vary between 0.5 – 1.3 mm, ~ 1 mg) were cut from natural inclusion-free diamonds predominantly of IIa type (nitrogen-free). The octahedrons were selected from the <1 mm population from three Lac de Gras kimberlites, and are flat-faced crystals (1-2 mg) with no to little resorption, inclusions or cracks visible in an optical microscope. The octahedrons are IaAB and IaB type and with variable colour (Table 4.1). The diamonds were washed ultrasonically for 5 minutes in alcohol before and after each experiment.

The diamond oxidation experiments were conducted using synthetic compositions of natural aphanitic Jericho kimberlite (JD-82 from Price et al., 2000), natural Kettle River alkali basalt (Brearley and Scarfe, 1986), and a simple system CaO-MgO-SiO_2 kimberlite (volatile-free and with H_2O added) (Table 4.2). In order to do the experiments above the liquidus we subtracted 10 wt% of forsterite from JD-82 kimberlite composition. Pt capsules were used to contain volatiles. For this reason, FeO was replaced with CoO in both the kimberlite and alkaline basalt compositions to avoid Fe loss. The amounts of volatiles were modified to have them completely dissolved in the kimberlite (JK-4) and alkali basalt (KR13-3) melts during the experiments. A second alkali basalt composition (KR13-1) was prepared without volatiles. To prepare all synthetic compositions reagent grade SiO_2, TiO_2, Al_2O_3, MgO, CoO, MnO, $CaCO_3$, K_2CO_3, Na_2CO_3 were ground under

alcohol, decarbonated at 850°C and fused to a glass at 1500°C. The glass was then crashed and grounded in mortar, and H_2O and CO_2 were added as brucite and $CaCO_3$. The glasses were analyzed by EMP and the amount of volatiles in the final mixture was tested by loss on ignition at 900°C overnight. The oxidation experiments in pure H_2O fluid were loaded with brucite and run at T above the reaction:

$$Mg(OH_2) = MgO + H_2O \quad (9)$$

For the experiments in CO_2 fluid, a mixture of $CaCO_3$ and SiO_2 was run at T above the reaction:

$$CaCO_3 + SiO_2 == CaSiO_3 + CO_2 \quad (10)$$

At the run conditions, the kimberlite (JK-4) and alkaline basalt (KR13-1, KR13-3) compositions were above the liquidus. The compositions in CMS system at 1400°C consisted of glass with a few olivine grains at the bottom and at 1350°C – glass with olivine crystals making up about third of the charge. In this latter composition, the fO_2 during experiments was estimated by adding ~2 wt% of V_2O_5 to the mixture (composition CMSV-12/10 in Table 2). The fO_2 sensitive partition of V between the co-existing olivine and glass was measured by EMP and fO_2 values around nickel – nickel oxide (NNO) buffer was then calculated from Canil and Fedortchouk (2001) (Table 4.3).

For each experiment, about a third amount of starting mixture was packed at the bottom of a 3 mm diameter Pt capsule. The starting diamonds were photographed under an optical microscope from all sides and then weighed on a microbalance. One or two diamonds were then loaded and the remaining mixture was packed around the crystals. The capsule was sealed by arc welding and loaded in the pressure assembly. The capsule was weighed before and after the welding to ensure that no volatiles were lost.

The diamond oxidation experiments were conducted at 1200° – 1500°C and 1 GPa in a piston – cylinder apparatus with 12.5 mm NaCl/pyrex assemblies. For pressure calibration, we used the transition of Tschermak pyroxene to anorthite-gehlenite-corundum assemblage at 1300C and 1.3 GPa and 1400°C and 1.4 GPa (Hays, 1966b). The Tschermak pyroxene was prepared after Hays (1966a). The calibration showed less than 5% friction correction required for this assembly, similar to the 3% suggested by McDade et al. (2002). Therefore we did not use any friction correction in any experiments and the real pressure was slightly below 1 GPa. Temperature was measured with $W_{95}Re_5$ – $W_{74}Re_{26}$ thermocouple, the accuracy of which was confirmed by the method of Watson et al. (2002). For each experiment, the sample was brought to the final run pressure at 300°C, heated to 600°C and held for 6 min and then brought to the final run temperature. The pressure was adjusted during the heating, and after the run temperature was reached no more adjustments of the pressure were made. Quenching was achieved by terminating the power to the graphite furnace. The capsule and the matrix were closely studied after each run. An expanded capsule, release of traces of water during opening the capsule, wet MgO powder or an abundance of large bubbles in the glass for CMS compositions were used as criteria for the presence of fluid in the experiments.

Each diamond was used in three to five sequential experiments. In a few failed runs, the fluid was lost and the diamond developed surface graphitisation. The graphite was then removed in a short (20 or 30 min) run and the diamond was than used in the following experiments. After each run, the weight loss of the diamond was measured on a microbalance (+/- 0.02 mg). To avoid the effect of the variation in the starting weight of different diamonds on their oxidation rate, we calculated the oxidation rate as mg/mm^2

min^{-1}, since the use of mg/min and mm/min overestimate oxidation rate for large stones, and wt%/min – for smaller stones. For diamond plates, the change in the surface area was obtained by measurement of their three dimensions under an optical microscope. For the octahedron crystals, the surface area was calculated from their weight, density (3.52 mg/mm^3) and the shape. The shape was assumed to be a perfect octahedron for unresorbed stones and a perfect sphere after 40% of the initial weight was loss. The surface area then was calculated proportionally to the weight loss. After some experiments, octahedron diamonds were photographed under the optical microscope and the decrease of the surface area of octahedron (111) face was calculated using ImageJ software. The diamond surfaces were studied under an optical microscope and scanning electron microscope.

Electron microprobe analyses of starting compositions and olivines and glasses in V-doped experiments were done with a CAMECA SX50 electron microprobe at the University of British Columbia with 15.04 kV acceleration voltage, 20.1 nA beam current and 1 μm beam size. The counting time on peaks was 20 s for major elements and 100 s for V in olivines. Data reduction was done with the 'PAP' $\varphi(\rho Z)$ method (Pouchou and Pichoir, 1985). Natural and synthetic standards were used for calibration.

4.3.1. Diamond Properties

The octahedron diamonds were studied for the presence of fluorescence under UV light, colour and colour intensity, nitrogen content and aggregation state (Table 4.1). The nitrogen content and aggregation states were calculated by deconvolution of FTIR absorbance spectra of whole stones. The spectra were collected using an Avatar 360 FTIR

spectrometer at European Gemological Laboratories, Vancouver, at a resolution of 4 cm^{-1}. The spectra were deconvoluted using the method described in Hayman et al. (2005).

There are two types of diamonds in our experiments: IaB type with the low total nitrogen content (NT) and high proportion of aggregation centres B (nitrogen forms mainly 2 atom clusters) and IaAB that have both types of aggregation centers A and B (nitrogen forms 4 and 2 atom clusters) (Table 4.1). For the majority of the experiments we used colourless diamonds without fluorescence. One brown stone with high nitrogen content, one brown stone with low nitrogen content, two yellow octahedrons and one intensive yellow tetrahexahedron (THH) were used to compare the character of oxidation of diamonds with different physical properties.

4.4. RESULTS

4.4.1. Resorption vs Surface Graphitization

The experiments in volatile-undersaturated compositions (i.e. no free fluid) developed surface graphitization on diamonds (Table 4.4). Graphite was in various forms: a layer covering the entire stone, separate spots with frosted diamond surface in between, individual graphite crystals on the frosted diamond surface and pockets with long needle-like crystals of graphite. The relationship between the form of the graphite growth and the conditions of the experiments was not investigated. At 1450° and 1500°C, the diamond loses weight and is replaced with graphite, whereas at 1350°C the diamond gains weight by graphitisation, likely due to the rapid migration of C from the graphite heater through the Pt capsule into the sample during the experiment (Watson, 1987). After the removal of the graphite layer in a mixture of HNO_3 and H_2SO_4 acids heated at 200°C, the

diamonds show the irregular corrosion structures described in Sonin et al. (1997). Increase in CO_2 content of KR13-3 basalt (by addition of a $CaCO_3$ layer at the bottom of the capsule) resulted in suppressing the graphitisation (Table 4.4), but experiments in $CaCO_3$ alone produced a thick graphite layer on the diamond.

Experiments in volatile-oversaturated compositions produced no graphitisation on diamond, but resorption similar to the naturally produced in kimberlites (Fedortchouk et al., 2005) and in other diamond dissolution experiments (e.g. Kozai and Arima, 2005) (Table 4.4). Cubic diamond plates developed square etch pits on (100) faces and rounding of the corners and edges (Fig. 4.1d). Octahedrons developed trigon etch pits on (111) faces. Rounding of their edges and corners lead to a change in the morphology from octahedron to tetrahexahedron (THH), and development of striation features on the growing THH faces (Fig. 4.2c,d). The final morphology of a diamond with more than 40 wt% lost is a THH form with striations on all the sides –typical of natural diamond in kimberlites (e.g. Fedortchouk et al., 2005).

The effect of the presence and the amount of a free fluid phase on diamond oxidation is evident in the CMS synthetic kimberlite experiments (Fig. 4.1). In CMS kimberlite with 5wt% of H_2O, all fluid is in the melt (i.e. no free fluid phase) resulting in surface graphitisation (Fig. 4.1a). The same composition with 10wt% of H_2O, just above the fluid-saturation limit, produces no resorption, but large circular features on the diamond surface (Fig. 4.1b), usually referred as disks (e.g. Afanasiev et al., 2000). The further increase in the H_2O content resulted in square etch pits common for the (100) diamond face in natural diamonds (Fig. 4.1c and d). Higher H_2O contents favour larger etch pits (Fig 4.3ab, Fig. 4.3).

4.4.2. Character and rate of diamond oxidation in different media

The effect of fluid composition on diamond oxidation was studied in pure H_2O and CO_2 fluids. Carbon migration into the capsule during the experiments likely produced some C volatile species in the H_2O runs (Watson, 1987). Although a Pyrex sleeve in our pressure assembly significantly decreases H_2 migration through the walls of the Pt capsule into the sample, some H_2O in the runs with CO_2 fluid is still possible. When normalized to the surface area of the diamond, there is a similar rate of weight loss (within the uncertainties) for several diamonds oxidized in H_2O, CO_2 and CMSV-12/10 melt at the same conditions (Fig. 4.4a).

Diamond resorption can also be expressed as a decrease of the area of primary octahedron faces (111) during transformation into the secondary THH form. For the same amount of weight loss, diamonds etched in H_2O develop more profound resorption of the octahedron form than those etched in CO_2 (Fig. 4.2b,c,e,f). Numerically this difference is shown as a relationship between the preservation of the initial area of all octahedron faces or their remnants, and the preservation of the diamond's initial weight for several experimental runs (Fig. 4.5). The areas were measured on enlarged photographs of individual faces under optical microscope before and after experiments, calculated by ImageJ software, and averaged for each stone. For the diamonds with only a few faces photographed, only the faces where photographs were obtained for each run were used. We considered the octahedron face completely disappeared when no remnant of this face is observed under the microscope. There is much faster disappearance of octahedron faces in H_2O than in CO_2 (Fig. 4.5). The change in the rate of loss for the M32 and M56 diamonds is due to the fluid loss in the second run and development of surface graphitisation that decreased the weight without changing the diamond's morphology.

After the removal of the graphite layer in the subsequent run, the rate of (111) face loss for both diamonds became parallel to the other H_2O-etched stones. The strange behaviour of the yellow M41 diamond might be explained by a complex initial surface of this stone covered with many growth and resorption features.

H_2O and CO_2 fluids produce contrasting etch characteristics on diamonds. On the octahedron (111) face H_2O fluid produces few individual large flat-bottom trigons, whereas CO_2 covers the face with numerous smaller point-bottom trigons (Fig. 4.2e). Similar differences are observed on (100) cubic face of diamond plates (Fig. 4.6). On the THH faces H_2O produces striations along the former octahedron edges, and CO_2 covers the whole surface with slightly elongated drop-shaped irregularities called hillocks (Fig. 4.2g). Other features produced only in H_2O fluid are shown in Fig. 4.7 (a,c,g,h) and those produced only in CO_2 fluid on Fig. 4.7 (b,d,e,f). Oxidation in the two fluids results in a different shape of the trigon pits (Fig. 4.8). Resorption also exposes deformation lamellae on the colorless and brown diamonds (Fig. 4.7g). The lamellae were observed only in the runs with H_2O fluid, but we do not have enough data to rule out their exposure during oxidation in CO_2 fluid. The fluid composition during the most recent etching event dictates the final morphology and overprints the previous features produced in a different fluid. For example, diamond M57 was oxidized in H_2O during five runs, but the final run in CO_2 fluid (P-277 Table 4.5, 2 hours) resulted in the typical "CO_2 etch surface" (Fig. 4.2g).

4.4.3. Oxidation of different diamonds

Oxidation rates of various diamonds are similar for all the diamonds and do not vary with colour (colorless, light brown, dark brown, light yellow, dark yellow) or nitrogen content

(from 35 to 1200 ppm) (Fig. 4.4b). Two yellow octahedrons M41 and M39 lost their yellow colour after one or two runs. The two possible reasons are: 1) lost of yellow colour at our experimental conditions; and 2) only the outer layer of these stones had yellow colour and it was removed making the diamond colourless. To test this possibility we did two runs with a diamond having strong yellow colour, THH morphology and a broken side (M4, Table 4.1) to ensure that the internal part of the diamond is exposed and has the same colour as the outer layer. This stone gave the same oxidation rate as the others and no loss or lightening of the colour, suggesting removal of the yellow outer layer from the colourless core on M41 and M39 diamonds. Surface etch features produced on different stones are similar at the conditions of our experiments.

4.5. DISCUSSION

4.5.1. Mechanism of diamond oxidation in kimberlite melt

The results of our experiments suggest that the presence of a free fluid phase is required to produce diamond resorption observed in natural diamonds (i.e. the change of the primary octahedron diamond into THH and development of etch trigons). Any oxidation reaction by diamond interaction with a volatile species dissolved in a melt or the melt components results in surface graphitisation. At the volatile-saturation limit of the melt we observed no surface graphitization, no changes in diamond morphology, but development of large disk sculptures, similar to those occasionally encountered in natural kimberlitic diamonds (Afanasiev et al., 2000). Thus, the oxidation in the melt just above its volatile-saturation limit causes resorption, but the kinetics of the process at this point is very slow. At conditions in which the melt is sufficiently fluid-oversaturated the resorption proceeds. The character and kinetics of the resorption is the same in volatile-

saturated melt as in a pure fluid, but the size of etch pits and their number may vary. We therefore suggest that the most accurate term for the process that causes diamond resorption should be named "oxidation" and not "dissolution".

The diamond oxidation rate in our experiments obtained at 1350°C, 1 GPa and fO_2 slightly above WM buffer compares well with the rate recorded by Kozai and Arima (2005) for diamond oxidation in Wesselton aphanitic kimberlite (Fig. 4.9) oversaturated in volatiles (Kozai and Arima, 2005, in methods). This consistency between two different studies, supports our observation that oxidation in pure fluid is the same as in the melt-fluid (i.e. magma) systems and represents the process of diamond oxidation in the natural kimberlite magmas.

Since the fluid phase, and not the kimberlite melt, oxidizes diamond, its conditions determine the kinetics of resorption. Kozai and Arima (2005) argue that CO_2 solubility in the melt determines the oxidation rate, because they observed that addition of 30 and 50 wt% of $CaMg(CO_3)_2$ to the Wesselton aphanitic kimberlite suppressed the oxidation, and experiments in pure $CaMg(CO_3)_2$ produce surface graphitisation. We suggest an alternative explanation for their observation. Addition of the carbonate greatly increases water solubility in the melt (Keppler, 2003) and consequently could greatly decrease the amount of fluid in the system down to the saturation limit, decreasing the diamond oxidation rate as observed by Kozai and Arima (2005). The surface graphitisation produced in $CaMg(CO_3)_2$ agrees with our data and is caused by the absence of a free (H_2O or CO_2) fluid phase. Kozai and Arima (2005) obtained much slower diamond oxidation in lamproite than in kimberlite. Their lamproite composition had significantly less volatiles than the kimberlite, especially CO_2, which has a lower

saturation limit. As a result, this lamproite might not have had enough fluid to fully support the oxidation.

The $H_2O - CO_2$ fluid system of kimberlite melts (Mitchell, 1986) has the following volatile species: H_2O, H_2, CH_4, CO, CO_2 (Holloway and Blank, 1994). The mole fraction and the activity of these species in the oxidation reaction with the diamond surface would depend primarily on T and fO_2. It is possible that the components of the melt react with the products of diamond oxidation in the fluid phase (CO_2, H_2) and affect the amount of reactants and products in the diamond oxidation reaction. In this case, the melt composition could affect the oxidation rate, but if this process operates, it probably has a very minor effect. The results of the present study suggest that as long as a melt is fluid-saturated, the T and fO_2 of the system will determine the kinetics of diamond oxidation.

Diamond resorption and the development of surface graphitisation are the two competitive processes of diamond oxidation. The activation energies for surface graphitisation of (111) and (110) diamond faces are 1059±75 and 728±50 kJ/mol respectively (Davies and Evans, 1972), corresponding to the energy required to break three or two C-C bonds of the diamond lattice (energy of one bond is 347 kJ/mol, from Rudenko et al. (1979). The activation energy of diamond oxidation by resorption is ~ 364 – 427 kJ/mol (Cull and Meyer, 1986, and our unpublished data) and corresponds to the breakage of one C-C bond. Rudenko et al. (1979) argue that energetically the most favourable process of diamond oxidation is through the attachment of volatile molecules (H_2O, CO_2, CH_4, etc) to the carbon open bonds on the diamond surface. The reaction of the components of these molecules with the surrounding C atoms breaks the remaining C-

C bonds one by one, to form new C-OH, C-O, C-H… etc. bonds, whose energy of formation is higher than the energy required to break a single C-C bond. These various C-O-H-OH compounds then break down into CO and CO_2, the final products of diamond oxidation. With this process, the C atom detaches from the diamond lattice by breaking only one C-C bond, in agreement with the measured activation energy. Thus, diamond oxidation by H_2O-CO_2 fluid is the fastest process and it produces diamond resorption, whereas in the absence of the fluid, the less energetically favourable surface graphitisation proceeds.

4.5.2. What determines the morphology of resorbed diamonds?

At the conditions of our experiments we found no effect of the fluid composition on the kinetics of diamond oxidation, but a great influence on the surface forms and morphology produced by the resorption. In nature, diamond resorption in kimberlite melts produces a variety of surface forms. The most common are negative trigon and square etch pits (Fig. 4.10 a,b) the shape, orientation, and number of which greatly vary in natural diamonds. The less common resorption features are: hexagons, disks, cavities, positive trigons. Variation in the degree of volume resorption and surface etching can produce resorbed diamonds with clear untouched remnants of octahedron faces, or well-preserved octahedrons completely covered with etch pits. Striation and hillocks are the two most common etch features on THHs and show a great variation in shape even within one diamond population (Fedortchouk et al., 2005). The morphological changes of diamond during resorption affect the yield during diamond cutting, and therefore the quality of a stone. It is important, therefore, to constrain what determines the final morphology of a resorbed diamond.

Several previous experimental studies found that different solvents and the variation in the H_2O content of melts produce different surface etch features on diamonds (Chepurov et al., 1985; Pal'yanov et al., 1995; Sonin et al., 2002). The presence of surface graphitisation during diamond oxidation in dry alkali basalt was mentioned in Chepurov et al. (1985). Yamaoka et al. (1980) studied the influence of T and fO_2 on the orientation of trigon etch pits, where negative trigons required lower fO_2 and higher T. They suggested that the relative oxidation rates in (100) and (110) directions determined the pit orientation (Fig. 4.10a), whereas at high fO_2 and low T the oxygen forms C-O-C bridges and stabilizes the oxidation in (100) direction (Yamaoka et al., 1980, and references therein).

The diamond morphologies produced by resorption in H_2O and CO_2 fluids in our experiments differ significantly and are summarized in Table 4.6. They agree well with Kozai and Arima (2005) data and represent the end-members of the surface resorption features produced by diamond oxidation in kimberlite with 6.2 wt% H_2O and 4.8 wt% CO_2 (Fig. 1b,d,f in Kozai and Arima, 2005). This example shows that the development of the surface resorption features is predictable from the fluid composition, at least for the H_2O-CO_2 system.

Following Yamaoka et al. (1980, and references therein) we explain the diversity of the surface features in our experiments by the differences in the relative oxidation rates in the three main directions of the diamond lattice (111), (110), (100) (Table 4.6 and Fig. 4.10a). What determines the variation of the oxidation rates may be hidden in the differences in the diamond lattice in these three directions. The position and distance between the open bonds in the diamond lattice is different in (111), (110) and (100) directions. Different volatile species in H_2O-CO_2 fluid also vary in size and configuration,

and therefore, would probably prefer attachment on certain directions of the diamond lattice. The activity of different volatile species in the fluid would affect the relative oxidation rates in the different directions and, as a result, the diamond morphology. To define the relationship between the activity of volatile species and the relative oxidation rates in the different directions of diamond structure, more experimental studies are needed. Our preliminary experiments show that increase in CO_2 of fluids results in higher oxidation rates in (111) direction.

4.5.3. Influence of diamond properties on their oxidation

In the Lac de Gras kimberlite pipes, brown diamond populations often have a much higher degree of resorption, whereas diamonds from kimberlites with mainly colourless stones are less resorbed (Gurney et al., 2004). This may have resulted from a very different history of the diamond populations, or simply from faster resorption of brown diamonds. Mendelssohn and Milledge (1995) suggested that the variation in the amount of the defects of diamond structure such as nitrogen impurities and plastic deformation (the common explanation for the brown colour of diamonds), might affect diamond oxidation rates. We tested the effect of diamond properties on their oxidation rate and resultant surface resorption features by putting two different diamonds in the same experimental run, and by repeating runs at the same conditions with different diamonds.

Similar oxidation rates and surface resorption features are observed for low-nitrogen, high-nitrogen, colourless, brown, and yellow stones (Tables 4.1 and 4.5, Fig. 4.4b). If the oxidation rate is affected by the physical properties of a diamond, these differences are within the uncertainties of our experimental method, and therefore, are

very small relative to the effect of T and fO_2 on the preservation of diamonds in kimberlites.

4.4.4. Fluid regime in the Lac de Gras kimberlites, diamond preservation and quality

Many lines of petrological data for kimberlites indicate a high volatile content. A large amount of carbonates in their groundmass implies high content of CO_2 in the fluid (e.g. Price et al., 2000). The exact fluid composition of kimberlite melts, however, is not well constrained due to ambiguity in the primary composition of kimberlites, their protracted emplacement history, the overprint of deuteric alteration and complex origin of some groundmass carbonates and hydrous minerals. The relationships between diamond morphology and the presence and composition of fluid observed in this study can help us to learn more about the fluid in kimberlite magmas and the proportions of the major volatiles – H_2O and CO_2 during their emplacement

Given our experimental observations, the amount of resorption experienced by the diamonds can also be used to infer the time in which a free fluid phase existed in a kimberlite system. THH, the secondary diamond morphology, is present in diamond populations of many kimberlites (e.g. Gurney et al., 2004) and requires at least 40% of the initial weight loss of a diamond. On the contrary, the diamonds with surface graphitisation are almost never found (Sonin et al., 1997, and references therein) requiring the presence of fluid phase during the latest stages of kimberlite emplacement. As an example using our experimental data, the time required to produce a THH form from a 1 cm octahedron diamond at the NNO buffer is three days at 1350°C and 0.5 days

at 1500°C. For a 0.5 cm long diamond this time is 35 hours and four hours respectively (Fig. 4.11). In comparison to the rapid emplacement rates of kimberlite magmas – hours and days (Canil and Fedortchouk, 1999; Kelley and Wartho, 2000) these times suggest that in order to produce the resorbed diamonds found in the majority of kimberlites, a fluid phase should be present through a significant part of their emplacement history. Otherwise, the majority of the resorption could only have happened in the mantle source. Surface graphitisation removed by later resorption could not produce such a high degree of diamond oxidation due to the much slower kinetics of this process.

Our experiments showed similar diamond oxidation rates in H_2O and in CO_2 fluids at the conditions of kimberlite magma during its ascent (Fig. 4.4a). However, the experiments at 100 kPa and 870°C by Rudenko et al. (1979) produced a five-fold difference in diamond weight loss between oxidation in pure CO_2 and pure H_2O vapour. It is, therefore, possible that the composition of the fluid might affects the diamond oxidation rate at the surface conditions.

Our experiments clearly show that resorption in H_2O and in CO_2 fluid produced very different surface features (Table 4.6). The majority of diamonds in the Panda, Beartooth, Misery kimberlites, Lac de Gras field, (Fedortchouk et al., 2005) show well-formed individual trigon etch pits, striation on the resorbed edges along the octahedron faces and on the surface of THH stones. Hillocks are common, but they have a round pyramid shape, similar to those produced in our experiments with H_2O. All these features indicate that at the last stages of kimberlite emplacement, the fluid reacted with the diamonds from these pipes was mostly H_2O with the H_2O/CO_2 ratio much higher than

those of proposed for the primary kimberlite melts of Wesselton (Shee, 1986) and Jericho (Price et al., 2000).

In our experiments we observed that diamond surface features record only the composition of the last fluid with which they reacted. Therefore, at this point we cannot tell much about the composition of the fluid in the kimberlites earlier history and evolution. A detailed study of the evolution of diamond surface features at variable fluid composition compared to the features of different diamond groups within one population may shed more light on the evolution of kimberlitic fluid through the time.

4.6. CONCLUSIONS

Diamond oxidation experiments at 1350°C and 1 GPa produced the resorption common for natural diamonds but only in the presence of a fluid phase. Diamond oxidation in melts undersaturated with fluid results in a surface graphitisation. Our results support proposition by Rudenko et al. (1979) that the reaction with the fluid and not with the kimberlite melt is responsible for resorption. We suggest substituting the term "diamond dissolution" with "diamond oxidation" as a more accurate description of this process in nature.

At the conditions of kimberlite emplacement the fluid composition (its H_2O/CO_2 ratio) does not affect diamond oxidation rate, but does influence the surface features produced during the oxidation. For this reason, T and fO_2 of the system have the major control on the diamond preservation.

The physical properties of the diamond (nitrogen content and aggregation state, colour) do not notably change its oxidation rate and cannot influence preservation of diamond populations.

Surface resorption features of diamonds record information on the composition of kimberlitic fluid at least at the late stages of the kimberlite evolution. Diamonds from the Panda, Beartooth, and Misery kimberlite pipes in the Lac de Gras kimberlite field are indicators of a fluid with high H_2O/CO_2 ratio.

The absence of surface graphitisation on diamonds in the majority of kimberlite pipes requires presence of a fluid phase at the final stages of kimberlite emplacement. The presence of secondary THH diamond morphologies among small and large stones requires fluid phase present in kimberlite magmas for hours or days that is comparable with the time estimated for the ascent and emplacement of kimberlite magma. The time during which kimberlite magma coexists with a fluid phase greatly affects the degree of diamond preservation.

ACKNOWLEDGMENTS

We thank Jon Carlson, Darren Dyck and BHPBilliton Diamonds Inc. for providing us the diamonds for our experiments. Branko Deljanin and European Gemological Laboratories, Vancouver are thanked for help with collecting FTIR spectra and Patrick Hayman for the help with deconvolution of the spectra. We thank Valentin Afanasiev for valuable suggestions on the diamond resorption experiments and Stephen Parman for shearing his experience in experimental procedure. We thank Bruce Kaye and Defence Research and Development Canada for the help with obtaining Back Scatter Electron Images. Mati Raudsepp helped with MP analyses at UBC. This research was supported by NSERC graduate scholarship to YF and NSERC Discovery Grant to DC.

Table 4.1 Properties of natural diamonds used in diamond oxidation experiments

Diamond	IaA NA (2 atoms) ppm	IaB NB (4 atoms) ppm	N total, ppm	Colour/ Intensity
M31	nd	nd	nd	colourless
M32	5.04	39.21	44.25	colourless
M34	3.67	36.78	40.45	colourless
M39	1.26	34.46	35.72	light yellowish-green
M41	0.74	34.28	35.01	yellowish-green
M45	4.10	30.77	34.87	dark brown
F4	263.01	276.91	539.92	colourless
M56	235.37	994.46	1229.83	light brown
M57	167.18	891.75	1058.93	colourless
M63	0.54	47.64	48.17	colourless
M4	32.70	1165.79	1198.50	intense yellow

Table 4.2 Starting compositions

oxide	JK-4	KR13-1	KR13-3	CMS-1	CMS-12/3	CMS-12/5	CMS-12/10	CMSV-12/10
SiO2	31.95	45.40	46.83	49.50	45.03	44.00	42.28	41.41
TiO2	0.93	2.73						
Al2O3	2.10	17.63	15.03					
CoO	8.97	13.41	11.40					
MnO	0.21	0.15						
MgO	23.75	7.29	6.71	28.51	29.03	28.34	27.28	26.71
CaO	21.73	10.78	9.49	17.49	15.94	15.66	14.94	14.63
Na2O	0.25	0.07	3.37					
K2O	0.60	0.86	1.17					
V2O5								2.08
H2O	6.52		3.00	4.50	10.00	12.00	15.50	15.18
CO2	3.00		3.00					
Total	100.00	98.31	100.00	100.00	100.00	100.00	100.00	100.00

JK-4 – modified Jericho aphanitic kimberlite JD-82 (from Price et al., 2000); KR13-1 and KR13-3 - natural alkali basalt modelled after (Brearley & Scarfe, 1986); CMS-1, CMS-12/3, 5, 10 and CMSV-12/10 – a simple system CaO-MgO-SiO_2-H_2O kimberlite.

Table 4.3 Olivine and glass compositions in experiments in CMSV-12/10 mixture and the fO_2 values calculated from $D_v^{ol/gl}$ after (Canil and Fedortchouk, 2001).

Sample	MgO	SiO2	CaO	V2O5	Total	Dv ol/gl	ΔNNO*	logfO2**	ΔWM**
P245-gl	30.3	48.9	16.84	2.01	98.1	0.042	-0.2	-5.9	0.8
P245-ol	57.6	42.3	0.33	0.09	100.3				
P246-gl	27.8	49.7	17.60	2.01	97.1	0.056	-0.6	-6.4	0.3
P246-ol	57.0	42.7	0.35	0.11	100.2				
P248-gl	30.1	49.7	17.78	2.01	99.6	0.029	0.5	-5.2	1.5
P248-ol	57.3	42.2	0.34	0.06	99.9				
Average						**0.042**	**-0.1**	**-5.8**	**0.9**

* - calculated from logDv=-0.24ΔNNO-1.41 (Canil & Fedortchouk, 2001).
** - the equations for NNO and WM buffers are from Frost (1991)

Table 4.4 Results of diamond oxidation in different compositions (Cc – $CaCO_3$).

Composition	H2O, wt%	CO2, wt%	T (°C)	Surface graphitization	Resorption	Bubbles in the matrix
JK-4	6.5	3	1500	layer	weight loss	absent
KR13-1	0	0	1300	minor	no	absent
KR13-3	3	3	1200	spots	no	absent
KR13-3	3	3	1400	thin layer	no	absent
KR13-3+Cc	3	>3	1200	absent	no	bubbles on quench
CaCO3			1450	extensive	undetermined	
CaCO3			1500	extensive, spots	undetermined	
CMS-1	5		1400	layer	undetermined	bubbles on quench
CMS-1+H2O	12-13		1400	absent	resorption, etch pits	bubbles
CMS-12/10	15.5		1400	absent	resorption, etch pits	bubbles
CMS-12/5	12		1400	absent	minor, small pits	bubbles
CMS-12/3	10		1400	absent	no resorption, disks	bubbles
CMSV-12/10	15.5		1350	absent	resorption, etch pits	bubbles
Mg(OH)2	100		1350	absent	resorption, etch pits	bubbles
CaCO3+SiO2		100	1350	absent	resorption, etch pits	bubbles

Table 4.5 Experimental conditions and results of diamond oxidation experiments at 1 GPa

Run no.	Diamond	Composition	Temperature (°C)	Duration (min)	Initial weight (mg)	Weight loss (mg)[a]	Total Preservation(wt%)[b]	Area (mm^2)[c]	Area weight loss (mg/mm^2)	Preservation of (111) face (%)[d]
Runs in fluid undersaturated melts										
P-220	IIa	KR13-1	1300	30	1.4	nd				
P-221	IIa	JK-4	1500	30	0.8	nd				
P-222	IIa	JK-4	1500	90	nd	nd				
P-226	IIa #25	KR13-3	1200	60	1.1	nd				
P-228	IIa #32	KR13-3	1400	64	0.8	nd				
P-227	IIa #31	KR13-3+Cc	1200	60	0.7	nd				
P-229	IIa #35	CaCO3	1450	30	0.53	nd				
P-230	IIa #38	CaCO3	1500	30	0.6	nd				
P232	IIa	sDi-1	1400	30	nd	nd				
Runs in melt with free fluid phase										
P235	IIa	CMS-1+H2O	1400	30	nd	nd				
P238	IIa	CMS-12/10	1400	30	nd	nd				
P239	IIa	CMS-12/5	1400	30	nd	nd				
P240	IIa	CMS-12/3	1400	30	nd	nd				
P241	IIa	CMS-12/10	1350	60	nd	nd				
P244	IIa	CMSV-12/10	1350	60	nd	nd				
P245	M32	CMSV-12/10	1350	60	1.98	0.11	94	3.90	**0.028**	48.9
P246	M57	CMSV-12/10	1350	60	2.02	0.1	95	3.95	**0.025**	60.4
P247	M45	CMSV-12/10	1350	60	1.04	-0.06	106	2.54	**-0.024**	
P248	M56	CMSV-12/10	1350	60	1.59	0.07	96	3.37	**0.021**	52.4
P252	M45	CMSV-12/10	1350	120	1.1	0.09	97	2.54	**0.035**	
P254	M41	CMSV-12/10	1350	60	1.33	0.21	84	2.99	**0.070**	77.6
P256	M34	CMSV-12/10	1350	120	2.15	0.11	95	4.12	**0.027**	49.5
P-280	M32	CMSV-12/10	1350	120	1.78	0.08	86	3.49	**0.023**	20.4
Runs in H2O fluid										
P249	IIa	Mg(OH)2	1350	60	1.11	0.37	67	nd	**nd**	
P250	M31	Mg(OH)2	1350	120	1.61	0.11	93	3.40	**0.032**	28.1
P258	M34	Mg(OH)2	1350	20	2.04	0.08	91	4.04	**0.020**	
P259	M34	Mg(OH)2	1350	120	1.96	0.21	81	3.87	**0.054**	
P260	M34	Mg(OH)2	1350	180	1.75	0.25	70	3.44	**0.073**	0.3

Table 4.5 (continued).

P-263	M34	Mg(OH)2	1350	360	1.5	0.41	51	2.94	**0.139**	
P-264	M45	Mg(OH)2	1350	180	0.91	0.11	77	2.19	**0.050**	
P-266	M45	Mg(OH)2	1350	180	0.8	0.11	66	1.92	**0.057**	
P-275	M45	Mg(OH)2	1350	120	0.69	0.07	60	1.67	**0.042**	
P-264	M57	Mg(OH)2	1350	180	1.85	0.25	79	3.61	**0.069**	2.6
P-266	M57	Mg(OH)2	1350	180	1.6	0.22	68	3.11	**0.071**	
P-275	M57	Mg(OH)2	1350	120	1.38	0.08	64	2.69	**0.030**	
P-273	M41	Mg(OH)2	1350	130	1.07	0.11	72	2.37	**0.046**	
P-274[e]	M41	Mg(OH)2	1350	120	0.96	0.1	65	2.15	**0.047**	22.0
P-276	M41	Mg(OH)2	1350	120	0.86	0.18	51	1.93	**0.093**	
P-273	M56	Mg(OH)2	1350	130	1.32	0.18	72	2.78	**0.065**	
P-274	M56	Mg(OH)2	1350	120	1.14	0.13	64	2.40	**0.054**	
P-276	M56	Mg(OH)2	1350	120	1.01	0.21	50	2.14	**0.098**	
Runs in CO2 fluid										
P-285	IIa 42,46	CaCO3+SiO2	1350	60	1.45	0.41	72	nd	**nd**	
P255	IIa43	CaCO3+SiO2	1350	60	0.6	0.17	72	2.012	**0.084**	
P255	M63	CaCO3+SiO2	1350	60	1.58	0.15	91	3.35	**0.045**	64.9
P-269	M63	CaCO3+SiO2	1350	195	1.43	0.18	79	3.02	**0.060**	28.3
P-277	M57	CaCO3+SiO2	1350	120	1.3	0.18	55	2.54	**0.071**	
P-278[e]	M39	CaCO3+SiO2	1350	60	2.09	0.19	91	4.04	**0.047**	
P-278	F4	CaCO3+SiO2	1350	60	1.33	0.09	93	2.99	**0.030**	71.9
P-279	F4	CaCO3+SiO2	1350	120	1.24	0.13	83	2.78	**0.047**	40.0
P-282	F4	CaCO3+SiO2	1350	120	1.11	0.12	74	2.48	**0.048**	27.2
P-279	M4	CaCO3+SiO2	1350	120	2.09	0.16	92	3.57	**0.045**	
P-282	M4	CaCO3+SiO2	1350	120	1.93	0.18	84	3.30	**0.054**	

[a] - for graphitized diamonds weight loss is often negative due to gaining graphite
[b] - preservation of the initial weight of the starting octahedron diamond
[c] - area is calculated from weight, density and the shape of the diamond (100% preserved - octahedron, 60% preserved - sphere)
[d] - preservation of (111) faces represent the proportion of the initial diamond surfaces
[e] - the runs when a yellow diamond lost its colour

Table 4.6 Diamond morphology and surface features produced in H_2O and CO_2 fluids at 1350°C and 1GPa and relative oxidation rate in the different directions of diamond lattice.

Resorption features	H2O fluid		CO2 fluid	
	surface features	relative oxidation rate	surface features	relative oxidation rate
preservation of primary octahedron shape	fast rounding of crystal	(100),(110) faster	longer preservation of sharp edges and (111) surfaces	(111) faster
orientation of etch pits	negative	(110)<(100)	mainly negative with some positive features	(110)</=(100)
size/shape of etch pits	large, flat-bottom trigons	(111) slow	small, pointed-bottom trigons	(111) fast
density of etching	few trigons on unresorbed (111) face	(111) slow	numerous trigons cover the whole (111) face	(111) fast
features on THH faces	striation		drop-like hillocks	

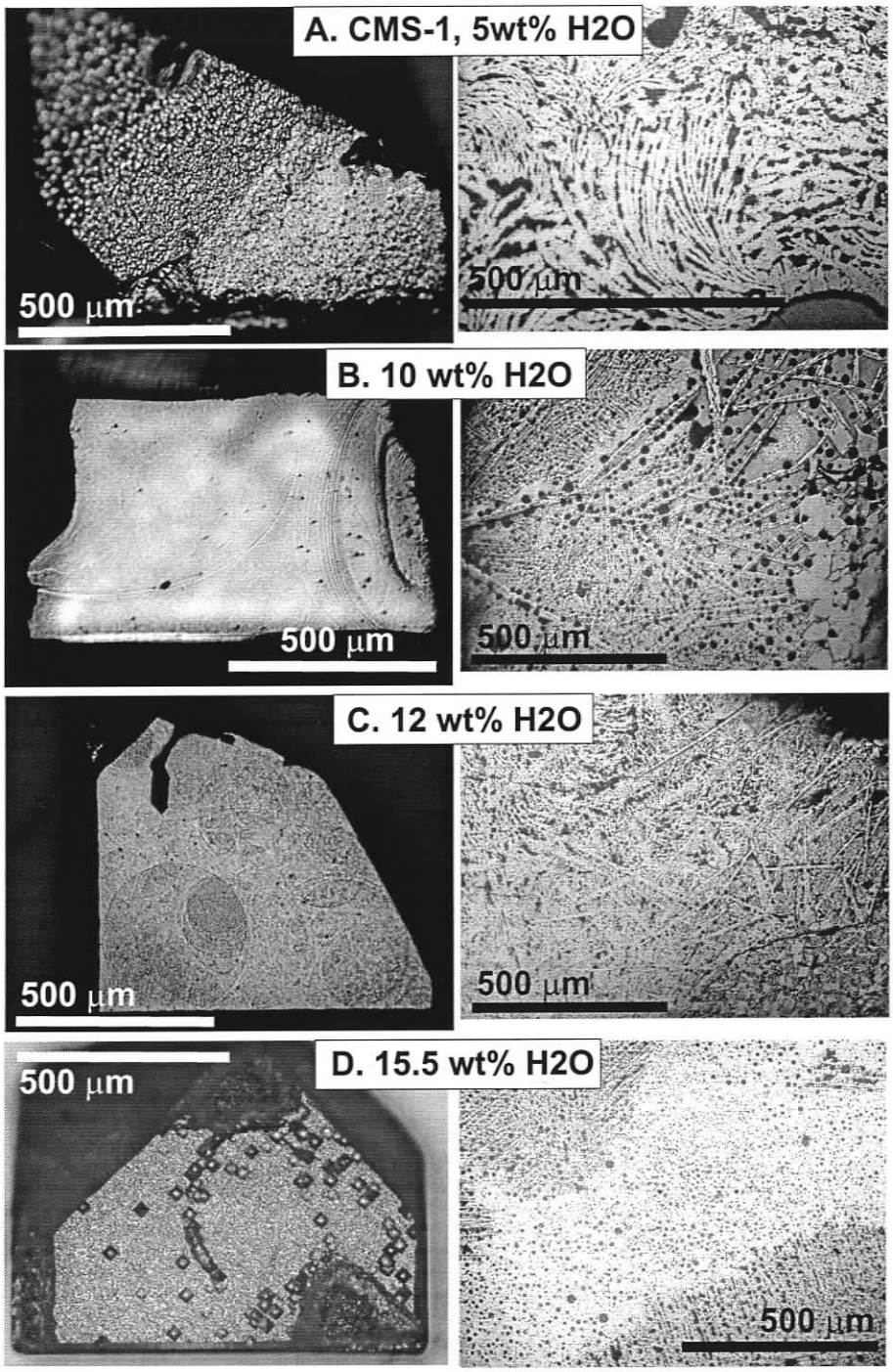

Figure 4.1 Diamond surface after oxidation experiments in melts with variable amount of fluid. The coexisting matrix around the diamond with the amount and structural position of the bubbles is shown for each experiment. All photographs were taken under an optical microscope. A) in H_2O-undersaturated melt (bubbles only form during quench i.e. along the quench crystals) and diamond develops surface graphitisation; B) at the H_2O-saturation limit or slightly above no etch pits formed, almost/ or no visible resorption, disk forms on diamond surface; C) very small amount of free fluid surface etching, small rare etch pits; D) more fluid (bubbles in the glass) widespread development of etch pits.

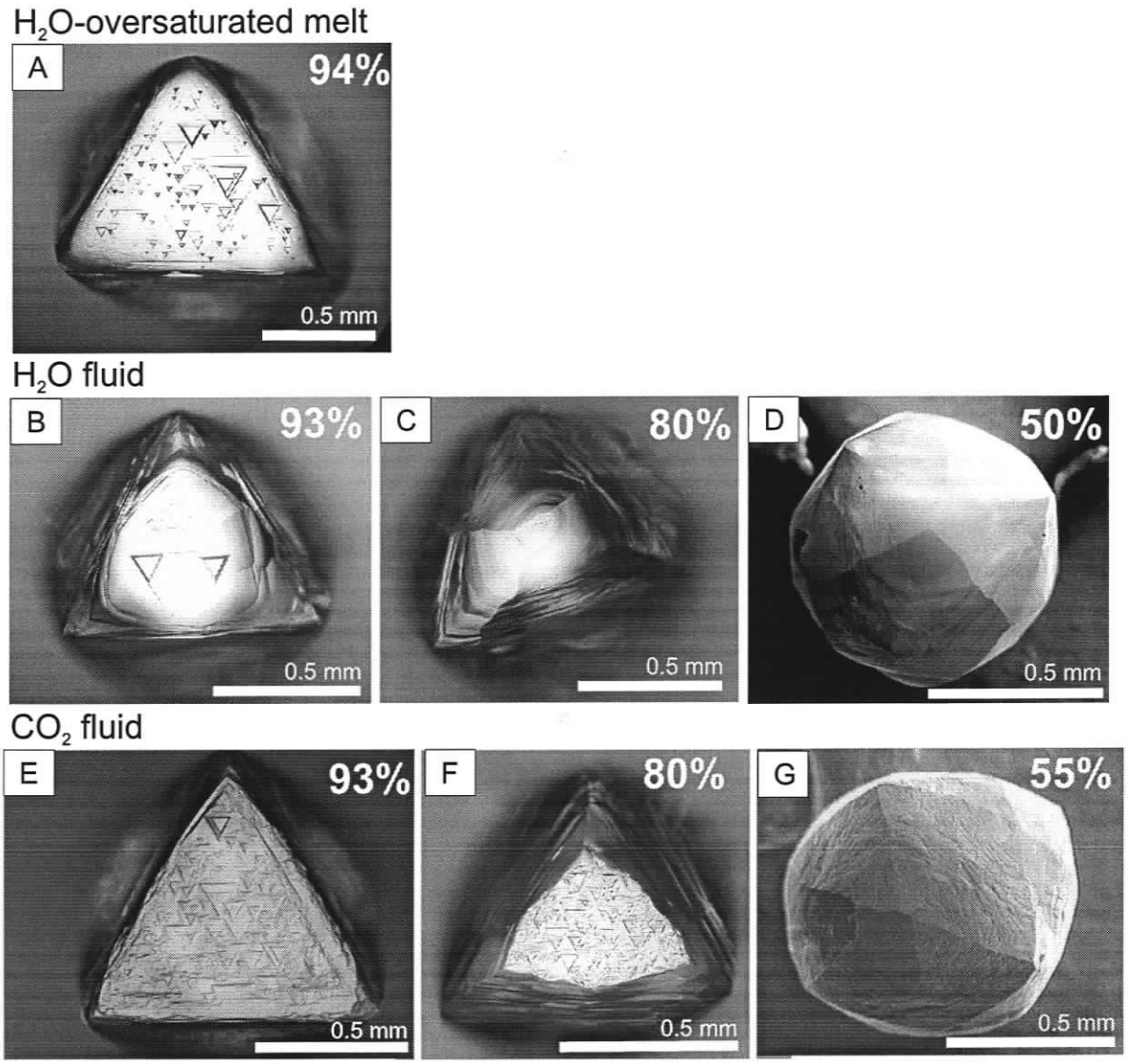

Figure 4.2 Different character of resorption during diamond oxidation in H_2O-oversaturated melt (a), H_2O fluid (b-d) and CO_2 fluid (e-g). The numbers given in percent represent preservation of the diamond's initial weight. Note the larger trigon pits produced in H_2O fluid, and more complex patterns of etching in CO_2 fluid. (111) octahedron face disappears faster when diamond oxidized in H_2O than in CO_2 fluid. The THH forms are covered with striation when etched in H_2O (d) and with hillocks when etched in CO_2 (g). D and G are back scatter electron images, others are photographs under the optical microscope.

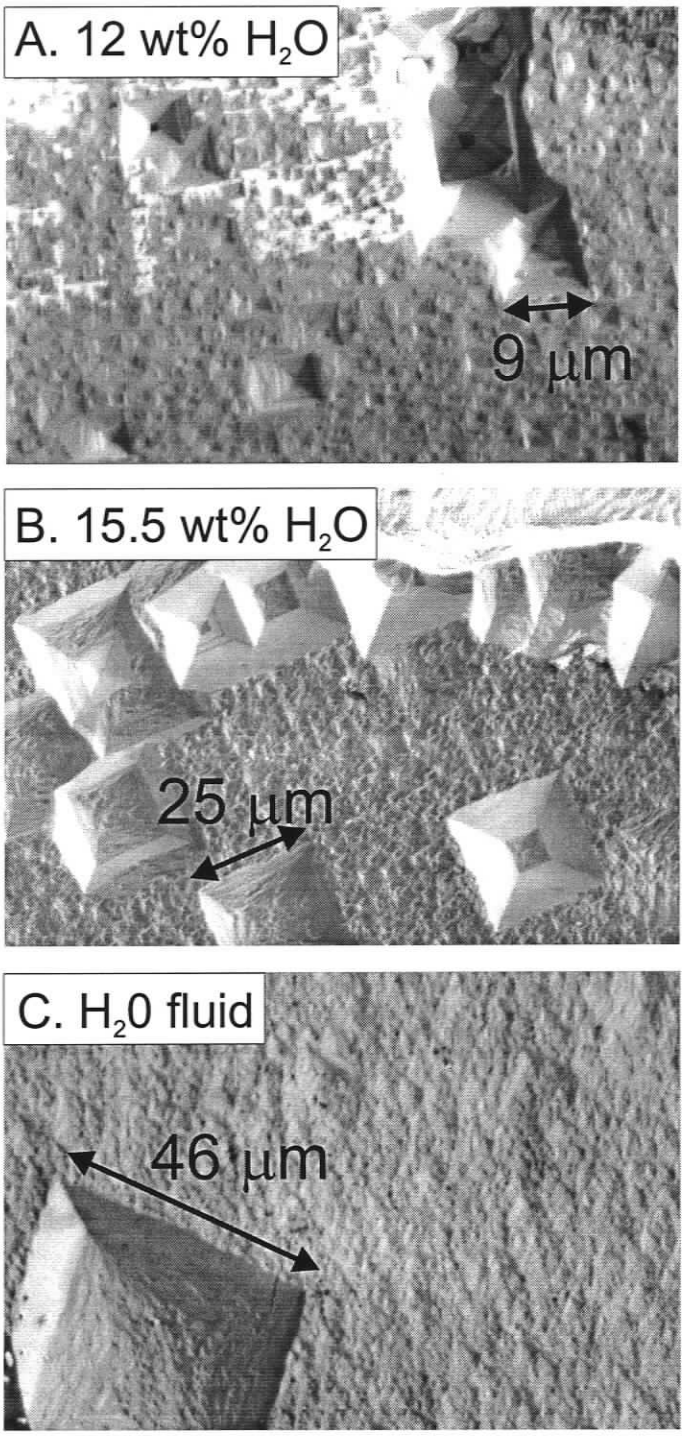

Figure 4.3 Enlargement of the etch pits with an increase of H_2O content of the melt (back scatter electron images).

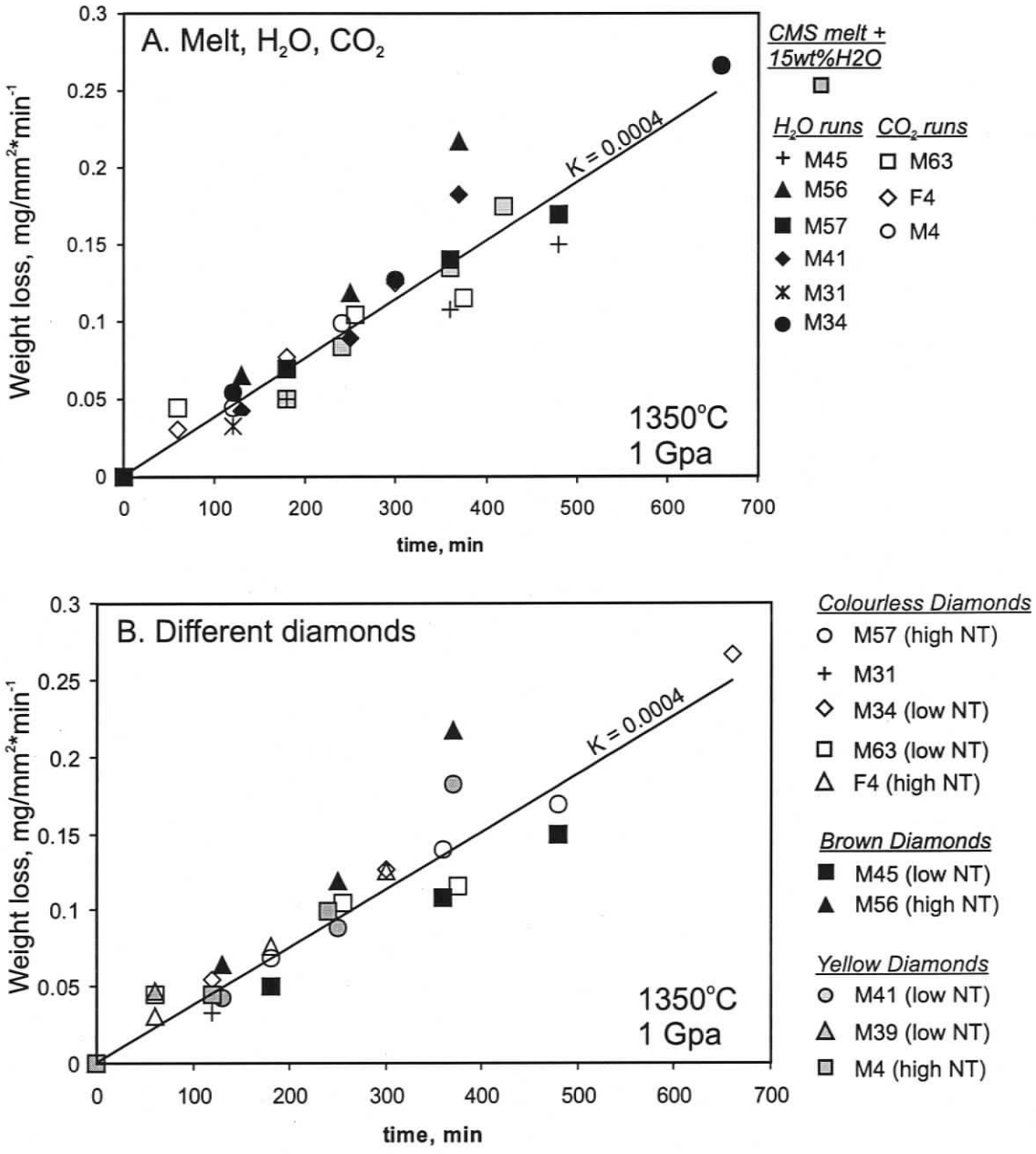

Figure 4.4 Oxidation rate of natural octahedron diamonds in the experimental runs at 1350°C and 1 GPa in piston-cylinder apparatus. The plot shows no difference in the kinetics of diamond oxidation in different reagents (a) and for diamond with various properties (b). The two points with the higher oxidation rate on the both plot are from the same experimental run, which might have slightly different conditions. Low and high nitrogen content of the diamonds indicated as NT (total nitrogen). All error bars are smaller than the size of the symbols.

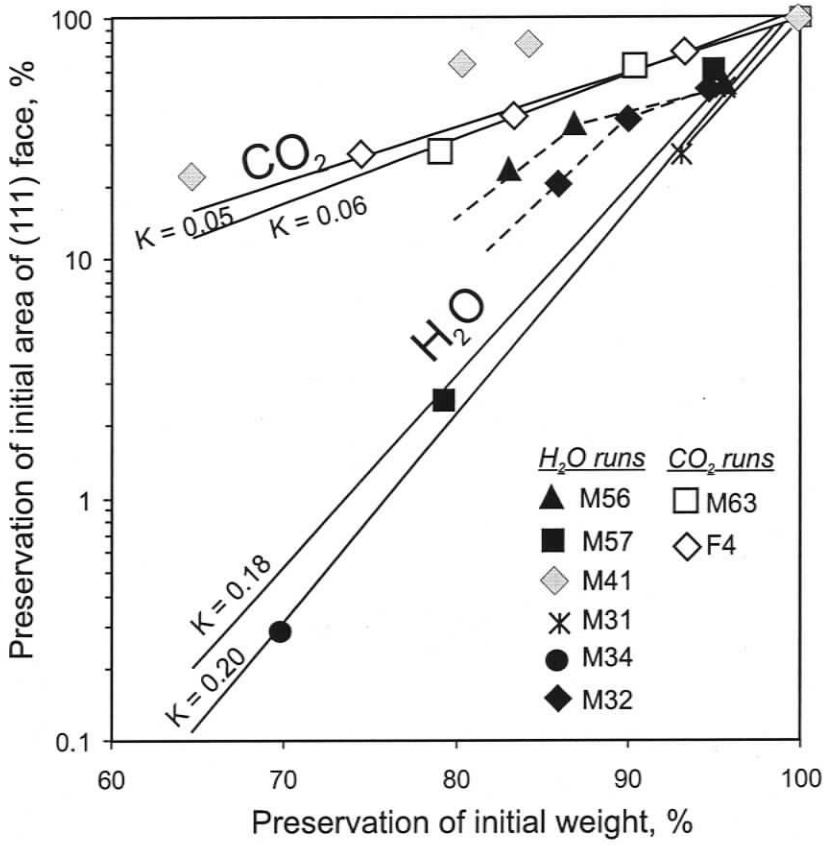

Figure 4.5 Decrease in the area of (111) octahedron face of the initial diamond vs. the initial weight loss during oxidation in H_2O and in CO_2 fluids showing longer preservation of the diamond's primary morphology in CO_2 fluid. Change in slope in M32 and M56 lines is due to surface graphitisation between the second and following runs.

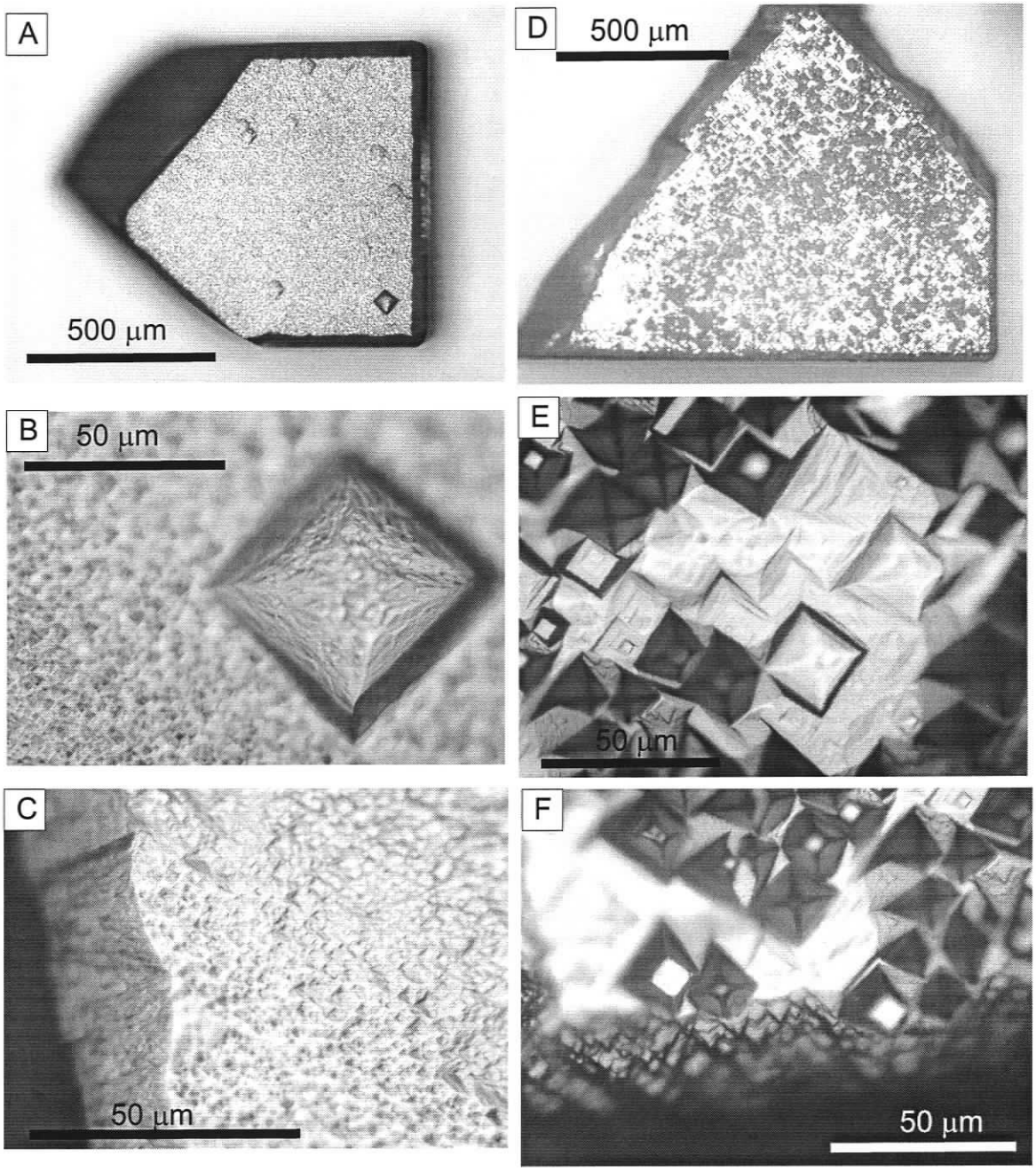

Figure 4.6 Different character of etching of (100) face of a cubic diamond plate in H_2O (run P-249) and CO_2 (run P-285) fluids. Oxidation in H_2O produces few large square pits on intensively etched diamond surface (A-C), whereas oxidation in CO_2 produces many smaller square pits with more regular shape and pointed-bottom (D-F). Surface etch features on the diamond edge ((110) direction) also differ between the two fluids (C and F).

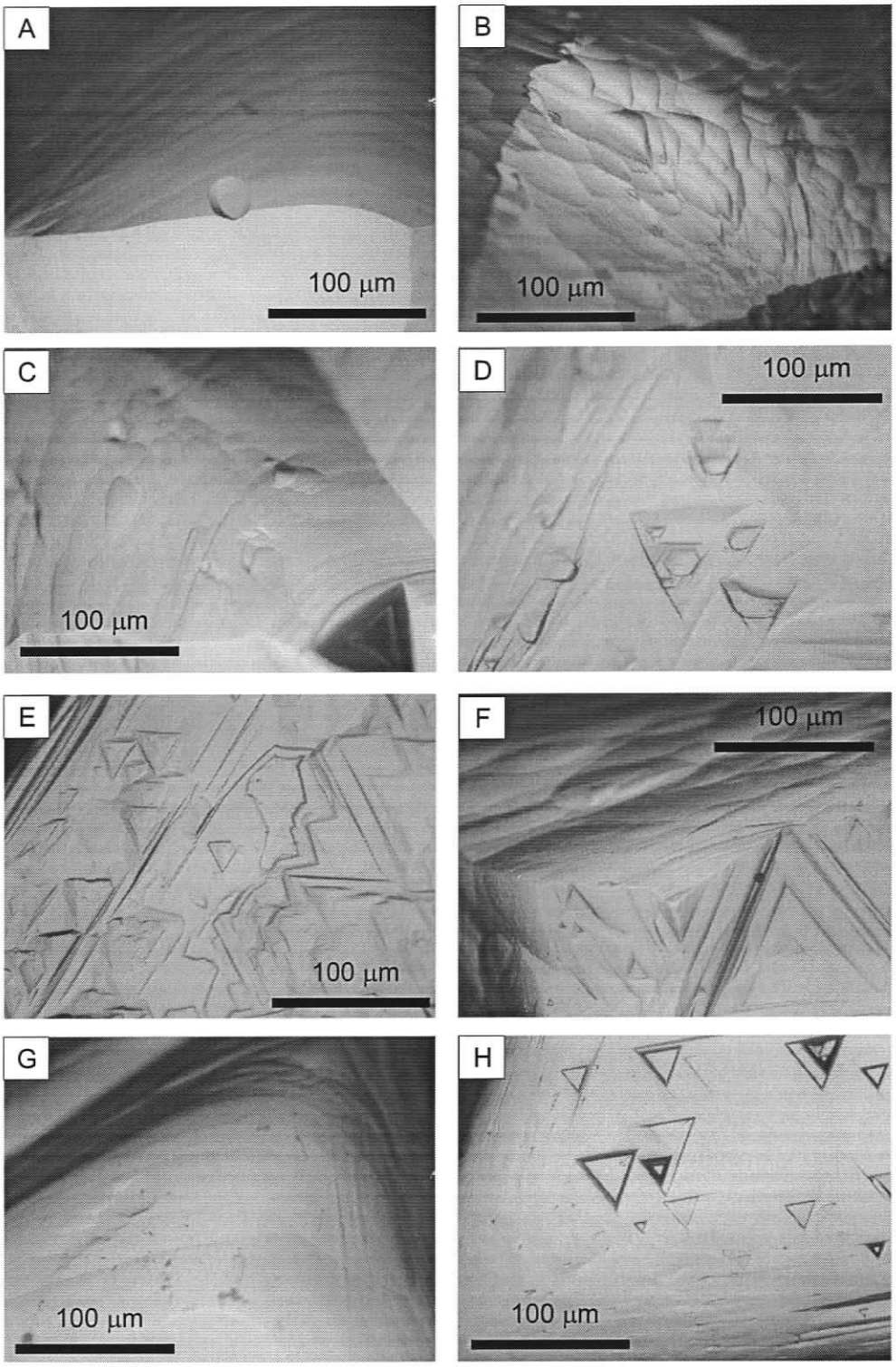

Figure 4.7 Photographs under optical microscope of etch features produced on octahedrons after oxidation in H_2O and CO_2 fluid. The most common features produced only in H_2O fluid: (a) striation and round cavities on THH sides, (c) individual round pyramid-shape hillocks, (h) small pointed holes, (g) deformation lamellae. In CO_2 fluid the main features are: (b) drop-shape hillocks completely covering THH surface, (d) hexagons, (e) etch pits of irregular shape, (f) rough surfaces.

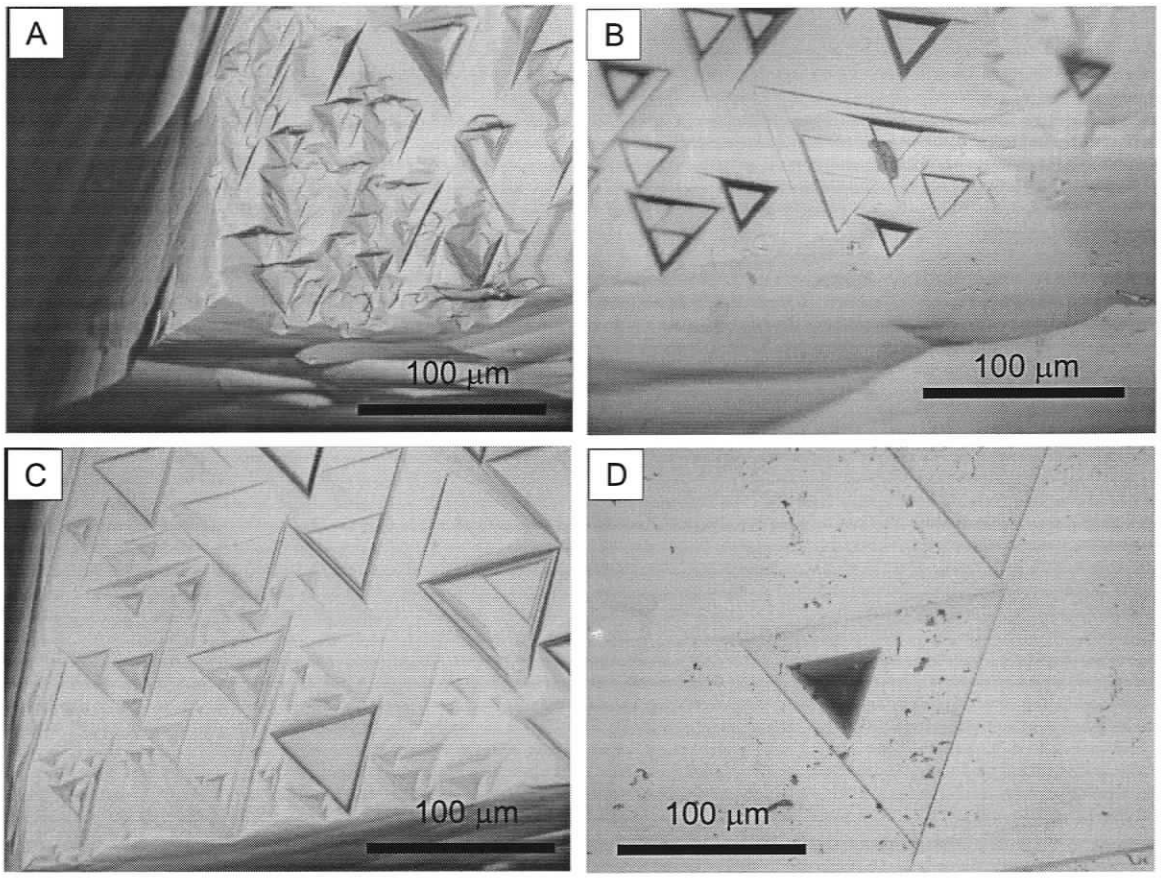

Figure 4.8 Different types of trigons produced in H_2O and CO_2 fluids. Note more complex pattern and many pointed-bottom trigons in CO_2 runs (a,c) and more regular, mainly flat-bottom trigons in H_2O (b,d).

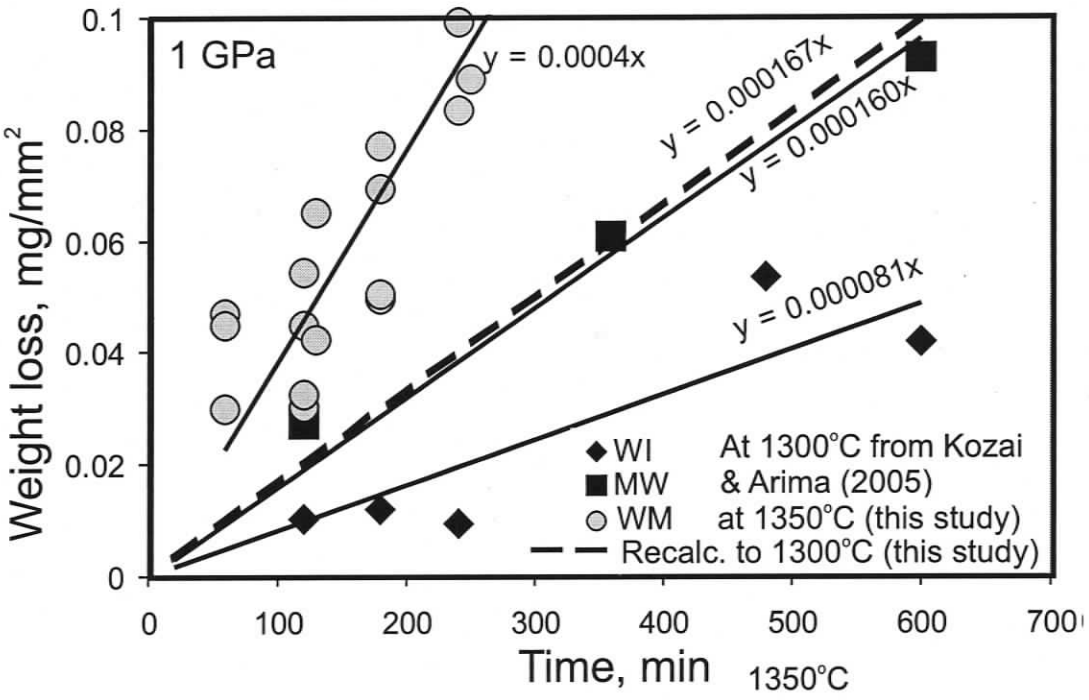

Figure 4.9 Diamond oxidation rates obtained at 1350C, 1 GPa and fO_2 within a log unit above wustite-magnetite (WM) buffer (Table 3) in this study and recalculated to 1300C using the Arrhenius relationship from (Kozai and Arima, 2005) are similar to the data from Kozai and Arima (2005) obtained at 1300C and fO_2 of WM buffer. The similar oxidation rates in CMS-H_2O melt and fluid of H_2O and CO_2 composition (present study) and in the Wesselton kimberlite (Kozai and Arima, 2005) suggest no influence of the melt on the diamond oxidation. All error bars are within the size of the symbol.

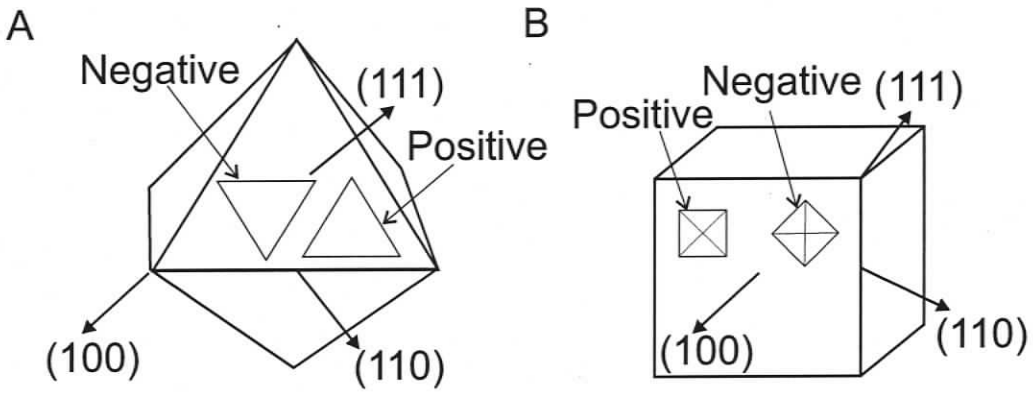

Figure 4.10 Main crystallographic directions of the diamond lattice for octahedron (a) and cubic (b) crystal with positive and negative orientation of etch pits on the (111) and (100) faces shown.

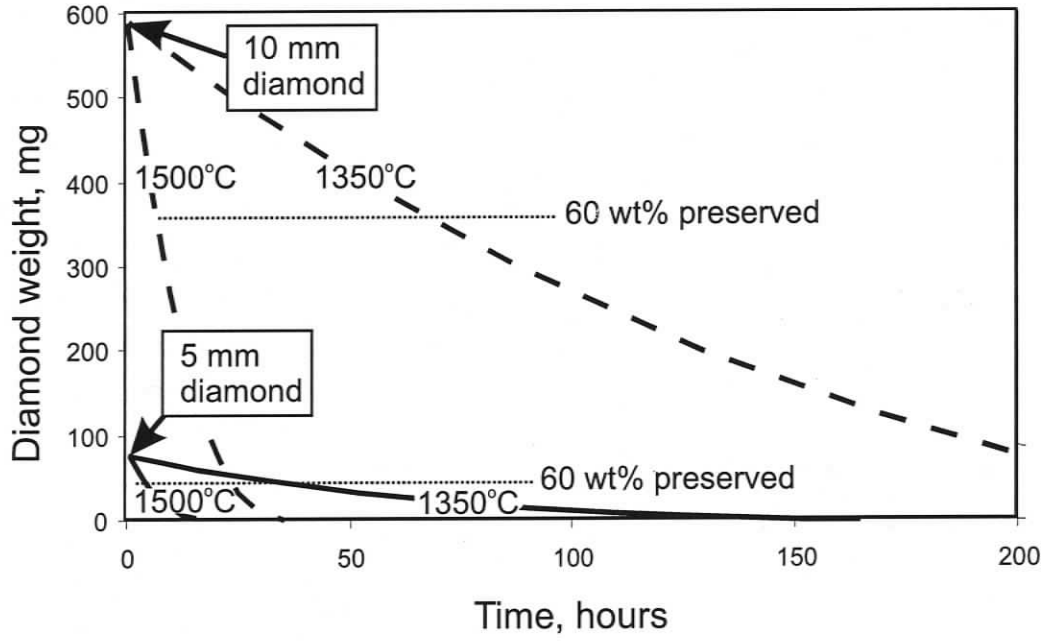

Figure 4.11 Diamond initial weight loss during oxidation at 1350° and 1500°C, 1 GPa and NNO buffer calculated for an octahedron diamond 10 mm long (dotted lines) and 5 mm long (solid lines) by the formula:
Weight $_{time\ 2}$(mg) = Weight $_{time\ 1}$(mg)- Rate (mg/mm^2 hour^{-1}) * Area $_{time\ 1}$(mm^2).
The oxidation rate at 1350°C (0.024 mg/mm^2 *hour^{-1}) is from the present study, at 1500°C (0.247 mg/mm^2 *hour^{-1}) is extrapolated from Kozai and Arima (2005) using Arrhenius relationship. The primary octahedron form is completely converted into secondary THH after 40% of the initial diamond weight loss and the weight correspondent to the 60% of the initial weight for both diamonds is shown.

CHAPTER 5.

CONCLUSIONS

The goal of this research was to address a number of issues related to the evolution and conditions of the kimberlite melts and their effect on the diamond preservation. To achieve this goal, I combined petrographic and mineral chemical studies of fresh kimberlites from the Lac de Gras field, N.W.T., Canada; thermobarometric calculations of crystallization T and fO_2 for these kimberlites; a detailed description of morphology and surface features of over 7000 diamonds recovered from these pipes; and diamond oxidation experiments at high T and P expected during kimberlite emplacement.

The main results of the study are: 1) Determination of crystallization conditions of kimberlite melts (T, fO_2, new data on the composition and behavior of the volatiles); 2) Investigation of the relationship between the conditions of kimberlite melts and the character of resorption in diamond parcels recovered from these kimberlites; 3) Describing the mechanism of diamond interaction with kimberlite magmas and determined the main rate-controlling parameters for diamond oxidation.

5.1. DIAMOND RESORPTION

5.1.1. Mechanism of diamond resorption

Diamond oxidation experiments in this study show that volatile-free or volatile-undersaturated melts produce a layer of surface graphite on the diamond surface and no resorption, whereas melts equilibrated with a free fluid phase and pure H_2O and CO_2 fluids produce resorption commonly observed on natural diamonds. It is, therefore,

proposed that diamond resorption in kimberlite magmas happens by its reaction with the kimberlitic fluid. Diamond reaction with the components of the melt is an energetically less favorable and slower process that is accompanied by the surface graphitization. When a fluid phase is present, the more energetically favorable and faster process of diamond oxidation by the volatile species of the fluid phase produces the resorption features. The majority of previous experimental studies suggested diamond oxidation by interaction with volatiles dissolved in the melt, where H_2O- and CO_2-content of the melt affects the resorption (e.g. Chepurov et al., 1985, Kozai and Arima, 2005). Harris and Vance (1974) recognized that diamonds may interact with the components of the fluid, but kimberlite melt played the major role in this reaction. Rudenko et al. (1979) are the first who showed that diamond does not react with kimberlite melt, but is oxidized by gas or vapor. But their results obtained at 100 KPa and low T differed significantly from those of high T and P processes happened in natural kimberlite magmas. The present study suggestes that at the conditions expected during kimberlite emplacement, diamond oxidation by reaction with the melt is negligible compared to the oxidation by the fluid phase. Only the reaction with the fluid produces the resorption features common for natural diamonds. The results showed similar oxidation rates of diamond in the melt + fluid system and in a pure fluid. They also allowed to determine the main rate-controlling parameters for diamond oxidation in kimberlite magmas.

5.1.2. Rate-controlling parameters

The kinetics of diamond oxidation in kimberlite melts may depend on many factors: T, fO_2 of the melt, H_2O and CO_2 content (e.g. Kozai and Arima, 2005), bulk rock composition of the kimberlite (Rudenko et al., 1979), properties of the diamonds

(Mendelssohn and Milledge, 1995). This work investigated the effect of the different parameters on diamond oxidation rate and clarified their influence on the diamond preservation in kimberlite.

Kimberlite composition may affect diamond oxidation in two ways. Kozai and Arima (2005) proposed that kimberlite melt dissolved diamonds in the form of CO_2. The CO_2 solubility in the melt, then, controls the kinetics of this reaction and itself depends on the composition of the melt. The latter, therefore, influences the rate of diamond oxidation. The present study shows that since the diamonds are not dissolved in the melt, but are oxidized by the fluid, the melt saturation in CO_2 does not slow down the reaction. On the contrary, the presence of free fluid phase is required for the resorption to occur. The alternative explanation for Kozai and Arima (2005) observations is discussed in the Chapter 4 (Discussion section).

Rudenko et al. (1979) found that diamond oxidation rate vary significantly in the presence of some cations (e.g. Na, K) at 100 KPa and low T. Similar diamond oxidation rates in pure fluids and in fluid-oversaturated melt obtained in this work showed that composition of kimberlite melt is not important for the kinetics of diamond oxidation at high T and P expected during kimberlite emplacement. No effect of the fluid composition (H_2O/CO_2 ratio) on the oxidation rate was also found. Diamonds of various colours and nitrogen content and aggregation state used in the present study showed similar oxidation rate. This indicates no influence of the properties of diamonds on the oxidation. This research shows that at the conditions expected for kimberlite emplacement the melt composition, the fluid composition and diamond characteristics do not affect the diamond oxidation rate. The rate must be fully determined by the intensive variables in the system: T, fO_2 and P.

Another goal of this work was to determine if the conditions of kimberlite melts affect the resorption of diamonds in these kimberlite pipes. The increase in the diamond oxidation rate at higher T and fO_2 was observed in many experimental studies (Cull and Meyer, 1986, Evans and Phaal, 1961, Sonin et al., 2000, Kozai and Arima, 2005). The present work for the first time investigated the relationship between T - fO_2 and the character of diamond resorption in natural diamond populations recovered from five kimberlite pipes (Chapter 3). It found higher degree of surface etching on diamonds from the more oxidized kimberlites and higher degree of resorption of diamonds from kimberlites with higher crystallization T. It suggested that the conditions of a kimberlite can notably affect its diamond population.

5.1.3. Kimberlite vs. mantle resorption

Diamonds can get resorbed both during their residence in the mantle source and during ascent in kimberlite. Diamond resorption in the mantle is recorded in diamonds where resorpbed core is surrounded by a rim of new diamond (Taylor et al., 1995, Gurney et al., 2004, and references therein). However, the majority of resorption is commonly believed to occur in kimberlite magmas (Robinson et al., 1989). The relative importance of the two processes is not known. One of the reasons is the absence of a criterion, which could be used to distinguish between the features of the diamond surface resorption produced in the mantle and surface resorption in kimberlite magmas. The present experimental results allowed clarification of the amount of the resorption produced in the mantle compared to resorption during kimberlite emplacement. It also shows how diamond surface provide information on the fluid environment. This information may help to develop a way to distinguish between the products of mantle and kimberlite resorption.

The empirical study of over 7000 diamonds from five kimberlites showed strong correlation between the presence and degree of diamond etching (trigon and square pits, ruts) and fO_2 of kimberlite melts. The relationship between volume resorption (proportion of THH forms relative to octahedrons) and fO_2 of the melt is less clear. At the same time, there is no positive correlation between the surface etching and volume resorption. I suggest that some notable amount of the volume resorption of diamonds happens in the mantle and cannot be fully determined by the properties of the kimberlite system. The surface etching, on the contrary, happens mainly in kimberlite and can be well predicted from the properties of kimberlite magmas. The experimental part of this study confirms that the diamond resorption features are determined by the latest resorption event. Such an event would completely over-write the pre-existing surface features.

Comparison of the diamond oxidation rates experimentally derived in this work and in the study of Kozai and Arima (2005), with the emplacement rates of kimberlite magmas (Kelley and Wartho, 2000, Canil and Fedortchouk, 1999) suggests that the emplacement is too rapid to produce THH diamonds commonly found in kimberlites (Figure 5.1). Some mantle resorption is necessary to explain presence of large THH diamonds in kimberlites.

The empirical and experimental data in this dissertation suggest that the importance of the mantle resorption is comparable to the one caused by kimberlites. Some of the THH diamond morphologies are produced in the mantle, but all the surface resorption features are determined by the kimberlite.

5.1.4. How kimberlite conditions influence diamond population

Both the new results from the study of the natural resorption in Lac de Gras diamonds and experimentally produced resorption features show what can be learned from the conditions of the host kimberlite about the characteristics of diamond population.

Both empirical and experimental approaches confirm that surface etch features are fully determined by the conditions in kimberlite magmas and can be well predicted from geochemistry of a kimberlite. It is important, because the surface resorption can greatly affect quality and yield of diamonds.

On the contrary, the volume resorption partially happens in the mantle and is not fully determined by the conditions of the kimberlites. Nevertheless, highly oxidized kimberlite magmas can have much lower diamond grade than was predicted from the studies of the mantle material. This was observed in the Ranch Lake kimberlite in the present study. Thus, determining of the fO_2 of kimberlite magmas can help to rule out the possibility of significant diamond loss during kimberlite emplacement and explain some of the discrepancies between the diamond grade predicted from the mantle indicator minerals and the real grades.

Finally, diamond shape and the density of etching are influenced by the composition of kimberlitic fluid. Diamonds with the same weight, but different degrees of resorption have different cut and yield, and are therefore priced differently. The extensive etching of diamond surfaces also reduces diamond's quality. The experimental results of this study show that diamond shape depends on the H_2O/CO_2 ratio in the reacting fluid. A diamond oxidized in CO_2 keeps its original octahedron shape better than in H_2O fluid after the same weight loss. Etching, on the contrary, is harsher in CO_2. Such a variation in the degree of resorption and surface etching is present in naturally resorbed diamonds

(Fig. 5.2). Thus, knowing of H_2O/CO_2 ratio in the kimberlitic fluid helps to predict the shape and preservation of the flat faces of the diamonds and, as a result, their quality.

5.2. CRYSTALLIZATION CONDITIONS OF KIMBERLITES

The thermobarometry and experimental results of the present study provided a new data on the conditions, composition and evolution of kimberlite magmas:

1) T and fO_2 were calculated for the phenocryst crystallization; 2) fO_2 change during kimberlite crystallization and its variation between different kimberlites and kimberlite clusters were determined; 3) the new data on the behavior and composition of volatiles in kimberlite magmas were obtained.

5.2.1. Oxidation conditions

Extreme freshness of the Lac de Gras kimberlites allowed application of mineral geothermometers and oxygen barometers to calculate T and fO_2, and provided new data on the oxidation state and fO_2 changes during kimberlite crystallization.

Composition of chromite inclusions in the rims of olivine phenocrysts in hypabyssal and volcaniclastic kimberlites from Leslie, Aaron, Grizzly, Torrie, Panda, Beartooth, Misery and Ranch Lake recorded the conditions at the end of the olivine crystallization and resulted in the maximum values of fO_2 2.2 – 3.1 log units below the nickel – nickel oxide (NNO) buffer. The minimum fO_2*'s* are limited by the iron – wustite (IW) buffer. Thus, kimberlites are relatively reduced melts and their oxidation state is similar to the fO_2 estimates for their mantle source (e.g. Woodland and Peltonen, 1999, McCammon and Kopylova, 2004).

The obtained T – fO_2 data revealed distinctive individual T – fO_2 trends for each kimberlite that showed melt reduction relative to NNO and FMQ buffers during Ol – Sp co-crystallization. The fO_2 evolution with T in these kimberlites is approximately parallel to WM buffer. Some kimberlites, e.g. Grizzly, have two different T – fO_2 trends, that may indicate mixing of different magma batches.

Variations in the oxidation state of kimberlites within one cluster and from different clusters in the Lac de Gras area were studied. The results show that the oxidation state is similar for kimberlites within one cluster (e.g. Northwest cluster: Panda, Beartooth, Leslie), but vary between different clusters (Northwest, Central zone and Southeast clusters). These variations correspond to substantial differences in the diamond populations of these kimberlites and, possibly, reflect differences in their mantle source. Since the three clusters of kimberlites have different emplacement ages (Creaser et al., 2003), the fO_2 of the mantle source might have changed with time or in space.

The ascent path of kimberlites in T – P – fO_2 space is important for diamond preservation. Kimberlite can take diamonds from their stability field to the CO_2 stability field in a number of ways: 1) directly to CO_2 stability field, 2) going through carbonate stability field, 3) through graphite stability field, 4) through both carbonate and then graphite stability field. Undergoing carbonation reaction can be very destructive for diamonds. Extrapolation of the T – fO_2 data obtained in the present study to high T and P shows that diamonds entrained in the Lac de Gras kimberlites avoided carbonation, stayed mainly in the graphite stability field and went into CO_2 stability field just before the eruption. The process of diamond resorption, therefore, mainly took place in the graphite stability field in agreement with the results of Kozai and Arima (2003) experiments.

5.2.2. Crystallization temperatures and primary melt composition

Ol – Sp mineral assemblage provided estimates of crystallization T of kimberlites between 970° and 1070°C (calculated at 1 GPa) at the end of olivine phenocryst crystallization. These are the first kimberlite liquidus T derived from the rock mineralogy and not implied from experiments. These T provided information on the composition of the melt (MgO content) equilibrated with this minerals assemblage. The calculated MgO-content of the melt is somewhere lower than the extrapolated composition of the known primary kimberlite melt examples (Jericho and Wesselton) and may be explained by the influence of volatiles. As a result, the liquidus T calculations indirectly support the extremely high volatile content of kimberlites proposed by many researchers.

Comparison of crystallization T of different kimberlite bodies showed similar T for kimberlites within one cluster and different for the three clusters in the Lac de Gras area. T increases in SE direction and corresponds to the higher degree of diamond resorption and poorer quality of the diamonds in these kimberlites.

5.2.3. Volatiles in kimberlites

The results of the diamond oxidation experiments suggest the presence of a free fluid phase in kimberlite magmas and put constraints on its composition. The resorption features found on natural diamonds require the presence of a free fluid phase in kimberlite magmas at the last stages of the emplacement. In order to produce THH morphology, the diamond must lose about 40% of its initial weight. If the full amount of the resorption were only produced in kimberlite, this would require fluid to be present through almost

whole history of the kimberlite. Large THH diamonds are common, but they might be partially a result of the mantle resorption discussed above. The only diamonds that provide the information about the kimberlite resorption are pseudohemimorphic diamonds that were attached to a xenolith and therefore had only one side exposed to the reaction with kimberlite. As a result, they have THH faces on one half and octahedron faces preserved on the other. Presence of such diamonds among the large size fractions in Lac de Gras diamonds suggest presence of a free fluid phase in kimberlites through the most of their history.

Diamond oxidation in pure H_2O and CO_2 fluids produced completely different surface resorption features. These features compared to the studied Lac de Gras diamonds suggested very high H_2O/CO_2 proportion in the last stage fluid in these kimberlites. If the H_2O/CO_2 ratio of kimberlite fluid is known, this experimental data makes possible to predict the surface features on diamonds and, therefore, to get some estimates of the diamond quality for a particular kimberlite On the other hand, it provides a new tool to determine the composition of the fluid in different kimberlites. Diamond populations from different kimberlites found around the world show a great variety of surface features, and some of them can be possibly explained by the variations in the fluid composition.

5.3. APPLICATIONS AND FURTHER STUDIES

The present study demonstrated that oxidation state of kimberlite melt notably influences character of resorption in natural diamond populations and showed that the kinetics and the character of diamond resorption are mainly determined by T, fO_2, P and fluid composition of a kimberlite. However, to be able to calculate the amount of resorption

caused by kimberlite for the existing models of kimberlite emplacement we need an equation that relates diamond oxidation rate to fO_2. It requires more experimental data on diamond oxidation at variable fO_2 for a range of T to combine with the results of the present study and the data by Kozai and Arima (2005).

This work proposed interaction with the volatile species in the fluid as a mechanism of diamond resorption. What causes the formation of different etch features on the diamond surface is not yet understood. I propose that the reaction rate of different volatile species with the certain diamond faces corresponds to the distance and configuration between the open bonds of the diamond lattice, relative to the size of the reacting molecule. To test this hypothesis and to find the relative oxidation rates for different volatile species in different crystallographic directions of diamond lattice requires etching of various diamond faces in a range of experimental conditions. Such a relationship will help to "read" the evolution of the fluid composition and change of T and fO_2 conditions of the system recorded on the diamonds surfaces.

A new data was obtained on the behavior of volatiles in kimberlites that suggested over-saturation of the melt with volatiles and presence of the free fluid phase through the most of kimberlite history. It also suggested that the surface resorption features on diamonds provide information about H_2O/CO_2 ratio in the fluid that cannot be obtained by other methods. Application of these experimental data to the natural diamond populations recovered from kimberlites can help to improve our understanding of the evolution of volatiles in kimberlite magmas. Presence of "H_2O-characteristic" and "CO_2 characteristic" features in different diamond groups or diamonds from different kimberlite phases can help to constrain evolution of the reacting fluid through the time. Such research can be combined with investigation of other indicators of the fluid composition

in groundmass mineralogy, bulk rock geochemistry, groundmass textures. This may help to predict the quality of the diamonds in a kimberlite pipe.

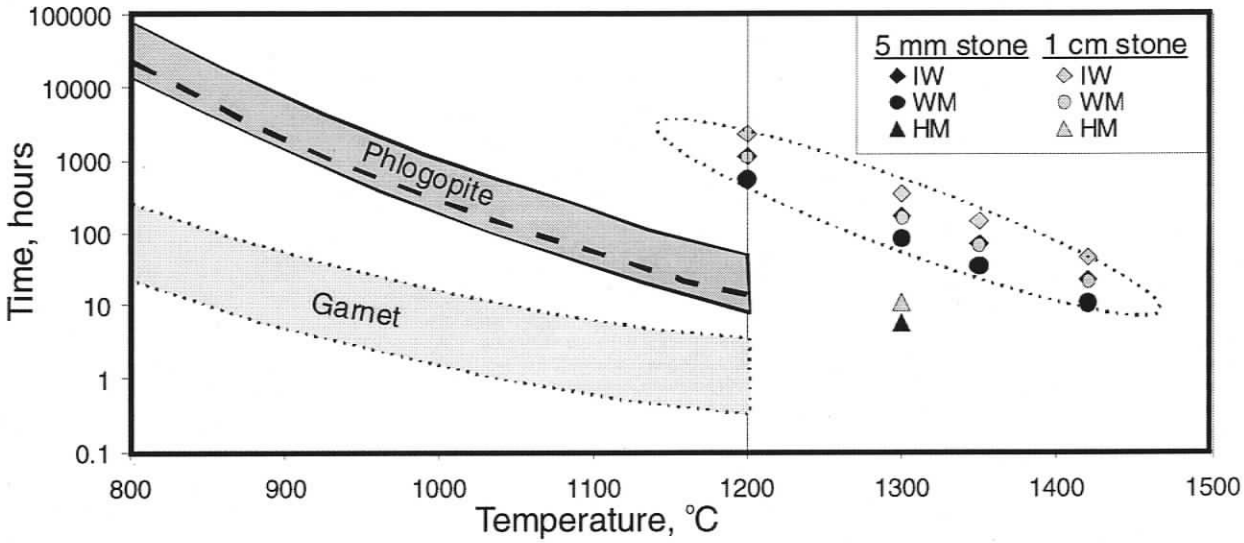

Figure 5.1. Comparison of kimberlite emplacement time with the time required to produce a THH diamond from a primary octahedron (40% of initial weight loss) for 5mm and 1 cm stones at different oxidation conditions (the plot modified from Kelley and Wartho, 2000, and references therein). The data for 1300°C (all three fO_2's) and 1420°C (IW buffer) is from Kozai and Arima (2005), 1350°C at WM is from this study, at 1200°C – extrapolated from the Arrhenius relationship in Kozai and Arima (2005) data, the dotted line is fO_2 of kimberlite melts. The plot shows that the time required to produce THH, that are commonly recovered from kimberlites, is longer than the whole time of kimberlite emplacement even for a 5 mm diamond. This implies a notable diamond resorption in the mantle source. The rates of the two processes converge only at higher fO_2 and T above 1400°C. The fO_2 relative to iron – wustite (IW), wustite – magnetite (WM) and hematite – magnetite (HM) buffers is calculated from Frost (1991).

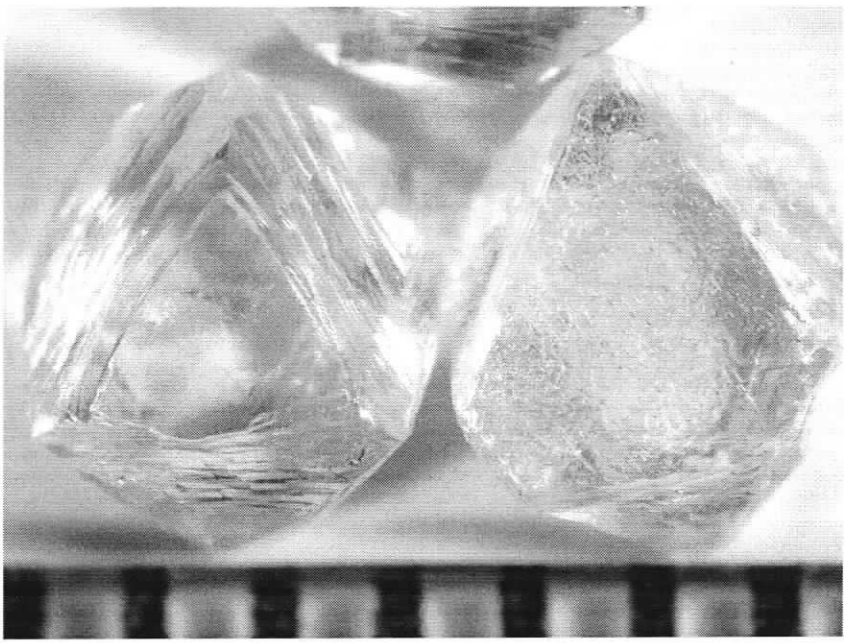

Figure 5.2. Different character of resorption produced in nature. Left stone has lost its original octahedron form, but shows almost no etching on (111) face, whereas the right stone preserved its octahedron shape, but severely etched.

REFERENCES

Afanasiev, V.P., Yefimova, E.S., Zinchuk, N.N., and Koptil, V.I. (2000) Atlas of morphology of diamonds from Russian sources. SPC UIGGM, Russian Academy of Science.

Andersen, D. J., and Lindsley, D. H. (1981) A valid Margules formulation for an asymmetric ternary solution: revision of the olivine-ilmenite thermometer, with applications. Geochimica et Cosmochimica Acta, 45, 847-853.

Andersen, D. J., Bishop, F. C., and Lindsley, D. H. (1991) Internally consistent solution models for Fe-Mg-Mn-Ti oxides: Fe-Mg-Ti oxides and olivine. American Mineralogist, 76, 427-444.

Andersen, D. J., Lindsley, D. H., and Davidson, P. M. (1993) QUILF: a PASCAL program to assess equilibria among Fe- Mg-Ti oxides, pyroxenes, olivine, and quartz. Computers in Geosciences, 19, 1333-1350.

Arima, M. (1998) Experimental study of growth and resorption of diamond in kimberlitic melts at high pressures and temperatures. 7th Internat. Kimberlite Conference, Extended Abstracts, p. 32-34, Cape Town.

Arima, M., Nakayama, K., Akaishi, M., Yamaoka, S., and Kanda, H. (1993) Crystallization of diamond from a silicate melt of kimberlite composition in high-pressure and high-temperature experiments. Geology, 21, 968-970.

Ballhaus, C., Berry, R. F., and Green, D. H. (1991) High pressure experimental calibration of the olivine-orthopyroxene-spinel oxygen geobarometer: Implications for the oxidation state of the upper mantle. Contributions to Mineralogy and Petrology, 107, 27-40.

Bartoshinskiy, Z.V. (1983) Mineralogical classification of natural diamonds. Mineralogicheskiy Zhurnal, 5(5), 84-93 (in Russian).

Beattie, P. (1994) Systematics and energetics of trace element partitioning between olivine and silicate melts: implications for the nature of mineral/melt partitioning. Chemical Geology, 117, 57-71.

Berg, G. W., and Carlson, J. A. (1998) The Leslie kimberlite pipe of Lac de Gras, Northwest Territories, Canada. In: 7th Internat. Kimberlite Conference, pp. 81-83, Cape Town.

Boyd, F. R., and Canil, D. (1997) Peridotite xenoliths from the Slave Craton, Northwest Territories. In: Seventh annual V. M. Goldschmidt conference, pp. 34-35, Lunar and Planetary Institute. Houston, TX, United States.

Brearley, M., and Scarfe, C.M. (1986) Dissolution rates of upper mantle minerals in an alkali basalt melt at high pressure: an experimental study and implications for ultramafic xenolith survival. Journal of Petrology, 27, 1157-1182.

Canil, D., and Scarfe, C. M. (1990) Phase relations in peridotite + CO_2 systems to 12 GPa: implications for the origin of kimberlite and carbonate stability in the Earth's upper mantle. Journal of Geophysical Research, 95, 15805-15816.

Canil, D., and Fedortchouk, Y. (1999) Garnet dissolution and the emplacement of kimberlites. Earth and Planetary Science Letters,167, 227-237.

Canil, D., and Fedortchouk, Y. (2001) Olivine-liquid partitioning of vanadium and other trace elements, with applications to modern and ancient picrites. The Canadian Mineralogist, 39, 319-330.

Carmichael, I. S. E. (1991) The redox states of basic and silicic magmas: a reflection of their source regions? Contributions to Mineralogy and Petrology, 106, 129-141.

Chepurov, A.I., Khokhryakov, A.F., Sonin, V.M., and Pal'yanov, Y.N. (1985) Forms of dissolution of diamond crystals in silicate melts at high pressure. Doklady Academii Nauk SSSR, 285(1), 212-216. (in Russian)

Clement, C. R. (1982) A comparative geological study of some major kimberlite pipes in the Northern Cape and Orange Free State. Unpub. PhD Thesis Thesis, University of Cape Town.

Clayton, R. N., and Toshiko, K. M. (1983) Oxygen isotopes in eucrites, shergottites, nakhlites, and chassignites. Earth and Planetary Science Letters.,62, 1-6.

Cookenboo H (1996) Ranch Lake kimberlite in the Central Slave Craton: the mantle sample. The Gangue, 52, 12-13

Creaser RA, Grütter H, Carlson J, and Crawford B (2004) Macrocrystal phlogopite Rb–Sr dates for the Ekati property kimberlites, Slave Province, Canada: evidence for multiple intrusive episodes in the Paleocene and Eocene. Lithos, 76, 399-414

Cull, F.A., and Meyer, H.O.A. (1986) Oxidation of diamond at high temperature and 1 atm total pressure with controlled oxygen fugacity. 4th International Kimberlite Conference, p. 377-379. Geological Soc of Australia, Perth, Australia.

Dalton, J. A., and Presnall, D. C. (1998) The continuum of primary carbonatitic-kimberlitic melt compositions in equilibrium with lherzolite: data from the system CaO-MgO-Al_2O_3-SiO_2-CO_2 at 6 GPa. Journal of Petrology, 39(11 & 12), 1953-1964.

Davies, G., and Evans, T. (1972) Graphitization of diamond at zero pressure and at a high pressure. Proc. R. Soc. Lond. A., 328, 413-427.

Davis, W. J., and Kjarsgaard, B. A. (1997) A Rb-Sr Isochron age for kimberlite from the recently discovered Lac de Gras Field, Slave Province, Northwest Canada. Journal of Geology, 105, 503-509.

Droop, G. T. R. (1987) A general equation for estimating Fe^{3+} concentrations in ferromagnesian silicates and oxides from microprobe analyses, using stoichiometric criteria. Mineralogical Magazine, 51, 431-435.

Edgar, A. D., Arima, M., Baldwin, D. K., Bell, D. R., Shee, S. R., Skinner, E. M. W., and Walker, E. C. (1988) High pressure - high temperature melting experiments on a SiO_2-poor, CaO-rich aphanitic kimberlite from the Wesselton mine, Kimberley, South Africa. American Mineralogist, 73, 524-533.

Edgar, A.D., and Charbonneau, H.E. (1993) Melting experiments on a SiO2-poor, CaO-rich aphanitic kimberlite from 5-10 GPa and their bearing on source of kimberlite magmas. Americam Mineralogist, 78, 132-142.

Evans, T., and Phaal, C. (1961) The kinetics of the diamond - oxygen reaction. Conference on Carbon, 5 PT.1, p. 147-153. Pergamon Press, New York.

Evans, T., and Harris, J.W. (1989) Nitrogen aggregation, inclusion equilibration temperatures and the age of diamonds. In J.R.e. al., Ed. Kimberlite and Related Rocks, 2, p. 1001-1006.

Fedortchouk Y, Canil D (2004) Intensive variables in kimberlite magmas, Lac de Gras, Canada and implications for diamond survival. Journal of Petrology, 45, 1725-1745

Fedortchouk, Y., Canil, D., and Carlson, J.A. (2005) Dissolution forms in Lac de Gras diamonds and their relationship to the temperature and redox state of kimberlite magma. Contributions to Mineralogy and Petrology, 150, 54-69.

Fersmann, A., and Goldschmidt, V. (1911) Der Diamant: Eine Studie. 274 p. Carl Winter's Universitatbuchhandlung, Heidelberg.

Fipke, C. E., Gurney, J. J., and Moore, R. O. (1995) Diamond exploration techniques emphasising indicator mineral geochemistry and Canadian examples. Geological Survey of Canada Bulletin, 423, 1-86.

Foley, S. F. (1990) A review and assessment of experiments on kimberlites, lamproites and lamprophyres as a guide to their origin. Earth Planet. Sci., 99, 57-80.

Ford, C. E., Russell, D. G., Craven, J. A., and Fisk, M. R. (1983) Olivine-liquid equilibria: temperature, pressure and composition dependence of the crystal/liquid cation partition coefficients for Mg, Fe^{2+}, Ca and Mn. Journal of Petrology, 24(3), 256-265.

Frost B (1991) Introduction to oxygen fugacity and its petrologic importance. In: Lindsley D H (ed) Oxide minerals: petrologic and magnetic significance, Rev Mineralogy 25. Min Soc America, pp. 1-9

Frost, D. J., and Wood, B. J. (1997) Experimental measurments of the fugacity of CO_2 and graphite / diamond stability from 35 to 77 kbar at 925° to 1650°C. Geochimica et Cosmochimica Acta, 61(8), 1565-1574.

Fung, A. T. (1998) Petrochemistry of upper mantle eclogites from the Grizzly, Leslie, Pigeon and Sable kimberlites in the Slave Province, Canada. In: 7th Internat. Kimberlite Conference, pp. 230-232, Cape Town.

Ghiorso, M. S., and Sack, R. O. (1995) Chemical Mass Transfer in Magmatic Processes. IV. A Revised and Internally Consistent Thermodynamic Model for the Interpolation and Extrapolation of Liquid-Solid Equilibria in Magmatic Systems at Elevated Temperatures and Pressures. Contributions to Mineralogy and Petrology, 119, 197-212.

Girnis, A. V., Brey, G. P., and Ryabchikov, I. D. (1995) Origin of Group 1A kimberlites; fluid-saturated melting experiments at 45-55 kbar. Earth and Planetary Science Letters, 134(3-4), 283-296.

Gudfinnsson, G.H., and Presnall, D.C. (2005) Continuous gradations among primary carbonatic. kimberlitic, melilititic, basaltic, picritic, and komatiitic melts in equilibrium with garnet lherzolite at 3-8 GPa. Journal of Petrology, 46(8), 1645-1659.

Gurney, J.J. (1986) Diamonds. Kimberlites and Related Rocks, 2, p. 935-965.

Gurney, J.J., Hildebrand, P.R., Carlson, J.A., Fedortchouk, Y., and Dyck, D.R. (2004) The morphological characteristics of diamonds from the Ekati property, Northwest Territories, Canada. Lithos, 77, 21-38.

Haggerty, S.E. (1986) Diamond genesis in a multiply-constrained model. Nature, 320, 34-38.

Haggerty, S.E. (1999) A diamond trilogy: Superplumes, Supercontinents, and Supernovae, Science, 285 (6), 851-860.

Harris J.W. Vance E.R. (1974) Studies of the reaction between diamond and heated kimberlite. Contirbutions to Mineralogy and Petrology, 47, 237-244

Harris, J. W. (1987) Recent physical, chemical, and isotopic research of diamond. In: Mantle xenoliths (ed Nixon, P. H.), pp. 477-500, John Wiley and Sons LTd, Chichester.

Hayman, P.C., Kopylova, M.G., and Kaminsky, F.V. (2005) Lower mantle diamonds from Rio Soriso (Juina area, Mato Grosso, Brazil). Contributions to Mineralogy and Petrology, 149, 430-445.

Hays, J.F. (1966a) Stability and properties of the synthetic pyroxene CaAl2SiO6. American Mineralogist, 51, 1524-1529.

Hays, J.F. (1966b) Lime-Alumina-Silica. Carnegie Institution Yearbook, 65, 234-239.

Holland, T.J.B.,, and Powell R. (1990) An enlarged and updated internally consistent thermodynamic dataset with uncertainties and correlations: the system K_2O-Na_2O-CaO-MgO-MnO-FeO-Fe_2O_3-Al_2O_3-TiO_2-SiO_2-C-H-O_2. Journal of Metamorphic Geology, 8, 89-124.

Holland, T.J.B.,, and Powell R. (1998) An internally consistent thermodynamic data set for phases of petrological interest. Journal of Metamorphic Geology, 16, 309-343.

Holloway, J.R., and Blank, J.G. (1994) Application of Experimental Results to C-O-H Species in Natural Melts. In M.R. Carrol, and J.R. Holloway, Eds. Volatiles in Magmas, 30, p. 187-230. Min Soc of Am.

Ilupin, I. P., and Lutz, B. G. (1971) The chemical composition of kimberlite and questions on the origin of kimberlite magmas. Sovetskaya Geologiya, 6, 61-73.

Kelley, S.P., and Wartho, J.-A. (2000) Rapid kimberlite ascent and the significance of Ar-Ar ages in xenolith phlogopites. Science, 289, 609-611.

Kennedy, C. S., and Kennedy, G. C. (1976) The equilibrium boundary between graphite and diamond. Journal of Geophysical Research,, 81(14), 2467 - 2470.

Keppler, H. (2003) Water solubility in carbonatite melts. American Mineralogist, 88, 1822-1824.

Khokhryakov AF , Palyanov YN (1990) Morphology of diamond crystals dissolved in water-containing silicate melts. Mineralogicheskiy Zhurnal, 12, 14-23

Kirkley, M. B., Kolebaba, M. R., Carlson, J. A., Gonzales, A. M., Dyck, D. R., and Dierker, C. (1998) Kimberlite emplacement processes interpreted from Lac de Gras examples. In: 7th Internat. Kimberlite Conference, pp. 429-431, Cape Town.

Kirkley, M. B., Smith, H. S., and Gurney, J. J. (1989) Kimberlite carbonates - a carbon and oxygen stable isotope study. In: Kimberlites and Related Rocks, pp. 264-281, GSA.

Kopylova, M.G., and McCammon C. (2003) Composition and the Redox State of the Slave Peridotitic Mantle, In: 8th Internat. Kimberlite Conference, Victoria.

Kozai, Y., and Arima, M. (2003) Diamond dissolution in kimberlite and lamproite melts at deep crustal conditions. Abstracts of 8th International Kimberlite Conference.

Kozai, Y., and Arima, M. (2005) Experimental study on diamond dissolution in kimberliteic and lamproitic melts at 1300-1420 C and 1 GPa with controlled oxygen partial pressure. American Mineralogist, 90, 1759-1766.

Kress, V. C., and Carmichael, I. S. E. (1988) Stoichiometry of the iron-oxidation reaction in silicate melts. Am. Mineral., 73, 1267-1274.

Langmiur, C. H., Klein, E. M., and Plank, T. (1992) Petrological systematics of mid-ocean ridge basalts: constraints on melt generation beneath ocean ridges. In: Mantle flow and melt generation at mid-ocean ridges (eds Phipps Morgan, J., Blackman, D. K., and Sinton, J. M.), pp. 183-280, American Geophysical Union.

Larsen, L. M., and Pedersen, A. K. (2000) Processes in high-Mg, high-T magmas; evidence from olivine, chromite and glass in Palaeogene picrites from West Greenland. Journal of Petrology, 41(7), 1071-1098.

Lockhart G, Grutter H, Carlson JA (2004) Temporal, geomagnetic and related attributes of kimberlite magmatism at Ekati, Northwest Territories, Canada. Lithos, 77, 665-682

MacKenzie, J. M., and Canil, D. (1999) Composition and thermal evolution of cratonic mantle beneath the central Archean Slave Province, NWT, Canada. Contributions to Mineralogy and Petrology, 134, 313-324.

McCammon, C. A., Griffin, W. L., Shee, S. R., and O'Neill, H. S. C. (2001) Oxidation during metasomatism in ultramafic xenoliths from the Wesselton kimberlite, South Africa: implications for the survival of diamond. Contributions to Mineralogy and Petrology, 141, 287-296.

McCammon, C. (2001) Deep diamond mysteries. Science, 293, 813-814.

McCammon C , Kopylova MG (2004) A redox profile of the Slave mantle and oxygen fugacity control in the cratonic mantle. Contributions to Mineralogy and Petrology, 148, 55-68

McCrea, J.M. (1950) On the isotope chemistry pf carbonates and a paleotemperature scale. Journal of Chemical Physics., 18, 849-857.

McDade, P., Wood, B.J., VanWestrenen, W., Brooker, R., Gudmundsson, G., Soulard, H., Najorka, J., and Blundy, J. (2002) Pressure corrections for a selection of piston-cylinder cell assemblies. Mineralogical Magazine, 66(6), 1021-1028.

Mendelssohn, M.J., and Milledge, H.J. (1995) Morphological Characteristics of Diamond Populations in relation to Temperature-Dependent Growth and Dissolution Rates. International Geology Review, 37, 285-312.

Meyer, H.O.A. (1985) Genesis of diamond: a mantle saga. American Mineralogist, 70, 344-355.

Mitchell, R. H. (1973) Composition of olivine, silica activity and oxygen fugacity in kimberlite. Lithos, 6, 65-81.

Mitchell, R.H. (1986) Kimberlites: Mineralogy, geochemistry, and petrology. Plenum Press, New York.

Mitchell, R.H. (1995) Kimberlites, orangeites, and related rocks. Plenum Press, New York.

Mitchell, R.H. (1996) Classification of undersaturated and related alkaline rocks. In R.H. Mitchell, Ed. Undersaturated alkaline rocks: Mineralogy, petrogenesis, and economic potencial, 24, p. 1-22, Winnipeg, Manitoba.

Mitchell, R.H. (2004) Experimental studies at 5-12 GPa of the Ondermatjie hypabyssal kimberlite. Lithos, 76, 551-564.

Nassichuk, W. W., and McIntyre, D. J. (1995) Cretaceous and Tertiary fossils discovered in kimberlites at Lac de Gras in the Slave Province, Northwest Territories. In: Interior Plains and Arctic Canada--Plaines interieures et region arctique du Canada, pp. 109-114, Geological Survey of Canada. Ottawa, ON, Canada.

O'Neill, H., and Wall, V. J. (1987) The olivine-orthopyroxene-spinel oxygen geobarometer, the nickel precipitation curve, and the oxygen fugacity of the Earth's upper mantle. Journal of Petrology, 28, 1169-1191.

Orr, P., and Luth, R. W. (2000) Petrology and oxygen-isotope geochemistry of the Yamba Lake kimberlite rocks, N.W.T. Canadian Journal of Earth Sciences, 37, 1053-1071.

Pal'yanov, Y.N., Khokhryakov, A.F., Borzdov, Y.M., and Sokol, A.G. (1995) Diamond morphology in growth and dissolution processes. Extenden Abstracts 6th International Kimberlite Conference, 415-417.

Pell, J.A. (1997) Kimberlites in the Slave Craton, Northwest Territories, Canada. Geoscience Canada, 24, 77-90.

Pouchou, J. L., and Pichoir, F. (1985) PAP $\varphi(\rho Z)$ procedure for improved quantitative microanalysis. Microbeam Analysis, 104-106.

Price, S.E., Russell, J.K., and Kopylova, M.G. (2000) Primitive magma from the Jericho pipe, NWT, Canada: constraints on primary kimberlite melt chemistry. Journal of Petrology, 41(6), 789-808.

Richardson, S.H., Gurney, J.J., Erlank, A.J., and Harris, J.W. (1984) Origin of diamonds in old enriched mantle. Nature, 310, 198-202.

Richardson, S.H., Shirey, S.B., Harris, J.W., and Carlson, R.W. (2001) Archean subduction recorded by Re-Os isotopes in eclogitic sulfide inclusions in Kimberley diamonds. Earth and Planetary Science Letters, 191, 257-266.

Ringwood, A.E., Kesson, S.E., Hibberson, W.O., and Ware, N. (1992) Origin of kimberlites and related magmas. Earth Planet. Sci. Lett., 113, 521-538.

Robinson, D.N., Scott, J.A., Neikerk, A.V., and Anderson, V.G. (1989) The sequence of events reflected in the diamonds of some southern African kimberlites. Kimberlites and related rocks, 2, No 14, p. 990-1000.

Roeder, P. L., and Emslie, R. F. (1970) Olivine-liquid equilibrium. Contributions to Mineralogy and Petrology, 29, 275-289.

Roex, A.P.L., Bell, D.R., and Davies, P. (2003) Petrogenesis of group I kimberlites from Kimberley, South Africa: evidence from bulk-rock geochemistry. Journal of Petrology, 44(12), 2261-2286.

Rudenko, A.P., Kulakova, I.I., and Shturman, V.L. (1979) Oxidation of natural diamond. Novye dannye o mineralogii SSSR, p. 105-125. Academiya Nauk SSSR, Fersman Mineralogical Museum, Moscow. (in Russian)

Scott Smith, B. H. S. (1992) Kimberlites and lamproites. Exploration Mining Geology, 1(4), 371-381.

Scott Smith, B.H. (1996) Kimberlites. In M. R.H., Ed. Undersaturated alkaline rocks: Mineralogy, petrogenesis, and economic potencial, 217-244.

Scowen, P. A. H., Roeder, P. L., and Helz, R. T. (1991) Reequilibration of chromite within Kilauea Iki lava lake, Hawaii. Contributions to Mineralogy and Petrology , 107, 8-20.

Shee, S. R. (1984) The oxide minerals of the Wesselton mine kimberlite, Kimberly, South Africa. Kimberlites and related rocks, 1, 59-73.

Shee, S. R. (1986) The petrogenesis of the Wesselton mine kimberlites, Kimberley, South Africa, PhD Thesis, University of Cape Town, Cape Town.

Sheppard, S. M. F., and Dawson, J. B. (1975) Hydrogen, carbon and oxygen isotope studies of megacryst and matrix minerals from Lesothan and South African kimberlites. Physycs and Chemistry of the Earth, 9, 747-763.

Shimizu, N., and Sobolev, N.V. (1995) Young peridotitic diamonds from the Mir kimberlite pipe. Nature, 375, 394-397.

Simkin, T., and Smith, J. V. (1970) Minor-element distribution in olivine. Journal of Geology, 78(3), 304-325.

Smith, C.B., Gurney, J.J., Skinner, E.M.W., Clement, C.R., and Ebrahim, N. (1985) Geochemical character of Southern African kimberlites: a new approach based on isotopic constraints. Trans. Geol. Soc. S. Afr., 88, 267-280.

Sonin, V.M., Zhimulev, Y.I., and Afanas'ev, V.P. (1997) Surface graphitization effect on diamond crystal morphology. Otechestvennaya Geologiya(10), 33-37. (in Russian)

Sonin, V. M., Zhimulev, Ye. I., Fedorov, I. I., and Osorgin, N. Yu. (1997) Etching of diamond crystals in silicate melt in the presence of aqueous solution under high P-T conditions. Geokhimiya. 4, 451-455.

Sonin, V.M., Fedorov, I.I., Pokhilenko, L.N., and Pokhilenko, N.P. (2000) Diamond oxidation rate as related to oxygen fugacity. Geology of Ore Deposits, 42(6), 496-502.

Sonin, V.M., Zhimulev, E.I., Afanas'ev, V.P., and Chepurov, A.I. (2002) Genetic aspects of the diamond merphology. Geology of Ore Deposits, 44(4), 291-299.

Sugawara, T. (2000) Empirical relationships between temperature, pressure, and MgO content in olivine and pyroxene saturated liquid. Journal of geophysical research, 105(B4), 8457-8472.

Sunagawa I (1984) Morphology of natural and synthetic diamond crystals. In Sunagawa (ed.) Material Science of the Earth's Interior, p. 303-330.

Taylor, W.R., Bulanova, G., and Milledge, H.J. (1995) Quantitative nitrogen aggregation study of some Yakutian diamonds: constraints on the growth, thermal, and deformation history of peridotitic and eclogitic diamonds. 6th International Kimberlite Conference, Extended Abstracts, p. 608-610, Novosibirsk.

Urusovskaya AA , Orlov YL (1964) Nature of plastic deformation of diamond crystals. Doklady Akademii Nauk SSSR, 154, 112-115

Watson, E.B. (1987) Diffusion and solubility of C in Pt. American Mineralogist, 72, 487-490.

Watson, E.B., Wark, D.A., Price, J.D., and Van Orman, J.A. (2002) Mapping the thermal structure of solid-media pressure assemblies. Contributions to Mineralogy and Petrology, 142, 640-652.

Ward, B. C., Kjarsgaard, I. M., Dredge, L. A., Kerr, D. E., and Stirling, J. A. R. (1995) Distribution and chemistry of kimberlite indicator minerals, Lac de Gras map area (76D), Northwest Territories. GSC, Open File 3079, 161 p.

Wood, B. J., and Virgo, D. (1989) Upper mantle oxidation state: Ferric iron contents of lherzolite spinel by 57Fe Mössbauer spectroscopy and resultant oxygen fugacities. Geochimica et Cosmochimica Acta, 53, 1277-1291.

Woodland, A. B., and Peltonen, P. (1999) Ferric iron contents of garnet and clinopyroxene and estimated oxygen fugacities of peridotite xenoliths from the Eastern Finland kimberlite province. In: 7th International Kimberlite Conference, pp. 904-911, Cape Town.

Yamaoka S, Kanda H, Setaka N (1980) Etching of diamond octahedrons at high temperatures and pressures with controlled oxygen partial pressure. Journal of Matematical Sciences, 332-336

Zhao, D., Essene, E. J., and Zhang, Y. (1999) An oxygen barometer for rutile-ilmenite assemblages: oxidation state of metasomatic agents in the mantle. Earth and Planetary Science Letters, 166, 127-137.

Zhimulev, E.I., Sonin, V.M., and Chepurov, A.I. (2002) Formation of diamond crystals with faces protruding due to etching. Zapiski Vserossiyskogo Mineralogicheskogo Obshestva, 131(1), 111-113. (in Russian)

APPENDIX I

TableAI. Analyses of kimberlite olivine from the Leslie, Aaron, Grizzly ans Torrie pipes. In the zoned phenocrysts analyses of cores (c) and margins (m) are present.

NN	Sample	MgO	Al2O3	SiO2	CaO	TiO2	Cr2O3	MnO	FeO	NiO	Total	Fo-no
Leslie Pipe												
1	LS1-a-m	50.0	0.01	40.7	0.04	na	0.03	0.12	8.41	0.37	99.7	91.4
2	LS1-a-c	49.1	0.00	40.5	0.04	na	0.00	0.10	9.88	0.27	99.9	89.9
3	LS1-b-c	46.8	0.00	39.9	0.02	na	0.01	0.18	12.88	0.35	100.1	86.6
4	LS1-b-c	49.8	0.00	40.7	0.07	na	0.08	0.13	8.27	0.14	99.2	91.5
5	LS1-b	46.6	0.01	40.0	0.02	na	0.03	0.18	12.90	0.36	100.1	86.6
6	LS1-b-sm	50.1	0.00	40.5	0.05	na	0.07	0.10	8.00	0.37	99.2	91.8
7	LS1-c1-c	51.4	0.02	40.8	0.01	na	0.01	0.06	6.96	0.34	99.6	92.9
8	LS1-c1-m	50.6	0.01	40.9	0.06	na	0.07	0.11	8.10	0.18	100.1	91.8
9	LS1-c2-c	49.5	0.00	40.3	0.03	na	0.00	0.12	9.20	0.33	99.4	90.6
10	LS1-c2-m	51.0	0.00	40.7	0.06	na	0.00	0.13	8.38	0.14	100.4	91.6
11	LS1-d-c	51.5	0.00	40.9	0.01	na	0.00	0.09	7.08	0.36	99.9	92.8
12	LS1-d-m	50.0	0.01	40.8	0.08	na	0.03	0.13	8.28	0.18	99.5	91.5
13	LS1-e-c	50.2	0.00	40.9	0.06	na	0.04	0.09	8.30	0.38	100.0	91.5
14	LS1-f-c	48.5	0.00	40.5	0.04	na	0.04	0.12	10.29	0.23	99.7	89.4
15	LS1-f-m	50.1	0.00	40.8	0.10	na	0.01	0.12	8.25	0.14	99.5	91.6
16	LS1-g1-c	49.9	0.01	40.5	0.05	na	0.08	0.13	8.60	0.36	99.6	91.2
17	LS1-g2-m	47.7	0.11	42.5	0.13	na	0.16	0.13	7.86	0.33	98.9	91.5
18	LS1-g2-c	49.9	0.00	40.6	0.06	na	0.05	0.09	8.65	0.32	99.7	91.1
19	LS1-h-c	51.3	0.00	40.9	0.01	na	0.04	0.10	6.83	0.35	99.5	93.0
20	LS1-h-m	50.4	0.00	41.3	0.07	na	0.05	0.08	8.17	0.17	100.2	91.7
21	LS1-i-c	50.9	0.00	40.7	0.00	na	0.00	0.06	6.40	0.33	98.4	93.4
22	LS1-i-m	50.2	0.00	40.6	0.05	na	0.03	0.11	8.27	0.13	99.4	91.5
23	LS2-n-m*	50.9	0.02	40.5	0.05	0.044	0.02	0.10	8.44	0.36	100.4	91.5
24	LS2-h-3*	49.8	0.00	41.1	0.05	0.009	0.12	0.08	8.18	0.33	99.7	91.6
25	LS2-m-1*	50.0	0.02	41.5	0.08	0.004	0.08	0.13	8.10	0.13	100.1	91.7
26	LS2-m-2*	50.0	0.02	41.5	0.08	0.004	0.08	0.13	8.10	0.13	100.1	91.7
27	LS2-g1-c	50.7	0.02	40.9	0.06	0.014	0.11	0.12	8.50	0.16	100.5	91.4
28	LS2-a1-c	51.0	0.01	40.9	0.02	na	0.00	0.07	7.12	0.38	99.4	92.7
29	LS2-a1-m	49.9	0.03	40.8	0.04	na	0.05	0.12	8.26	0.14	99.3	91.5
30	LS2-a2-c	44.4	0.02	39.2	0.04	na	0.02	0.17	15.53	0.28	99.7	83.6
31	LS2-a2-m	49.4	0.01	40.2	0.05	na	0.04	0.13	8.37	0.14	98.4	91.3
32	LS2-a3-c	48.7	0.00	40.6	0.02	na	0.02	0.10	9.39	0.29	99.1	90.2
33	LS2-a4-m	49.3	0.00	40.4	0.03	na	0.06	0.12	8.25	0.39	98.5	91.4
34	LS2-b-m	49.6	0.00	40.3	0.06	na	0.12	0.10	8.14	0.19	98.5	91.6
35	LS2-b-c	50.4	0.00	40.9	0.02	na	0.02	0.09	7.16	0.35	98.9	92.6
36	LS2-c-c	47.9	0.00	39.9	0.24	na	0.03	0.12	9.90	0.25	98.4	89.6
37	LS2-c-m	49.3	0.00	40.8	0.05	na	0.13	0.11	8.17	0.18	98.7	91.5
38	LS2-d	49.4	0.01	40.9	0.05	na	0.05	0.10	8.34	0.39	99.3	91.4
39	LS2-e1-c	49.3	0.01	40.5	0.02	na	0.04	0.10	8.26	0.38	98.7	91.4
40	LS2-e2-c	49.5	0.00	40.6	0.03	na	0.00	0.12	8.64	0.40	99.2	91.1
41	LS2-e3	49.6	0.01	40.4	0.08	na	0.05	0.12	8.18	0.29	98.7	91.5
42	LS2-e4-c	50.7	0.01	40.7	0.01	na	0.02	0.07	6.87	0.38	98.8	92.9
43	LS2-e4-m	50.0	0.01	40.6	0.06	na	0.04	0.11	8.19	0.18	99.1	91.6
44	LS2-f-c	49.6	0.01	41.1	0.02	na	0.01	0.10	8.22	0.35	99.4	91.5
45	LS2-g-c	49.8	0.00	40.7	0.04	na	0.02	0.12	8.10	0.34	99.1	91.6
46	LS2-h-c	50.2	0.00	40.9	0.04	na	0.00	0.12	7.71	0.31	99.2	92.1
47	LS2-n-c	50.0	0.00	41.0	0.02	0.026	0.03	0.10	9.16	0.33	50.6	90.7
48	LS2-m-m	50.8	0.00	40.6	0.10	0.022	0.10	0.15	8.49	0.10	49.5	91.4
49	LS2-m-c	51.5	0.00	41.7	0.02	0.000	0.01	0.06	7.38	0.36	49.5	92.6
50	LS2-l-c	51.5	0.00	41.4	0.01	0.000	0.02	0.11	7.31	0.37	49.2	92.6

Table AI. Analyses of kimberlite olivine … (continued)

NN	Sample	MgO	Al2O3	SiO2	CaO	TiO2	Cr2O3	MnO	FeO	NiO	Total	Fo-no
51	LS2-l-m	49.7	0.00	40.9	0.04	0.010	0.08	0.13	9.23	0.32	50.7	90.6
52	LS2-b2-c	51.5	0.01	41.4	0.02	0.000	0.05	0.09	7.50	0.40	49.4	92.4
53	LS3-u-m	50.6	0.00	41.1	0.03	0.010	0.05	0.10	8.49	0.33	100.7	91.4
54	LS3-t4	50.2	0.03	41.1	0.02	0.039	0.04	0.07	8.62	0.34	100.4	91.2
55	Ls3-j3	50.7	0.01	41.0	0.09	0.048	0.08	0.15	8.77	0.11	101.0	91.2
56	LS3-u-m	50.6	0.00	41.1	0.03	0.010	0.05	0.10	8.49	0.33	100.7	91.4
57	LS3-t4	50.2	0.03	41.1	0.02	0.039	0.04	0.07	8.62	0.34	100.4	91.2
58	LS3-t4	50.2	0.03	41.1	0.02	0.039	0.04	0.07	8.62	0.34	100.4	91.2
59	LS3-a-c	51.0	0.01	40.9	0.03	na	0.02	0.10	7.69	0.36	100.0	92.2
60	LS3-a-m	50.2	0.00	40.8	0.07	na	0.02	0.10	8.14	0.38	99.7	91.7
61	LS3-b-c	50.7	0.01	40.8	0.05	na	0.09	0.12	8.24	0.40	100.4	91.6
62	LS3-c2-c	50.1	0.00	40.6	0.06	na	0.00	0.11	8.29	0.38	99.6	91.5
63	LS3-c2-m	50.6	0.00	41.2	0.08	na	0.10	0.13	8.15	0.15	100.3	91.7
64	LS3-d	50.0	0.00	40.3	0.19	na	0.03	0.10	8.06	0.33	99.1	91.7
65	LS3-e-c	49.5	0.00	40.5	0.05	na	0.01	0.11	9.28	0.30	99.8	90.5
66	LS3-e-m	50.1	0.00	40.5	0.06	na	0.00	0.13	8.16	0.15	99.1	91.6
67	LS3-f-c	49.7	0.00	40.5	0.03	na	0.00	0.11	8.55	0.39	99.2	91.2
68	LS3-g-c	49.7	0.00	40.3	0.03	na	0.03	0.11	8.85	0.36	99.3	90.9
69	LS3-g-m	50.2	0.01	40.9	0.13	na	0.00	0.15	7.95	0.22	99.5	91.8
70	LS3-h-c	49.8	0.00	40.4	0.04	na	0.02	0.09	8.46	0.39	99.3	91.3
71	LS3-j1-c	51.2	0.00	40.6	0.01	na	0.02	0.10	7.01	0.34	99.2	92.9
72	LS3-j1-m	50.3	0.00	40.9	0.06	na	0.00	0.14	8.28	0.13	99.8	91.5
73	LS3-j2-c	49.8	0.00	40.7	0.03	na	0.01	0.12	8.70	0.32	99.7	91.1
74	LS3-k-c	50.0	0.01	40.5	0.05	na	0.07	0.10	8.35	0.40	99.5	91.4
75	LS3-u-c	49.9	0.02	40.9	0.04	0.000	0.03	0.12	9.03	0.33	50.5	90.8
76	LS3-s2-c	48.3	0.00	40.3	0.04	0.047	0.01	0.16	11.12	0.37	52.1	88.6
77	LS3-r-c	49.7	0.01	40.8	0.03	0.028	0.06	0.15	9.46	0.34	50.8	90.4
78	LS3-p-m	51.1	0.02	41.0	0.10	0.100	0.00	0.19	8.09	0.17	49.6	91.8
79	LS3-t	50.2	0.00	40.9	0.04	0.028	0.07	0.12	8.50	0.38	50.0	91.2
80	LS3-n	50.2	0.02	41.0	0.09	0.036	0.08	0.15	8.55	0.40	50.3	91.3
81	LS3-l-c	50.0	0.00	41.1	0.03	0.022	0.05	0.14	8.86	0.37	50.6	91.0
82	LS3-e1-c	49.4	0.00	40.8	0.03	0.004	0.05	0.14	9.96	0.35	51.3	89.8
83	LS3-g2-c	49.7	0.00	41.0	0.04	0.009	0.06	0.12	9.31	0.40	51.0	90.5
84	LS4-g-m	48.4	0.00	39.2	0.03	na	0.04	0.08	8.96	0.32	97.1	90.6
85	LS4-d-m	49.0	0.01	40.2	0.39	na	0.09	0.08	8.13	0.35	98.2	91.5
86	LS4-a-c	50.2	0.00	41.0	0.03	na	0.03	0.09	7.97	0.38	99.6	91.8
87	LS4-b-c	50.1	0.02	41.1	0.03	na	0.01	0.11	8.09	0.40	99.8	91.7
88	LS4-c-c	50.3	0.03	41.1	0.04	na	0.03	0.13	7.41	0.34	99.4	92.4
89	LS4-c-m	49.8	0.02	41.2	0.02	na	0.03	0.11	8.42	0.37	99.9	91.3
90	LS4-d-c	49.6	0.01	40.6	0.03	na	0.01	0.11	8.42	0.38	99.2	91.3
91	LS4-e-m	50.0	0.00	40.5	0.03	na	0.00	0.13	8.32	0.13	99.1	91.5
92	LS4-f-c	48.1	0.01	40.4	0.03	na	0.00	0.12	9.99	0.24	98.9	89.6
93	LS4-f-m	47.7	0.01	39.9	0.04	na	0.02	0.10	10.17	0.24	98.1	89.3
94	LS4-h1-c	50.5	0.02	40.8	0.04	na	0.02	0.10	7.53	0.37	99.3	92.3
95	LS4-h2-c	49.3	0.00	40.4	0.04	na	0.06	0.12	8.86	0.35	99.1	90.8
96	LS4-i-c	48.2	0.01	40.1	0.04	na	0.03	0.13	10.47	0.20	99.2	89.1
97	LS4-i-m	50.4	0.00	40.8	0.04	na	0.05	0.13	8.19	0.18	99.8	91.6
98	LS4-j-c	50.8	0.01	41.2	0.02	na	0.00	0.10	6.93	0.36	99.4	92.9
Element profiles in zonned phenocrysts												
99	LS3-k-0	53.2	0.03	42.8	1.10	0.036	0.00	0.41	2.70	0.09	100.4	97.2
100	LS3-k-44.4	53.2	0.15	42.2	0.96	0.032	0.00	0.29	2.80	0.04	99.8	97.1
101	LS3-k-88.8	53.9	0.05	42.7	0.91	0.012	0.00	0.24	2.85	0.10	100.7	97.1
102	LS3-k-133.2	53.5	0.06	42.3	0.96	0.011	0.02	0.24	2.65	0.05	99.8	97.3
103	LS3-k-177.6	52.9	0.09	42.1	1.17	0.007	0.01	0.26	3.33	0.11	100.0	96.6
104	LS3-k-222	50.6	0.09	41.7	0.73	0.005	0.03	0.21	5.79	0.21	99.3	94.0

Table AI. Analyses of kimberlite olivine … (continued)

NN	Sample	MgO	Al2O3	SiO2	CaO	TiO2	Cr2O3	MnO	FeO	NiO	Total	Fo-no
105	LS3-k-266.4	48.6	0.02	41.3	0.11	0.018	0.00	0.12	8.60	0.30	99.1	91.0
106	LS3-k-310.8	48.5	0.02	41.3	0.07	0.021	0.03	0.07	8.94	0.33	99.3	90.6
107	LS3-k-355.2	48.7	0.00	41.1	0.06	0.015	0.03	0.14	8.90	0.31	99.3	90.7
108	LS3-k-399.6	48.9	0.01	41.1	0.12	0.023	0.02	0.11	8.84	0.33	99.4	90.8
109	LS3-s-0	49.5	0.01	41.4	0.06	0.006	0.14	0.13	8.11	0.13	99.5	91.6
110	LS3-s-6.7	49.5	0.01	41.3	0.21	0.059	0.15	0.11	7.82	0.13	99.3	91.9
111	LS3-s-13.3	49.8	0.01	41.4	0.03	0.042	0.11	0.17	8.18	0.15	99.9	91.6
112	LS3-s-20	49.9	0.01	41.3	0.03	0.024	0.14	0.13	7.85	0.19	99.6	91.9
113	LS3-s-26.7	49.3	0.01	41.4	0.03	0.023	0.12	0.13	7.84	0.26	99.1	91.8
114	LS3-s-33.4	49.7	0.01	41.4	0.04	0.008	0.08	0.12	7.92	0.28	99.5	91.8
115	LS3-s-40	50.0	0.01	41.3	0.02	0.025	0.08	0.10	8.18	0.42	100.1	91.6
116	LS3-s-46.7	49.6	0.00	41.3	0.03	0.033	0.03	0.10	7.85	0.43	99.4	91.8
117	LS3-s-53.4	49.5	0.00	41.3	0.05	0.011	0.04	0.10	8.00	0.40	99.4	91.7
118	LS3-s-60	49.6	0.01	41.3	0.04	0.039	0.04	0.06	8.08	0.37	99.5	91.6
119	LS3-s-66.7	49.6	0.00	41.4	0.04	0.043	0.07	0.14	8.21	0.39	99.9	91.5
120	LS3-s-73.4	49.6	0.00	41.2	0.04	0.035	0.06	0.13	8.23	0.37	99.6	91.5
121	LS3-s-80	49.0	0.01	41.2	0.03	0.046	0.05	0.08	8.85	0.32	99.7	90.8
122	LS3-s-86.7	47.8	0.00	41.1	0.03	0.000	0.08	0.21	9.77	0.35	99.4	89.7
123	LS3-s-93.4	46.8	0.08	39.5	0.10	0.034	0.03	0.14	10.52	0.38	97.6	88.8
124	LS3-s-100.1	47.3	0.02	41.3	0.04	0.023	0.01	0.15	10.18	0.36	99.4	89.2
125	LS3-s-106.7	47.7	0.01	40.8	0.04	0.027	0.04	0.18	10.24	0.33	99.4	89.3
126	LS3-s-113.4	47.9	0.00	40.8	0.03	0.012	0.05	0.14	10.26	0.36	99.6	89.3
127	LS3-s-120.1	47.9	0.00	40.8	0.03	0.000	0.01	0.17	10.43	0.32	99.7	89.1
128	LS3-n-0	49.4	0.01	41.7	0.09	0.041	0.02	0.11	8.12	0.20	99.7	91.6
129	LS3-n-10	49.8	0.02	41.6	0.08	0.022	0.08	0.13	7.79	0.16	99.7	91.9
130	LS3-n-20	50.0	0.01	41.3	0.05	0.017	0.07	0.08	8.12	0.16	99.8	91.6
131	LS3-n-30	49.8	0.00	41.5	0.05	0.053	0.13	0.16	7.86	0.14	99.7	91.9
132	LS3-n-40	50.2	0.00	41.3	0.05	0.045	0.05	0.12	7.98	0.18	99.9	91.8
133	LS3-n-50	50.1	0.00	41.5	0.05	0.000	0.01	0.16	7.82	0.14	99.8	91.9
134	LS3-n-60	49.9	0.00	41.5	0.04	0.020	0.14	0.14	7.83	0.20	99.8	91.9
135	LS3-n-70	50.0	0.02	41.5	0.04	0.026	0.14	0.10	7.94	0.21	100.0	91.8
136	LS3-n-80	50.3	0.02	41.5	0.05	0.036	0.04	0.10	7.82	0.42	100.3	92.0
137	LS3-n-90	50.9	0.00	41.8	0.04	0.036	0.04	0.09	6.70	0.33	100.0	93.1
138	LS3-n-100	51.3	0.00	41.6	0.04	0.002	0.06	0.07	6.64	0.35	100.0	93.2
139	LS3-n-110	51.6	0.03	41.5	0.10	0.013	0.04	0.10	6.47	0.34	100.2	93.4
140	LS3-n-120	51.3	0.01	41.6	0.06	0.021	0.04	0.09	6.48	0.33	100.0	93.4
141	LS3-n-130	51.4	0.01	41.6	0.03	0.000	0.04	0.08	6.63	0.30	100.1	93.3
142	LS3-n-140	51.1	0.02	41.5	0.03	0.009	0.06	0.12	6.56	0.31	99.7	93.3
143	LS3-n-150	51.3	0.00	41.7	0.03	0.016	0.00	0.09	6.63	0.33	100.0	93.2
144	LS3-n-160	51.4	0.02	41.6	0.04	0.000	0.05	0.11	6.56	0.34	100.1	93.3
145	LS3-n-170	51.4	0.04	41.5	0.03	0.029	0.09	0.07	6.55	0.33	100.0	93.3
Megacrysts												
146	LS1-meg-m	51.7	0.00	41.2	0.01	0.000	0.03	0.08	7.03	0.37	100.4	92.9
147	LS1-meg-c	51.4	0.02	41.3	0.02	0.000	0.00	0.07	7.03	0.36	100.2	92.9
148	LS1-meg-m	51.6	0.00	41.2	0.02	0.000	0.00	0.08	7.06	0.38	100.4	92.9
149	LS5-meg-c	49.8	0.00	40.6	0.03	0.000	0.01	0.12	9.52	0.31	100.4	90.3
150	LS5-meg-m	49.4	0.00	40.5	0.04	0.000	0.02	0.13	9.41	0.30	99.7	90.3
Aaron Pipe												
151	AN1-l-m*	50.2	0.01	40.9	0.05	0.014	0.09	0.07	8.10	0.38	99.9	91.7
152	AN1-k-m*	50.2	0.00	40.6	0.05	0.004	0.07	0.05	8.45	0.39	99.8	91.4
153	AN1-e-c	51.3	0.01	41.1	0.02	0.030	0.07	0.14	7.66	0.35	100.7	92.3
154	AN1-h-m	50.9	0.00	41.3	0.07	0.008	0.08	0.14	8.28	0.16	101.0	91.6
155	AN1-f-m	49.8	0.00	41.8	0.05	0.030	0.14	0.12	8.49	0.23	100.7	91.3
156	AN1-h-c	49.7	0.00	40.3	0.02	0.003	0.05	0.13	8.11	0.31	48.9	91.6
157	AN1-g-m	51.2	0.00	40.9	0.05	0.021	0.07	0.21	8.47	0.16	49.9	91.5

Table AI. Analyses of kimberlite olivine … (continued)

NN	Sample	MgO	Al2O3	SiO2	CaO	TiO2	Cr2O3	MnO	FeO	NiO	Total	Fo-no
158	AN1-g-c	49.8	0.00	41.0	0.02	0.004	0.09	0.12	8.88	0.34	50.5	90.9
159	AN1-f-c	50.6	0.00	41.7	0.02	0.033	0.03	0.08	8.20	0.40	50.5	91.7
160	AN1-l	51.3	0.02	41.2	0.02	0.016	0.05	0.13	7.40	0.38	49.2	92.5
161	AN1-j-c	51.0	0.02	40.9	0.06	0.000	0.10	0.13	7.98	0.45	49.6	91.9
162	AN1-j6	50.9	0.02	40.9	0.03	0.000	0.04	0.07	8.12	0.41	49.6	91.8
163	AN1-j4	50.3	0.03	40.9	0.06	0.011	0.08	0.04	8.43	0.39	49.9	91.4
164	AN1-j12	50.0	0.02	40.8	0.08	0.053	0.13	0.10	8.33	0.39	49.9	91.4
165	AN1-l-c	51.2	0.01	41.2	0.02	0.000	0.03	0.12	7.46	0.38	49.3	92.4
166	AN1-k-c	50.3	0.03	40.6	0.05	0.000	0.05	0.08	8.89	0.43	50.1	91.0
167	AN1-d-c	49.9	0.00	41.0	0.03	0.018	0.00	0.12	8.89	0.28	50.3	90.9
168	AN1-b-c	51.4	0.01	40.9	0.04	0.000	0.02	0.09	7.48	0.40	48.9	92.4
169	AN1-a1-sm	50.0	0.00	41.3	0.03	0.045	0.05	0.17	9.25	0.36	51.2	90.6
170	AN1-a2-sm	49.8	0.02	41.1	0.03	0.000	0.07	0.13	9.18	0.38	50.9	90.6
171	AN2-c-m	50.3	0.01	40.5	0.07	na	0.00	0.14	8.25	0.15	99.4	91.6
172	AN2-a-c	50.9	0.04	40.7	0.02	na	0.06	0.10	7.68	0.41	100.0	92.2
173	AN2-a-m	50.8	0.00	41.0	0.05	na	0.03	0.12	8.00	0.27	100.3	91.9
174	AN2-b-c	49.6	0.01	40.5	0.02	na	0.00	0.12	9.03	0.30	99.6	90.7
175	AN2-b-m	50.0	0.01	40.4	0.08	na	0.11	0.15	7.97	0.15	98.8	91.8
176	AN2-b-sm	50.5	0.02	40.7	0.05	na	0.03	0.09	8.07	0.41	99.9	91.8
177	AN2-c-c	49.6	0.00	40.5	0.07	na	0.02	0.14	9.13	0.30	99.8	90.6
178	AN2-c-m	50.3	0.01	40.5	0.07	na	0.00	0.14	8.25	0.15	99.4	91.6
179	AN2-c-sm-c	50.3	0.00	40.5	0.04	na	0.00	0.11	8.21	0.38	99.6	91.6
180	AN2-c-sm-m	50.4	0.00	40.5	0.07	na	0.01	0.12	8.09	0.15	99.3	91.7
181	AN2-d-c	50.1	0.00	40.7	0.04	na	0.01	0.10	8.81	0.39	100.1	91.0
182	AN2-d-m	50.4	0.01	40.6	0.07	na	0.10	0.14	8.03	0.15	99.5	91.8
183	AN2-e1-c	50.9	0.02	40.7	0.03	na	0.00	0.09	7.45	0.37	99.6	92.4
184	AN2-e1-m	50.7	0.01	40.4	0.08	na	0.06	0.14	8.18	0.15	99.7	91.7
185	AN2-e1-m	49.9	0.01	40.2	0.12	na	0.04	0.13	8.28	0.12	98.8	91.5
186	AN2-e2-c	50.3	0.00	40.8	0.05	na	0.05	0.11	8.17	0.38	99.8	91.6
187	AN2-e2-m	50.1	0.01	40.5	0.07	na	0.05	0.15	8.16	0.15	99.2	91.6
188	AN2-e3-sm	50.2	0.00	40.6	0.06	na	0.04	0.14	8.37	0.32	99.7	91.4
189	AN2-f	50.1	0.00	41.0	0.09	na	0.14	0.12	8.11	0.33	99.9	91.7
190	AN2-f	50.4	0.00	40.5	0.07	na	0.09	0.14	8.24	0.14	99.7	91.6
191	AN2-g-c	49.5	0.00	40.4	0.03	na	0.00	0.11	9.05	0.35	99.5	90.7
192	AN2-g-m	50.0	0.02	40.5	0.02	na	0.11	0.13	8.07	0.20	99.1	91.7
193	AN2-h-c	50.2	0.00	40.7	0.02	na	0.00	0.11	8.49	0.33	99.8	91.3
194	AN2-h-m	50.5	0.01	40.6	0.05	na	0.08	0.12	7.99	0.22	99.6	91.8
195	AN2-i-c	50.0	0.01	40.6	0.04	na	0.00	0.09	8.64	0.38	99.7	91.1
196	AN2-i-m	49.7	0.00	40.7	0.11	na	0.06	0.17	8.42	0.15	99.4	91.3
197	AN2-j-c	49.7	0.01	40.3	0.04	na	0.07	0.10	8.76	0.37	99.4	91.0
198	AN2-j-m	50.8	0.00	41.3	0.06	na	0.09	0.15	8.22	0.14	100.8	91.7
199	AN2-k-c	51.0	0.02	41.0	0.02	na	0.04	0.09	7.21	0.37	99.8	92.7
200	AN2-k-m	50.7	0.00	40.5	0.07	na	0.11	0.14	8.05	0.16	99.7	91.8
201	AN2-k-sm-c	50.6	0.01	40.5	0.06	na	0.02	0.11	7.68	0.32	99.3	92.2
202	AN2-l-c	50.0	0.03	40.4	0.07	na	0.07	0.10	8.37	0.36	99.4	91.4
203	AN2-l-m	50.1	0.00	40.1	0.08	na	0.07	0.13	8.11	0.16	98.8	91.7
204	AN2-m-c	50.2	0.02	40.3	0.04	na	0.02	0.10	7.92	0.42	99.1	91.9
205	AN2-m-m	50.6	0.02	40.4	0.06	na	0.07	0.10	8.00	0.24	99.5	91.8
206	AN3-a-c	49.6	0.01	40.9	0.04	0.000	0.07	0.09	9.28	0.39	50.8	90.5
207	AN3-a-m	50.0	0.03	40.8	0.04	0.014	0.04	0.08	9.45	0.33	50.7	90.4
208	AN3-a-m1	49.2	0.00	41.3	0.04	0.026	0.01	0.14	9.35	0.40	51.3	90.4
209	AN3-b-c	51.8	0.01	41.7	0.01	0.010	0.00	0.07	6.93	0.41	49.2	93.0
210	AN3-b-m	51.2	0.03	42.1	0.02	0.005	0.00	0.11	6.87	0.36	49.4	93.0
211	AN3-c-m	50.8	0.01	41.1	0.03	0.000	0.03	0.10	8.07	0.38	49.7	91.8
212	AN3-c-c	50.9	0.03	41.1	0.02	0.003	0.01	0.08	7.89	0.41	49.5	92.0

Table AI. Analyses of kimberlite olivine … (continued)

NN	Sample	MgO	Al2O3	SiO2	CaO	TiO2	Cr2O3	MnO	FeO	NiO	Total	Fo-no
213	AN3-d-c	50.9	0.00	41.2	0.03	0.006	0.03	0.12	8.43	0.44	50.2	91.5
214	AN3-d-m	49.9	0.02	41.6	0.06	0.014	0.10	0.05	8.41	0.47	50.7	91.4
215	AN3-e-c	49.9	0.01	40.9	0.03	0.032	0.04	0.14	8.88	0.37	50.4	90.9
216	AN3-e-m	49.2	0.00	41.7	0.03	0.072	0.01	0.14	8.90	0.29	51.1	90.8
217	AN3-h-c	49.7	0.02	41.2	0.02	0.000	0.06	0.14	9.15	0.37	50.9	90.6
218	AN3-h-m	50.6	0.02	40.2	0.04	0.019	0.05	0.11	8.92	0.34	49.7	91.0
219	AN3-g1	49.4	0.05	41.2	0.06	0.000	0.07	0.09	8.76	0.43	50.6	90.9
220	AN3-f1	50.3	0.02	41.3	0.05	0.009	0.07	0.08	8.30	0.40	50.2	91.5
221	AN3-f2	50.9	0.01	41.4	0.02	0.007	0.03	0.12	7.44	0.37	49.4	92.4
222	AN3-f2-m	51.0	0.03	41.7	0.02	0.006	0.05	0.11	7.42	0.34	49.6	92.5
223	AN4-d2-m	50.2	0.00	41.0	0.08	na	0.04	0.10	7.76	0.41	99.6	92.0
224	AN4-b2	50.3	0.00	40.6	0.07	na	0.07	0.09	7.68	0.38	99.2	92.1
225	AN4-a-c	49.7	0.02	40.3	0.04	na	0.00	0.11	8.21	0.38	98.7	91.5
226	AN4-b1-c	49.6	0.01	40.4	0.04	na	0.04	0.10	8.52	0.42	99.1	91.2
227	AN4-b1-m	50.6	0.00	40.6	0.04	na	0.04	0.10	8.05	0.24	99.7	91.8
228	AN4-c-c	50.2	0.00	40.3	0.01	na	0.01	0.12	8.58	0.33	99.5	91.2
229	AN4-d1-c	50.3	0.00	40.4	0.05	na	0.00	0.13	7.98	0.38	99.3	91.8
230	AN4-e-c	49.7	0.00	40.6	0.01	na	0.01	0.13	8.71	0.34	99.5	91.1
231	AN4-f1-c	50.2	0.01	40.8	0.03	na	0.01	0.09	8.29	0.31	99.8	91.5
232	AN4-f2-c	50.6	0.03	40.7	0.03	na	0.06	0.11	7.76	0.38	99.7	92.1
233	AN4-g1-c	51.0	0.01	40.7	0.02	na	0.05	0.10	7.50	0.38	99.7	92.4
234	AN4-g2-c	50.0	0.01	40.6	0.03	na	0.00	0.11	8.63	0.33	99.7	91.2
235	AN4-h-c	51.4	0.00	40.9	0.02	na	0.01	0.10	6.95	0.35	99.6	92.9
236	AN4-h-m	50.6	0.00	40.3	0.03	na	0.03	0.11	7.98	0.20	99.2	91.9
237	AN4-i-c	47.8	0.01	40.1	0.02	na	0.00	0.15	11.35	0.37	99.8	88.2
238	AN4-i-m	50.8	0.00	41.2	0.03	na	0.04	0.11	7.95	0.30	100.5	91.9
239	AN5-b-1*	50.5	0.00	41.2	0.05	0.000	0.06	0.13	8.07	0.33	100.3	91.8
240	AN5-c-2*	50.1	0.01	41.6	0.06	0.020	0.09	0.12	7.92	0.22	100.1	91.9
241	AN5-i1	50.6	0.00	41.3	0.06	0.024	0.04	0.14	8.34	0.37	100.9	91.5
242	AN5-c	51.1	0.03	40.8	0.17	0.000	0.11	0.20	8.26	0.16	100.8	91.7
243	AN5-d2-m	50.8	0.03	40.7	0.12	0.029	0.12	0.20	8.66	0.16	100.8	91.3
244	AN5-d4-c	50.3	0.03	41.2	0.05	0.044	0.01	0.09	8.72	0.40	50.5	91.1
245	AN5-d3-c	52.8	0.01	41.8	0.02	0.000	0.00	0.01	5.84	0.34	48.0	94.2
246	AN5-d1-c	50.7	0.05	41.1	0.14	0.057	0.08	0.16	8.56	0.32	50.4	91.4
247	AN5-e-c	49.6	0.02	40.9	0.04	0.036	0.04	0.13	9.51	0.32	51.0	90.3
248	AN5-e-m	50.1	0.02	41.3	0.06	0.011	0.08	0.12	8.07	0.24	49.9	91.7
249	AN5-f-c	51.2	0.02	41.4	0.02	0.000	0.01	0.09	6.97	0.38	48.9	92.9
250	AN5-g-c	50.4	0.02	41.1	0.14	0.000	0.08	0.14	8.25	0.19	49.8	91.6
251	AN5-g-m	51.0	0.01	40.9	0.15	0.026	0.09	0.19	8.37	0.17	49.9	91.6
252	An5-l2-sm	50.2	0.02	41.1	0.05	0.000	0.05	0.13	8.78	0.40	50.5	91.1
253	AN5-l3-sm	50.3	0.02	41.1	0.07	0.020	0.04	0.09	8.32	0.34	50.0	91.5
254	AN5-h1	50.6	0.02	41.1	0.05	0.004	0.01	0.06	7.87	0.44	49.6	92.0
255	AN5-h2	51.0	0.04	41.2	0.05	0.003	0.07	0.06	7.99	0.40	49.8	91.9
256	AN5-b	50.0	0.01	41.3	0.05	0.034	0.03	0.09	8.55	0.38	50.4	91.2
Element profiles in zonned phenocrysts												
257	AN1-l-0	49.9	0.00	41.6	0.09	0.016	0.01	0.13	8.09	0.14	100.0	91.7
258	AN1-l-10	50.0	0.01	41.1	0.07	0.012	0.04	0.15	7.98	0.15	99.5	91.8
259	AN1-l-20	49.9	0.01	41.3	0.07	0.014	0.04	0.16	8.16	0.16	99.8	91.6
260	AN1-l-30	49.8	0.01	41.3	0.06	0.000	0.01	0.11	7.95	0.12	99.4	91.8
261	AN1-l-40	49.6	0.01	41.2	0.05	0.001	0.05	0.15	7.59	0.15	98.9	92.1
262	AN1-l-50	50.1	0.01	41.3	0.06	0.050	0.02	0.13	7.87	0.25	99.8	91.9
263	AN1-l-60	50.1	0.02	41.0	0.06	0.015	0.02	0.13	7.90	0.37	99.6	91.9
264	AN1-l-70	50.0	0.01	41.3	0.03	0.039	0.04	0.13	7.54	0.45	99.5	92.2
265	AN1-l-80	50.1	0.00	41.2	0.04	0.041	0.02	0.09	7.86	0.37	99.8	91.9
266	AN1-l-90	48.9	0.02	41.0	0.04	0.000	0.04	0.12	8.62	0.25	99.0	91.0

Table AI. Analyses of kimberlite olivine … (continued)

NN	Sample	MgO	Al2O3	SiO2	CaO	TiO2	Cr2O3	MnO	FeO	NiO	Total	Fo-no
267	AN1-l-100	49.8	0.01	40.9	0.04	0.035	0.02	0.14	8.01	0.34	99.3	91.7
268	AN1-l-110	50.8	0.02	41.1	0.02	0.025	0.06	0.11	7.08	0.37	99.6	92.7
269	AN1-l-120	50.5	0.01	41.5	0.02	0.047	0.02	0.08	7.01	0.39	99.5	92.8
270	AN1-l-130	50.5	0.02	41.1	0.02	0.000	0.04	0.12	6.90	0.37	99.0	92.9
271	AN1-c-0	50.7	0.03	41.0	0.12	0.017	0.04	0.19	7.95	0.13	100.2	91.9
272	AN1-c-8.5	50.3	0.00	41.2	0.08	0.030	0.04	0.16	8.02	0.19	100.0	91.8
273	AN1-c-17	50.4	0.00	41.2	0.07	0.003	0.07	0.17	7.84	0.20	99.9	92.0
274	AN1-c-25.5	50.6	0.03	41.3	0.04	0.000	0.08	0.13	7.70	0.22	100.0	92.1
275	AN1-c-34*	50.5	0.02	41.3	0.04	0.020	0.05	0.08	7.80	0.37	100.2	92.0
276	AN1-c-42.5	50.0	0.03	41.2	0.03	0.000	0.06	0.06	8.07	0.31	99.8	91.7
277	AN1-c-51*	50.2	0.02	41.1	0.20	0.000	0.06	0.12	7.99	0.37	100.0	91.8
278	AN1-c-59.5	50.1	0.00	41.4	0.04	0.018	0.05	0.10	7.98	0.35	100.0	91.8
279	AN1-c-68	50.6	0.00	41.1	0.05	0.010	0.02	0.15	7.99	0.33	100.2	91.9
280	AN1-c-76.5	50.7	0.00	41.4	0.06	0.013	0.05	0.13	7.38	0.32	100.1	92.5
281	AN1-c-85	50.6	0.01	41.6	0.05	0.000	0.06	0.07	7.12	0.41	100.0	92.7
282	AN1-c-93.5	51.4	0.03	41.5	0.06	0.000	0.04	0.11	6.72	0.39	100.2	93.2
283	AN1-c-102	51.4	0.00	41.7	0.01	0.000	0.00	0.09	6.78	0.42	100.4	93.1
284	AN1-c-110.5	51.3	0.02	41.8	0.03	0.000	0.04	0.08	6.81	0.38	100.5	93.1
	Grizzly Pipe											
285	G19-k-m	51.0	0.00	40.9	0.08	0.025	0.01	0.15	8.33	0.13	100.6	91.6
286	Gr19-g1-m	51.5	0.01	40.9	0.07	0.035	0.13	0.12	8.16	0.29	101.2	91.8
287	Gr19-b1	50.5	0.01	41.2	0.04	0.028	0.11	0.08	8.39	0.42	100.7	91.5
288	GR19-j1-m	50.5	0.02	41.2	0.05	0.036	0.04	0.15	8.73	0.22	50.4	91.2
289	GR19-j1-c	51.3	0.02	41.4	0.01	0.000	0.04	0.13	7.74	0.39	49.8	92.2
290	GR19-j3-c	49.8	0.02	40.8	0.07	0.022	0.04	0.12	9.28	0.38	50.7	90.5
291	GR19-k-c	51.1	0.01	41.3	0.02	0.017	0.03	0.13	7.48	0.40	49.3	92.4
292	GR19-f-m	50.8	0.03	41.2	0.05	0.006	0.07	0.11	7.98	0.30	49.7	91.9
293	GR19-f-c	51.2	0.00	41.4	0.03	0.025	0.02	0.10	7.32	0.38	49.3	92.6
294	GR19-g1-m	50.6	0.02	41.0	0.05	0.022	0.03	0.13	8.16	0.40	49.8	91.7
295	GR19-g1-c	50.2	0.03	41.0	0.06	0.005	0.04	0.10	8.91	0.41	50.6	90.9
296	GR19-10	50.5	0.00	41.4	0.03	0.000	0.07	0.08	8.41	0.36	50.3	91.5
297	GR19-a-c	49.8	0.01	41.0	0.03	0.007	0.02	0.11	9.56	0.33	51.1	90.3
298	GR19-e-c	49.6	0.00	41.1	0.02	0.001	0.00	0.19	9.47	0.36	51.1	90.3
299	GR19-d-c	49.8	0.00	40.9	0.03	0.000	0.00	0.07	8.96	0.35	50.3	90.8
300	GR19-c-c	50.6	0.00	41.3	0.03	0.001	0.01	0.09	8.32	0.37	50.1	91.6
301	GR19-b1-c	50.4	0.01	41.2	0.03	0.018	0.03	0.11	8.47	0.37	50.2	91.4
302	Gr43-k2*	51.0	0.02	41.1	0.03	0.000	0.06	0.09	8.17	0.42	100.9	91.8
303	Gr43-e-c*	50.5	0.01	41.1	0.06	0.017	0.17	0.11	8.57	0.23	100.8	91.3
304	Gr43-a1-m*	50.1	0.02	41.0	0.18	0.053	0.06	0.22	8.77	0.10	100.4	91.1
305	Gr43-f-m	50.2	0.02	41.5	0.06	0.018	0.14	0.11	8.38	0.40	100.8	91.4
306	Gr43-c-m	50.1	0.00	41.0	0.08	0.013	0.08	0.16	8.48	0.15	100.0	91.3
307	Gr43-e-m	50.6	0.01	41.2	0.06	0.026	0.04	0.12	8.55	0.17	100.8	91.3
308	Gr43-b-m	50.5	0.00	41.1	0.07	0.027	0.05	0.13	8.39	0.16	100.4	91.5
309	Gr43-b-m	50.6	0.01	41.4	0.04	0.001	0.11	0.10	8.24	0.41	101.0	91.6
310	GR43-l-m	50.2	0.00	41.3	0.03	0.000	0.11	0.16	8.28	0.37	50.3	91.5
311	GR43-l-m	50.7	0.00	41.1	0.04	0.006	0.01	0.14	8.50	0.37	50.1	91.5
312	GR43-l-c	50.3	0.02	41.1	0.05	0.000	0.06	0.12	8.65	0.32	50.2	91.2
313	GR43-d-c	50.9	0.00	41.3	0.03	0.032	0.08	0.08	7.81	0.34	49.7	92.1
314	GR43-c-c	51.4	0.00	41.2	0.02	0.009	0.03	0.02	6.98	0.40	48.7	92.9
315	GR43-k1-c	50.1	0.02	41.3	0.05	0.026	0.03	0.17	8.88	0.44	50.9	91.0
316	GR43-h-m	49.5	0.01	41.5	0.03	0.040	0.07	0.04	8.02	0.34	50.0	91.7
317	GR43-h-c	51.9	0.00	41.3	0.01	0.026	0.03	0.09	7.03	0.34	48.8	92.9
318	GR43-h-c	51.5	0.00	41.3	0.02	0.001	0.02	0.09	7.44	0.37	49.2	92.5
319	GR43-e-c	49.9	0.01	40.9	0.01	0.021	0.01	0.17	9.19	0.33	50.6	90.6
320	GR43-g-c	50.8	0.01	41.5	0.04	0.000	0.05	0.08	7.97	0.40	50.0	91.9

Table AI. Analyses of kimberlite olivine … (continued)

NN	Sample	MgO	Al2O3	SiO2	CaO	TiO2	Cr2O3	MnO	FeO	NiO	Total	Fo-no
321	GR43-a1-c	50.4	0.00	41.3	0.04	0.007	0.13	0.11	8.42	0.40	50.4	91.4
Torrie Pipe												
322	TQ3-c	49.8	0.02	40.7	0.03	na	0.09	0.11	9.21	0.26	100.2	90.6
323	TQ3-f	50.0	0.01	41.1	0.04	0.045	0.03	0.12	8.98	0.19	100.5	90.9
324	TQ3-a	49.7	0.02	41.1	0.06	0.026	0.02	0.16	9.01	0.18	100.3	90.8
325	TQ13-h-1*	49.4	0.00	41.3	0.05	0.038	0.09	0.09	8.90	0.23	100.1	90.8
326	TQ13-l-1**	49.2	0.00	41.0	0.04	0.023	0.10	0.09	8.90	0.21	99.6	90.8
327	TQ13B-f	49.5	0.00	40.9	0.05	0.063	0.04	0.10	9.07	0.16	99.9	90.7
328	TQ13b-d2	49.7	0.00	40.7	0.06	na	0.04	0.10	9.10	0.19	99.9	90.7
329	TQ15-n*/**	49.7	0.01	40.5	0.03	na	0.05	0.10	9.21	0.23	99.8	90.6
330	TQ15-x	50.0	0.01	40.8	0.05	na	0.07	0.12	9.05	0.31	100.4	90.8
331	TQ15-f	49.7	0.04	41.1	0.05	0.041	0.13	0.10	8.81	0.26	100.2	91.0
332	TQ15-qr	49.8	0.00	40.9	0.04	0.033	0.01	0.13	8.93	0.15	100.0	90.9
333	TQ15-n	49.9	0.03	40.7	0.07	0.073	0.03	0.18	8.65	0.21	99.8	91.1
334	TQ17-f-1*	49.3	0.00	40.8	0.10	0.049	0.07	0.12	8.73	0.34	99.5	91.0
335	TQ18-c-c	50.1	0.02	40.7	0.06	na	0.05	0.09	8.83	0.37	100.2	91.0
336	TQ-18E-2*	49.7	0.01	40.5	0.07	0.044	0.09	0.12	8.62	0.15	99.334	91.1

* – analyses used in Ol-Sp thermobarometry calculations

** – analyses used in Ol-Ilm thermometry calculations